Die approbierte gedruckte Originalversion dieser Diplomarbeit ist an der TU Wien Bibliothek verfügbar.
The approved original version of this thesis is available in print at TU Wien Bibliothek.

TECHNISCHE UNIVERSITÄT WIEN
Vienna University of Technology

GRADUATE SCHOOL OF FRONTIER SCIENCES
THE UNIVERSITY OF TOKYO

DIPLOMA THESIS

Microstructure and thermoelectric properties of full-Heusler compounds based on Fe2VAl co-doped with Ta and Si

under the supervision of

Univ.Prof. Dr. Kaoru Kimura[1], Ass.Prof. Dr. Yukari Katsura[1],
Dr. Kazuki Tobita[1], Dipl.-Ing. Alexander Riss[2], Dipl.-Ing. Michael Parzer[2],
Dipl.-Ing. Bernhard Hinterleitner[2],
Ao.Univ.Prof. Univ.Prof. Dipl.-Ing. Dr.techn. Ernst Bauer[2]

[1] Department of Advanced Materials Science, GSFS, The University of Tokyo

[2] Institut für Festkörperphysik, Technische Universität Wien

by

Fabian Garmroudi[1,2]
01427515
f.garmroudi@gmx.at
1040 Vienna, Austria, EU

TU Bibliothek Your knowledge hub WIEN

Die approbierte gedruckte Originalversion dieser Diplomarbeit ist an der TU Wien Bibliothek verfügbar.
The approved original version of this thesis is available in print at TU Wien Bibliothek.

Abstract

In the course of this work we investigated the effect of Ta-doping at the V-site and Si-doping at the Al-site in Fe_2VAl-based Heusler compounds with respect to the microstructure and thermoelectric properties. As band structure calculations suggest the Ta-doping could lead to an improvement of the electronic structure while Si is an excellent doping element for tuning the carrier concentration within the rigid band model. Samples with the composition $Fe_2V_{1-x}Ta_xAl_{1-y}Si_y$ were synthesized by induction melting and a multitude of different annealing conditions, varying temperature and annealing time were applied in order to optimize the microstructure and solubility of Ta and Si. While XRD results showed a single phase for all compositions except the sample with $x = 0.1$ and $y = 0.1$, the SEM images revealed tiny amounts of impurity precipitates in the microstructure of $Fe_2V_{0.95}Ta_{0.05}Al_{0.9}Si_{0.1}$ and $Fe_2V_{0.9}Ta_{0.1}Al$. The impurity peaks could be attributed to a hexagonal Laves phase that crystallizes in the C14 structure. The amount of secondary phase increased with annealing time and has been shown to have a detrimental effect on S due to its metallic character. We measured ρ and S in a broad temperature range from $4\,\mathrm{K} \rightarrow 800\,\mathrm{K}$ and $300\,\mathrm{K} \rightarrow 800\,\mathrm{K}$ respectively. The maximum power factor was $PF \approx 7 - 8\,\mathrm{mW/mK^2}$, which is an improvement of almost 50 % compared to $Fe_2VAl_{1-y}Si_y$-based compounds that have been reported in literature.

Die approbierte gedruckte Originalversion dieser Diplomarbeit ist an der TU Wien Bibliothek verfügbar.
The approved original version of this thesis is available in print at TU Wien Bibliothek.
TU Bibliothek Your knowledge hub WIEN

Die approbierte gedruckte Originalversion dieser Diplomarbeit ist an der TU Wien Bibliothek verfügbar.
The approved original version of this thesis is available in print at TU Wien Bibliothek.

Zusammenfassung

Im Zuge dieser Diplomarbeit wurden Heusler-Verbindungen der Zusammensetzung $Fe_2V_{1-x}Ta_xAl_{1-y}Si_y$ bezüglich ihrer Mikrostruktur und thermoelektrischen Eigenschaften hin untersucht. Berechnungen der Bandstruktur deuten auf eine Verbesserung der elektronischen Struktur für Ta-dotierte Zusammensetzungen hin, während die Substitution von Si an der Stelle von Al eine Möglichkeit bietet die Ladungsträgerdichte zu optimieren, ohne dabei die elektronische Zustandsdichte nahe der Fermi-Energie wesentlich zu verändern. Mittels Induktionsschmelzsynthese wurden die Proben hergestellt und einer Reihe unterschiedlicher Wärmebehandlungen ausgesetzt, wobei die Temperatur und Dauer der Wärmebehandlung variiert wurden. Obwohl die Ergebnisse der Röntgendiffraktometrie nur bei der Probe mit der Zusammensetzung $Fe_2V_{0.9}Ta_{0.1}Al_{0.9}Si_{0.1}$ auf eine Fremdphase hindeuten ließen, konnten in der Mikrostruktur von $Fe_2V_{0.95}Ta_{0.05}Al_{0.9}Si_{0.1}$ und $Fe_2V_{0.9}Ta_{0.1}Al$ kleine Abscheidungen einer Ta- und Si-reichen Sekundärphase, welche als hexagonale Laves-Phase mit dem Strukturtyp C14 identifiziert wurde, festgestellt werden. Aufgrund der metallischen Eigenschaften der Fremdphase stellte sich bei größerer Präzipitation in der Mikrostruktur eine Verschlechterung des Seebeck-Koeffizienten heraus. Nichtsdestotrotz ergab sich, aufgrund der optimierten Mikrostruktur und positiven Auswirkung der Ta-Dotierung auf die elektronische Struktur, ein maximal gemessener Powerfaktor von $PF \approx 7 - 8\,\mathrm{mW/mK^2}$, was gegenüber $Fe_2VAl_{1-y}Si_y$-basierenden Heusler-Verbindungen aus der Literatur eine Verbesserung um fast 50 % darstellt.

Die approbierte gedruckte Originalversion dieser Diplomarbeit ist an der TU Wien Bibliothek verfügbar.
The approved original version of this thesis is available in print at TU Wien Bibliothek.
TU Bibliothek WIEN Your knowledge hub

Contents

1 Introduction **1**
1.1 Historical background and overview 2
1.2 Thermoelectric parameters 4

2 Theory **5**
2.1 Schrödinger equation 5
2.2 Bloch's theorem 6
2.3 Boltzmann theory 7
2.3.1 Group velocity 7
2.3.2 Effective mass 8
2.3.3 Boltzmann transport equation 8
2.3.4 Electrical conductivity 11
2.3.5 Seebeck coefficient 12
2.4 Landauer theory 12
2.4.1 Charge transport 13
2.4.2 Heat transport 16
2.5 The ideal transport function 19
2.6 The ideal position of the Fermi energy 20
2.7 Band convergence and valley degeneracy 24
2.8 Density functional theory and band structure calculation 26
2.8.1 Hohenberg-Kohn theorems 26
2.8.2 Kohn-Sham equations 27
2.9 Photoemission spectroscopy as a way to study the electronic structure 29

3 Characteristics of full-Heusler materials based on Fe2VAl **33**
3.1 Crystal structure 33
3.2 Anti-site disorder 36
3.3 Ternary phase diagrams for the (Fe,V,Al)- system 39
3.4 Electronic structure 41
3.4.1 Rigid band model 43
3.5 Choice of doping elements 44
3.5.1 Silicon doping effect 44
3.5.2 Tantalum doping effect 45

Die approbierte gedruckte Originalversion dieser Diplomarbeit ist an der TU Wien Bibliothek verfügbar.
The approved original version of this thesis is available in print at TU Wien Bibliothek.
TU WIEN Bibliothek Your knowledge hub

4 Experimental Methods **49**
4.1 Synthesis 49
4.1.1 Induction melting 50
4.2 Annealing conditions 51
4.3 XRD measurement set-up 52
4.4 Observation of microstructure by SEM 52
4.5 Measurement of Seebeck coefficient and electrical resistivity 53

5 Results **55**
5.1 XRD patterns 55
5.1.1 Lattice parameter 58
5.2 Microstructure 59
5.2.1 Single phase region and solubility limit 59
5.2.2 Microstructural evolution with annealing 62
5.3 Electrical resistivity 65
5.3.1 Effect of Ta- and Si-substitution 65
5.3.2 Effect of impurity phase and annealing 68
5.4 Seebeck coefficient 70
5.4.1 Effect of Ta- and Si-substitution 70
5.4.2 Effect of impurity phase and annealing 73
5.5 Power factor 74

6 Conclusion **77**

Acknowledgements **79**

List of Figures **80**

Bibliography **83**

Die approbierte gedruckte Originalversion dieser Diplomarbeit ist an der TU Wien Bibliothek verfügbar.
The approved original version of this thesis is available in print at TU Wien Bibliothek.
TU Bibliothek WIEN Your knowledge hub

Die approbierte gedruckte Originalversion dieser Diplomarbeit ist an der TU Wien Bibliothek verfügbar.
The approved original version of this thesis is available in print at TU Wien Bibliothek.

1 Introduction

The changing climate and the global energy crisis have been getting more and more into focus over the past decade. Therefore, there has been an increasing demand for renewable and innovative energy conversion technologies which have become more important than ever. One of the potential candidates in this regard are thermoelectric materials, which can directly convert heat into electricity. Any kind of thermal sources can be used for such conversion in a thermoelectric device, which primarily makes them attractive for reusing waste heat. Because of that widespread area of application, reaching from car engines to spacecraft to Peltier-cooled refrigerators or even to thermoelectric wristwatches, this class of materials has been very attractive for research. On the contrary, due to their high cost as well as their poor efficiency, only few of them have been commercialised so far.

Full-Heusler materials are only one among a large number of material classes, which are being investigated as thermoelectric materials. The most prominent candidate within the full-Heusler family so far has been Fe_2VAl. Although the thermoelectric figure of merit ZT is relatively low in Fe_2VAl-based compounds, they are promising candidates due to their excellent mechanical and chemical long-term stability as well as their moderately low costs. Moreover, these compounds feature a very interesting, semimetallic electronic structure with a pseudo bandgap that has steep slopes in the electronic density of states at both sides of the Fermi energy E_F. This allows for large values of n-type and p-type Seebeck coefficient, when E_F slightly shifts due to doping or off-stoichiometric composition change.
Recently, the effect of heavy elemental substitution as well as thin film deposition and microstructural tailoring in order to reduce the lattice thermal conductivity have been the main focus of study [18, 24, 27, 34]. Not so much effort has been put in improving the power factor PF of Fe_2VAl-based full Heusler systems lately as PF is already very high. Nonetheless, this work will primarily focus on the Seebeck coefficient and electrical resistivity of $Fe_2V_{1-x}Ta_xAl_{1-y}Si_y$ and how they depend on the microstructure. Prior to that, a short introduction into the thermoelectrics research field will be presented, followed by the most important theoretical solid state physics concepts and fundamental characteristics of Fe_2VAl.

Die approbierte gedruckte Originalversion dieser Diplomarbeit ist an der TU Wien Bibliothek verfügbar.
The approved original version of this thesis is available in print at TU Wien Bibliothek.
TU WIEN Bibliothek Your knowledge hub

1.1 Historical background and overview

The basic principle of thermoelectric energy conversion in solid-state bodies is the Seebeck effect, which was first discovered by the German physicist Thomas Johann Seebeck in 1821 [12]. He noticed a relation between heat and magnetism when holding a compass needle close to an electric circuit made of two different metals with one junction being at a higher temperature than the other.
Shortly after that, in 1834, the Peltier effect, which is the inverse Seebeck effect, was discovered. As shown in Figure 1.1 the Peltier effect is the cooling of one junction in opposite to the other as a result of an electric current that is flowing through a thermocouple.

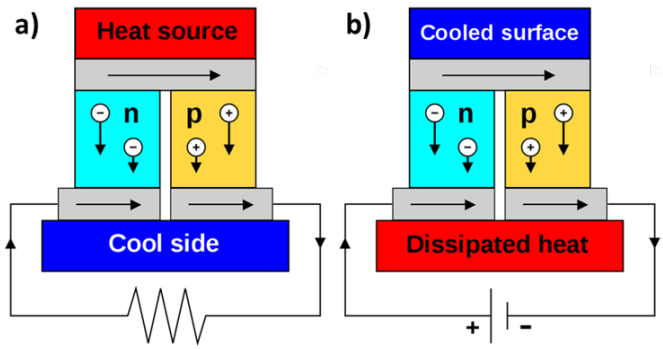

Figure 1.1: a) Seebeck effect: Temperature gradient causes charge carriers to move from the hot to the cold end. b) Peltier effect: External voltage gradient causes charge carriers to transport heat and cool one side in respect to the other. Image from [67].

However, it was only in the beginning of the 20th century that Edmund Altenkirch introduced the so-called "thermoelectric figure of merit" ZT for the first time, which can be expressed as a function of Seebeck coefficient S, electrical conductivity σ and thermal conductivity λ via the relation:

$$ZT = \frac{S^2\sigma}{\lambda}T. \tag{1.1}$$

This value is directly related to the power conversion efficiency of a thermoelectric device by:

$$\eta = \frac{T_H - T_C}{T_H}\frac{\sqrt{1+ZT}-1}{\sqrt{1+ZT}+\frac{T_C}{T_H}}, \tag{1.2}$$

where T_H is the hot-side temperature, T_C the cold-side temperature and $T = (T_H + T_C)/2$ is the mean temperature. Figure 1.2 shows the thermoelectric power conversion efficiency for various average ZT values [12].

Die approbierte gedruckte Originalversion dieser Diplomarbeit ist an der TU Wien Bibliothek verfügbar.
The approved original version of this thesis is available in print at TU Wien Bibliothek.
TU Bibliothek Your knowledge hub WIEN

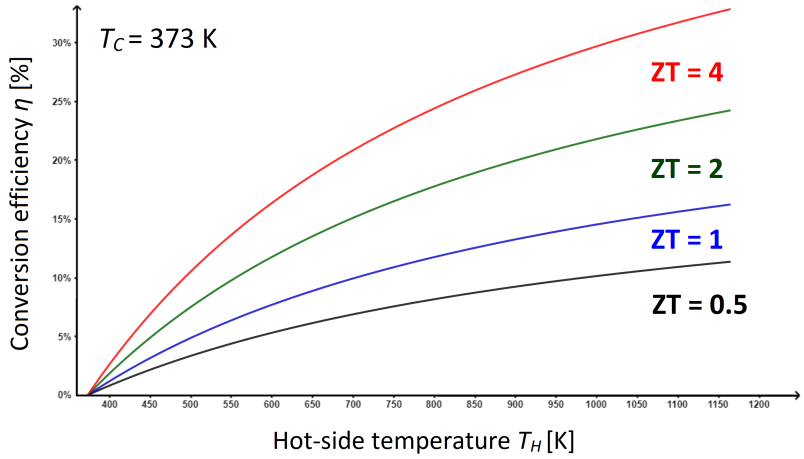

Figure 1.2: Thermoelectric power conversion efficiency as a function of hot-side temperature for different average values of ZT.

Since the 1950s these thermoelectric properties have been tried to be understood and improved in terms of solid state physics models. The well-known thermoelectric material Bi_2Te_3 has already been proposed in 1954 [16] and has been succesfully commercialised due to a high $ZT > 1$. While Bi_2Te_3 ranks amongst the best-performing thermoelectrics at room temperature, PbTe and Half-Heusler alloys together with others dominate the high temperature region of ZT. Figure 1.3 shows the temperature dependence of ZT for various material classes [12].

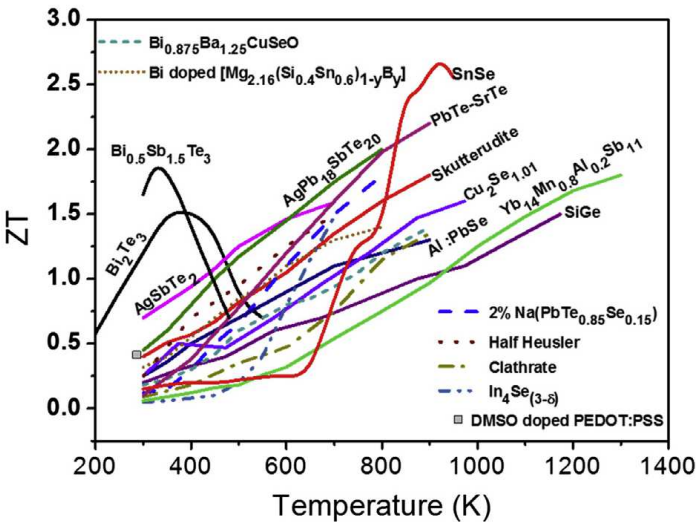

Figure 1.3: Temperature dependence of thermoelectric figure of merit ZT for different material classes. Reproduced with permission from [12].

Die approbierte gedruckte Originalversion dieser Diplomarbeit ist an der TU Wien Bibliothek verfügbar.
The approved original version of this thesis is available in print at TU Wien Bibliothek.
TU Bibliothek Your knowledge hub WIEN

1.2 Thermoelectric parameters

As already mentioned, the so-called figure of merit ZT is a good way to evaluate the performance of a thermoelectric material:

$$ZT = \frac{S^2\sigma}{\lambda_e + \lambda_{\text{lattice}}}T, \tag{1.3}$$

where the parameters are the Seebeck coefficient S, the electrical conductivity σ and the electronic thermal conductivity λ_e and λ_{lattice} being the lattice thermal conductivity. The numerator is also called power factor PF and strongly depends on the carrier concentration n, the electronic scattering time τ and the electronic band structure $E(\mathbf{k})$. So does λ_e, whereas the lattice thermal conductivity depends on phononic scattering time and phonon dispersion relation $\omega(\mathbf{k})$.

Carrier concentration

The materials of interest in the thermoelectric field are narrow-gap semiconductors, which is going to be reasoned in chapter 2. The type of charge carriers can therefore be both n-type and p-type, namely electrons and electron holes. The electronic properties S, σ and λ_e are strongly competing with another due to their strict dependence on the charge carrier concentration n, which can be seen in Figure 1.4 [12]. Thus, it is necessary to optimize the charge carrier concentration in a thermoelectric material, which can usually be achieved by doping other elements.

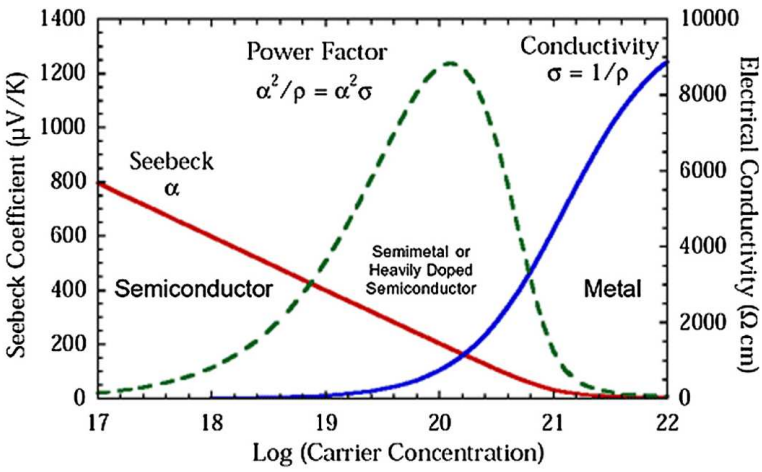

Figure 1.4: Carrier concentration dependence of Seebeck coefficient, electrical conductivity and power factor. Reproduced with permission from [12].

Die approbierte gedruckte Originalversion dieser Diplomarbeit ist an der TU Wien Bibliothek verfügbar.
The approved original version of this thesis is available in print at TU Wien Bibliothek.
TU Bibliothek Your knowledge hub WIEN

2 Theory

The theoretical background in the thermoelectric research field includes solid-state physics, materials science and solid-state chemistry. It is therefore, nearly, if not completely impossible to be an expert in the whole field due to the sheer complexity and magnitude of the topic. Nonetheless, this chapter will make an attempt to summarize the most important theoretical concepts for understanding transport phenomena in solids, that are necessary to comprehend the quality of a thermoelectric material. It is highly recommended however, to read further literature and be familiar with quantum mechanics, statistical physics and solid-state physics theory, as the concepts covered in this thesis will require background knowledge in those fields.

2.1 Schrödinger equation

The solid state can be categorised in amorphous, quasicrystalline and periodic crystals. In all of these cases the atoms have their more or less fixed positions in space, where they can only oscillate but not move freely. It is apparent that the type of crystal structure and the type of atoms, which are occupying the crystal structure are responsible for the type of chemical bonding and therefore also determine the chemical and physical properties of the system. In a quantum mechanical sense, we face a multibody Schrödinger equation problem:

$$\left[\sum_{n=1}^{N} \frac{-\hbar^2 \Delta_n}{2m_n} + V(\mathbf{r}_1, \mathbf{r}_2, ...\mathbf{r}_N, t)\right] \psi(\mathbf{r}_1, \mathbf{r}_2, ...\mathbf{r}_N, t) = E\psi(\mathbf{r}_1, \mathbf{r}_2, ...\mathbf{r}_N, t), \qquad (2.1)$$

with the first and second term on the left side of the equation representing the kinetic energy and the potential V and ψ being the electron wave function, which depends on time and the position vector of N electrons in three dimensional space. Δ_n is the Laplace operator and m_n the mass for the n-th electron. E are the energy eigenvalues of the Hamiltonian on the left side of the equation and $\hbar$ is the reduced Planck constant.
Considering a Si single crystal with $\approx 5\,\mathrm{g}$ for example, one has to deal with $\approx 10^{23}$ Si atoms with 14 electrons each that make this kind of approach for understanding macroscopic phenomena impossible, as the limit for an exact solution of the Schrödinger equation is already reached for the hydrogen atom with one electron.

Die approbierte gedruckte Originalversion dieser Diplomarbeit ist an der TU Wien Bibliothek verfügbar.
The approved original version of this thesis is available in print at TU Wien Bibliothek.
TU WIEN Bibliothek Your knowledge hub

2.2 Bloch's theorem

However, fortunately one does not have to consider $N \approx 10^{24}$ electrons. Due to the translational periodicity of the lattice in real space and reciprocal space, a calculation in the unit cell or first Brillouin zone (1^{st}BZ) is sufficient. The eigenvectors of our new Hamiltonian with the periodic potential are so-called Bloch waves:

$$\psi_{\mathbf{k}}(\mathbf{r}) = u_{\mathbf{k}}(\mathbf{r})e^{i\mathbf{kr}}, \tag{2.2}$$

where $u_{\mathbf{k}}(\mathbf{r}) = u_{\mathbf{k}}(\mathbf{r} + \mathbf{T})$ is a periodic function, that has to be multiplied with the plain wave term $e^{i\mathbf{kr}}$. $\mathbf{T}$ is a translational vector in real space.

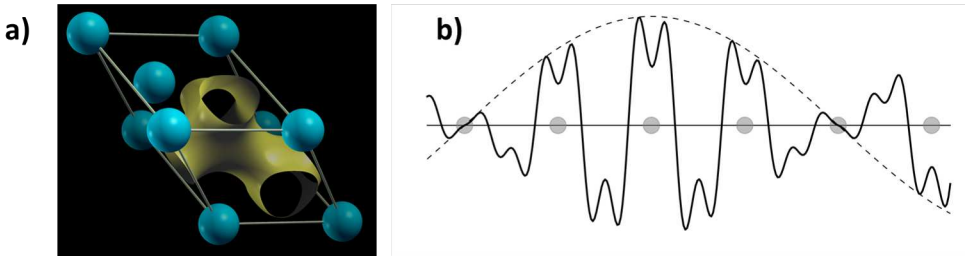

Figure 2.1: a) Square of the absolute value of a Bloch wave in a Si crystal. b) Real part of a typical Bloch wave with the plain wave term represented by the dotted line and atoms sitting in the lattice represented by the grey circles. Image taken from [65].

Because of the previously mentioned periodicity of the reciprocal lattice, one can assume:

$$\psi_{\mathbf{k}+\mathbf{G}}(\mathbf{r}) = \psi_{\mathbf{k}}(\mathbf{r}) \tag{2.3}$$

and

$$E(\mathbf{k} + \mathbf{G}) = E(\mathbf{k}), \tag{2.4}$$

with $\mathbf{G}$ being a reciprocal lattice vector. The energy eigenvalues in the 1^{st}BZ constitute the so-called electronic band structure $E(\mathbf{k})$, which is one of the most important concepts in order to understand transport phenomena in real crystal structures. It is for example directly related to the group velocity $\mathbf{v}_j$ and effective mass m^*_{ij}, which are frequently used parameters for evaluating the thermoelectric properties. We want to further explain these paramters and their importance in the following sections. It is also important to state that due to the nature of Bloch waves one cannot identify $\mathbf{k}$ with the momentum of the electrons like one would usually expect and therefore $\mathbf{p} \neq \hbar\mathbf{k}$, as can easily be shown:

$$-i\hbar\nabla\psi_{\mathbf{k}}(\mathbf{r}) = -i\hbar\nabla u_{\mathbf{k}}(\mathbf{r})e^{i\mathbf{kr}} = \hbar\mathbf{k}\psi_{\mathbf{k}}(\mathbf{r}) - e^{i\mathbf{kr}}\hbar\nabla u_{\mathbf{k}}(r). \tag{2.5}$$

Die approbierte gedruckte Originalversion dieser Diplomarbeit ist an der TU Wien Bibliothek verfügbar.
The approved original version of this thesis is available in print at TU Wien Bibliothek.
TU Bibliothek WIEN Your knowledge hub

Here $\psi_{\mathbf{k}}(\mathbf{r})$ is a Bloch wave and $-i\hbar\nabla$ is the momentum operator. We can conclude that the electrons in the crystal structure are periodic Bloch waves that are eigenvectors of a quantum system with a periodic potential. By solving the Schrödinger equation and obtaining the energy eigenvalues one can get the electronic band structure $E(\mathbf{k})$ of the system. Furthermore, we learned that $\hbar\mathbf{k}$ is not to be confused with the momentum of the electron as the Bloch wave functions are not eigenfunctions of the momentum operator and it is more correct to treat the wave vector $\mathbf{k}$ as a quantum number that describes a characteristic Bloch wave function.

For a more detailed derivation of Bloch's theorem it is recommended to read in chapter 7 of [51].

2.3 Boltzmann theory

The most commonly used theory for describing transport phenomena in crystalline solids is the Boltzmann theory, named after Austrian physicist Ludwig Boltzmann. It uses a semiclassical approach and explains the transport of charge and heat by electrons inside the crystal through exterior forces, more precisely the Lorentz force as well as by temperature gradients.

2.3.1 Group velocity

Using the picture of a moving particle, which can engage in transport phenomena, it makes sense to describe the electron as a wave packet or a superposition of Bloch waves:

$$\psi_{j,\mathbf{k}}(\mathbf{r},t) = \sum_{k-\Delta k/2}^{k+\Delta k/2} a(k) u_{\mathbf{k}}(\mathbf{r}) e^{i\left[\mathbf{kr} - \frac{E_j(\mathbf{k})}{\hbar} t\right]}. \tag{2.6}$$

The wave packet moves with a group velocity $\mathbf{v}(\mathbf{k})$ that depends on the wave vector $\mathbf{k}$ and leads to the equations of motion in the semiclassical model:

$$\frac{d\mathbf{r}}{dt} = \mathbf{v}(\mathbf{k}) = \frac{1}{\hbar}\frac{\partial E(\mathbf{k})}{\partial \mathbf{k}}, \tag{2.7}$$

$$\hbar\frac{d\mathbf{k}}{dt} = \mathbf{F}(\mathbf{r},t) = q\left[\mathbf{E}(\mathbf{r},t) + \mathbf{v}(\mathbf{k}) \times \mathbf{B}(\mathbf{r},t)\right], \tag{2.8}$$

where $\mathbf{E}(\mathbf{r},t)$ and $\mathbf{B}(\mathbf{r},t)$ are an electric and magnetic field respectively at a position $\mathbf{r}$ in space at a given time t, $\mathbf{v}(\mathbf{k})$ is the group velocity of a wave packet of Bloch waves and $E(\mathbf{k})$ is the electronic band structure. $\mathbf{F}(\mathbf{r},t)$ is the Lorentz force that acts on the electron.

Die approbierte gedruckte Originalversion dieser Diplomarbeit ist an der TU Wien Bibliothek verfügbar.
The approved original version of this thesis is available in print at TU Wien Bibliothek.
TU Bibliothek WIEN Your knowledge hub

2.3.2 Effective mass

By building the time derivative of the group velocity:

$$\frac{d\mathbf{v}(\mathbf{k})}{dt} = \frac{1}{\hbar}\frac{d}{dt}\frac{\partial E(\mathbf{k})}{\partial \mathbf{k}} \Rightarrow \frac{1}{\hbar}\sum_{j=1}^{3}\frac{\partial^2 E}{\partial k_i \partial k_j}\frac{\partial k_j}{\partial t} = \frac{1}{\hbar^2}\sum_{j=1}^{3}\frac{\partial^2 E}{\partial k_i \partial k_j}F_j, \tag{2.9}$$

one can see that, corresponding to $\mathbf{F} = m\mathbf{a}$, the following term represents the effective mass in the motion of equation of this system:

$$\left(m_{ij}^*\right)^{-1} = \frac{1}{\hbar^2}\frac{\partial^2 E}{\partial k_i \partial k_j}, \tag{2.10}$$

with m_{ij}^* being a tensor that represents the curvature of the band structure that can be positive or negative.

2.3.3 Boltzmann transport equation

The phase space is the number of possible positions (x, y, z) and wave vectors (k_x, k_y, k_z) any electron can take and the infinitesimal phase space volume is:

$$d^3\mathbf{r}d^3\mathbf{k} = dxdydzdk_xdk_ydk_z. \tag{2.11}$$

The distribution function $f = f(\mathbf{r}, \mathbf{k}, t)$ is the probability per unit phase-space volume to find an electron at the position $\mathbf{r}$ with a wave vector $\mathbf{k}$ at a certain time t. In thermal equilibrium and in the absence of external electromagnetic fields $f(\mathbf{r}, \mathbf{k}, t)$ becomes the Fermi-Dirac distribution function:

$$f_0(E(\mathbf{k})) = \frac{1}{e^{\frac{E(\mathbf{k})-\mu}{k_B T}} + 1}, \tag{2.12}$$

with μ being the chemical potential. The Fermi-Dirac distribution will change due to scattering processes and external electromagnetic fields $f_0 \Rightarrow f(\mathbf{r}, \mathbf{k}, t)$ and, under the consideration that scattering processes will not happen in an infinitesimal time interval $[t - dt, t]$, only the semiclassical equations Equation 2.7 and Equation 2.8 decide the position vectors and wave vectors $\mathbf{r}$ and $\mathbf{k}$. This means that inside of a small volume all electrons with $\mathbf{r}$ and $\mathbf{k}$ at the time t were at the position $\mathbf{r} - \mathbf{v}(\mathbf{k})dt$ and $\mathbf{k} - \frac{\mathbf{F}}{\hbar}dt$ at the time $t - dt$, as illustrated in Figure 2.2. Furthermore, we can say that the distribution functions at both times t and $t - dt$ have to be equal:

$$f(\mathbf{r}, \mathbf{k}, t) = f(\mathbf{r} - \mathbf{v}(\mathbf{k})dt, \mathbf{k} - \frac{\mathbf{F}}{\hbar}dt, t - dt) \tag{2.13}$$

and for the difference df per time interval length dt:

Die approbierte gedruckte Originalversion dieser Diplomarbeit ist an der TU Wien Bibliothek verfügbar.
The approved original version of this thesis is available in print at TU Wien Bibliothek.
TU Bibliothek WIEN Your knowledge hub

$$\frac{df}{dt} = \frac{f(\mathbf{r},\mathbf{k},t) - f(\mathbf{r}-\mathbf{v}(\mathbf{k})dt, \mathbf{k}-\frac{\mathbf{F}}{\hbar}dt, t-dt)}{dt} = 0. \tag{2.14}$$

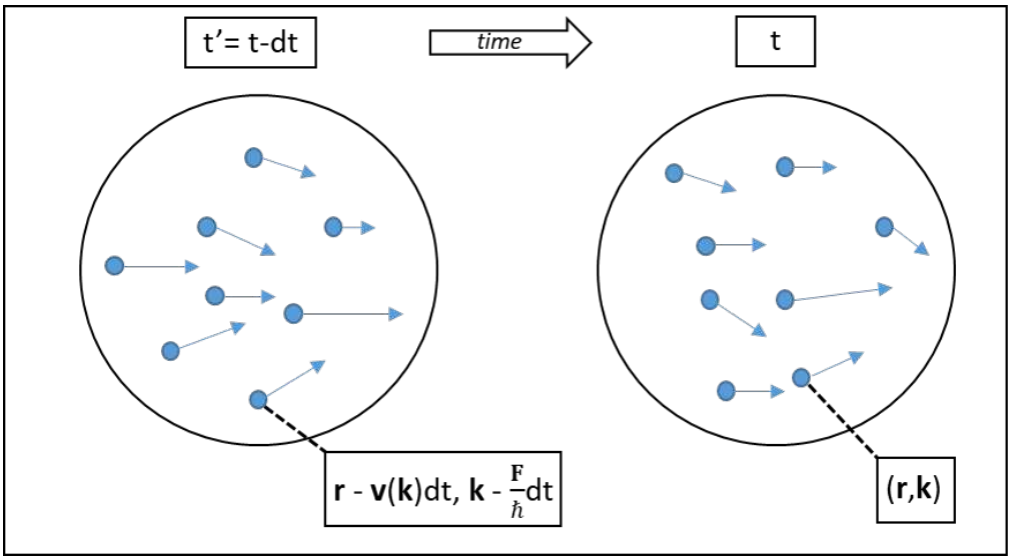

Figure 2.2: Changing **r**- and **k**-vectors in a time interval $[t-dt, t]$ due to external forces according to semiclassical equations.

Taking scattering processes into account, it is clear that the number of electrons at the time t has to be corrected because scattering can also lead to electrons being in the same volume with $(\mathbf{r},\mathbf{k})$. Therefore, a collision term is necessary for the correction of Equation 2.13 and Equation 2.14 and we get:

$$f(\mathbf{r},\mathbf{k},t) = f(\mathbf{r}-\mathbf{v}(\mathbf{k})dt, \mathbf{k}-\frac{\mathbf{F}}{\hbar}dt, t-dt) + \left(\frac{\partial f}{\partial t}\right)_{\text{collision}} dt \tag{2.15}$$

and the differential of the distribution function, such that:

$$\frac{df}{dt} = \frac{f(\mathbf{r},\mathbf{k},t) - f(\mathbf{r}-\mathbf{v}(\mathbf{k})dt, \mathbf{k}-\frac{\mathbf{F}}{\hbar}dt, t-dt)}{dt} = \left(\frac{\partial f}{\partial t}\right)_{\text{collision}}. \tag{2.16}$$

Under the assumption that dt is very small and therefore only terms of the first order of dt can be taken into account, the differential df/dt can be transformed into partial derivatives:

$$\frac{df}{dt} = \frac{\partial f}{\partial \mathbf{r}}\frac{\partial \mathbf{r}}{\partial t} + \frac{\partial f}{\partial \mathbf{k}}\frac{\partial \mathbf{k}}{\partial t} + \frac{\partial f}{\partial t} = \left(\frac{\partial f}{\partial t}\right)_{\text{collision}}. \tag{2.17}$$

Die approbierte gedruckte Originalversion dieser Diplomarbeit ist an der TU Wien Bibliothek verfügbar.
The approved original version of this thesis is available in print at TU Wien Bibliothek.
TU Bibliothek Your knowledge hub WIEN

Moreover, by using Equation 2.7 and Equation 2.8, we can rewrite Equation 2.17 into the so-called **Boltzmann transport equation**:

$$\frac{\partial f}{\partial t} = -\mathbf{v}\nabla_{\mathbf{r}} f + \frac{e}{\hbar}\left(\mathbf{E} + \mathbf{v} \times \mathbf{B}\right)\nabla_{\mathbf{k}} f + \left(\frac{\partial f}{\partial t}\right)_{\text{collision}}. \tag{2.18}$$

Here, the first term with $\nabla_{\mathbf{r}} f = \frac{\partial f}{\partial \mathbf{r}}$ is called the diffusion term, the second one is the contribution by the Lorentz force and the last one is the already mentioned collision term. The collision term is a non-trivial integral, that cannot be solved easily.

Relaxation time approximation

Because this complex collision term remains a problem, there have been made several attempts to simplify it, like the most commonly used relaxation time approximation:

$$\left(\frac{\partial f}{\partial t}\right)_{\text{collision}} = -\frac{f(\mathbf{r},\mathbf{k}) - f_0(\mathbf{r},\mathbf{k})}{\tau(\mathbf{r},\mathbf{k})} = -\frac{g(\mathbf{r},\mathbf{k})}{\tau(\mathbf{r},\mathbf{k})}, \tag{2.19}$$

with the electronic relaxation time $\tau(\mathbf{r},\mathbf{k})$ and Fermi distribution function $f_0(\mathbf{r},\mathbf{k})$ for the equilibrium state . The idea is that the non-equilibrium distribution function, induced by the effects of exterior forces on the particles, is lead back into an equilibrium state $f_0(\mathbf{r},\mathbf{k})$ by scattering processes. This can be easily understood when solving the relaxation time ansatz 2.19:

$$g(\mathbf{r},\mathbf{k},t) = g(\mathbf{r},\mathbf{k},0)e^{-t/\tau(\mathbf{r},\mathbf{k})}. \tag{2.20}$$

The deviation of the non-equilibrium function from the Fermi-Dirac function $f(\mathbf{r},\mathbf{k}) - f_0(\mathbf{r},\mathbf{k}) = g(\mathbf{r},\mathbf{k})$ exponentially decreases with the frequency $1/\tau(\mathbf{r},\mathbf{k})$. In the relaxation time approximation one can now attempt to calculate the non-equilibrium distribution $f(\mathbf{r},\mathbf{k},t)$. After a more detailed mathematical derivation, which is not going to be explained here but can be read in chapter 13 of [41], one eventually gets the solution of the Boltzmann transport equation:

$$f = f_0 + \int_{-\infty}^{t} P(t,t')\left[\left(-\frac{\partial f_0}{\partial E}\right)\mathbf{v}(\mathbf{k})\left(-e\mathbf{E} - \nabla_{\mathbf{r}}\mu - \left(\frac{E-\mu}{T}\right)\nabla_{\mathbf{r}} T\right)\right] dt', \tag{2.21}$$

with the energy $E = E(\mathbf{k})$ being the band structure, $f_0 = f_0(\mathbf{r},\mathbf{k})$ being the Fermi-Dirac distribution and $\mu = \mu(\mathbf{r})$ and $T = T(\mathbf{r})$ being the chemical potential and temperature respectively. $\mathbf{E}$ is an externally applied electric field. The term $P(t,t')$ gives the fraction of electrons, that can reach the phase space element $(\mathbf{r},\mathbf{k})$ at time t (see Figure 2.2) without collisions between t' and t. As shown in [41] it is related to the relaxation time $\tau(E(\mathbf{k}))$ in a simple differential equation with the solution:

Die approbierte gedruckte Originalversion dieser Diplomarbeit ist an der TU Wien Bibliothek verfügbar.
The approved original version of this thesis is available in print at TU Wien Bibliothek.
TU Bibliothek Your knowledge hub WIEN

$$P(t,t') = exp\left(-\int_{t'}^{t} \frac{d\tilde{t}}{\tau(E(\mathbf{k}))}\right). \tag{2.22}$$

The vectors $\mathbf{r} = \mathbf{r}(t')$ and $\mathbf{k} = \mathbf{k}(t')$ are trajectories of an electron of a given band, whose dependence on t' has been omitted in the previous equations in order to avoid any further obscurity of the already complex expressions. This very general term for $f(\mathbf{r}, \mathbf{k}, t)$ can be further simplified by making a few very plausible assumptions:

1) Electric fields and temperature gradients are considerably small.
2) The integrand in Equation 2.21 is independent of $\mathbf{r}(t')$.
3) Relaxation time depends only on the energy $E(\mathbf{k})$.

Given these simplifications, one can start deriving the electrical conductivity σ and Seebeck coefficient S, which are of interest for the thermoelectric figure of merit ZT (see Equation 1.3).

2.3.4 Electrical conductivity

In the case of a static electric field and constant chemical potential and temperature, Equation 2.21 takes the form of:

$$f(\mathbf{k}) = f_0(\mathbf{k}) - e\mathbf{E}\mathbf{v}(\mathbf{k})\tau(E(\mathbf{k}))\left(-\frac{\partial f_0(\mathbf{k})}{\partial E(\mathbf{k})}\right). \tag{2.23}$$

The infinitesimal particle current density by electrons with two possible spin directions can be defined as:

$$d\mathbf{j} = \mathbf{v}(\mathbf{k})\frac{1}{4\pi^3}d^3k, \tag{2.24}$$

where d^3k is a volume element in reciprocal space. By integration over the first Brillouin zone and multiplication with the electron charge $q = -e$, we can find the electronic current density:

$$\mathbf{j}_e = -\frac{e}{4\pi^3}\int_{1^{st}BZ} \mathbf{v}(\mathbf{k})f(\mathbf{k})d^3k. \tag{2.25}$$

We include the information about the occupied and unoccupied states via the previously derived distribution function $f(\mathbf{k})$. By combining Equation 2.23 and Equation 2.25 and taking the k-dependent electric field $\mathbf{E}$ out of the integrand, we can find Ohm's law $j_\nu = E^\mu\sigma_{\mu\nu}$, with the coefficient being the **electrical conductivity** tensor $\sigma_{\mu\nu}$:

$$\sigma_{\mu\nu} = e^2\int \frac{1}{4\pi^3}\tau(E(\mathbf{k}))v_\mu(\mathbf{k})v_\nu(\mathbf{k})\left(-\frac{\partial f_0(\mathbf{k})}{\partial E(\mathbf{k})}\right)d^3k. \tag{2.26}$$

Die approbierte gedruckte Originalversion dieser Diplomarbeit ist an der TU Wien Bibliothek verfügbar.
The approved original version of this thesis is available in print at TU Wien Bibliothek.
TU Bibliothek WIEN Your knowledge hub

The k-integration can be transformed into an integration over E with the definiton of the electronic density of states (DOS), $D(E)dE \equiv \frac{1}{4\pi^3}d^3k$. Thus, one gets:

$$\sigma = e^2 \int_{-\infty}^{\infty} D(E)\tau(E)\mathbf{v}(E)\mathbf{v}(E)\left(-\frac{\partial f_0(E)}{\partial E}\right)dE, \tag{2.27}$$

where $D(E)$ is the above mentioned DOS, which is the total number of states in an interval $[E, E + dE]$, which means the sum over all $\mathbf{k}$ for a given energy $E(\mathbf{k})$.

2.3.5 Seebeck coefficient

If, however, the temperature and chemical potential are not constants, we need to consider the gradients in chemical potential and temperature from Equation 2.21 and therefore get:

$$\mathbf{E} = \frac{\mathbf{j}_e}{\sigma} + S\nabla T - \frac{1}{e}\nabla\mu. \tag{2.28}$$

The coefficient S is the **Seebeck coefficient** and following analog steps, the expression for the Seebeck coefficient is:

$$S = \frac{-e}{\sigma}\int_{-\infty}^{\infty} dE D(E)\tau(E)\mathbf{v}(E)\mathbf{v}(E)\left(\frac{E-\mu}{T}\right)\left(-\frac{\partial f_0(E)}{\partial E}\right), \tag{2.29}$$

where σ is the previously derived electrical conductivity.
Because Boltzmann theory is a rather complicated and indistinct entry into understanding thermoelectrics, especially for beginners, a different approach is given in section 2.4 below. The derivation from Landauer theory, which was taken from [68], will lead to the exact same solutions for electrical conductivity and Seebeck coefficient, that were derived in this section.

2.4 Landauer theory

Another theory that has been developed as an alternative approach to Boltzmann theory in 1957 by Landauer offers a very intuitive way of understanding and describing both charge and heat transport. Assume that the particle current density through an infinitesimal slice of bulk material is given by:

$$\mathbf{j} = -q\int_{-\infty}^{\infty} G(E)\nabla F(E)dE, \tag{2.30}$$

where $G(E)$ is called *transport function*, which has positive values and will be specified in section 2.5, and $F(E)$ being a general particle distribution function, that can be the Fermi-Dirac distribution in the case of electron transport or the Bose-Einstein distribution in the case of phonon transport etc. The charge q can be the electric charge of electrons $-e$, but can also used for describing the heat, that

Die approbierte gedruckte Originalversion dieser Diplomarbeit ist an der TU Wien Bibliothek verfügbar.
The approved original version of this thesis is available in print at TU Wien Bibliothek.
TU WIEN Bibliothek Your knowledge hub

is carried by a particle as will be shown in subsection 2.4.2. The similar concept to Boltzmann theory is again the fact that voltage gradients and temperature gradients cause gradients in the particle distribution function, which will be the determining factor for the transport properties.

2.4.1 Charge transport

Firstly, the charge transport by electrons will be discussed by using Equation 2.30, where $q = -e$ is the electric charge for electrons and the distribution function $F(E) = f_0(E)$ is the Fermi-Dirac occupation statistics for electrons. Next, one needs to distinguish two cases how a gradient in the occupation statistics can arise.

Charge transport driven by voltage gradients

The electron transport induced from an electric field will be explained by using Landauer's approach. When applying a voltage gradient to a sample, this will lead to a gradient in chemical potential $\nabla\mu = -e\nabla V$, which will then result in a spatial gradient in occupation statistics:

$$\nabla f_0 = \frac{\partial f_0}{\partial x} = \frac{\partial f_0}{\partial \mu}\frac{\partial \mu}{\partial x}. \tag{2.31}$$

By looking at the derivatives of the Fermi-Dirac distribution (Equation 2.12), one can see that:

$$\frac{\partial f_0(\mu, E)}{\partial \mu} = -\frac{\partial f_0(\mu, E)}{\partial E}. \tag{2.32}$$

In the following we will omit the dependence on the chemical potential μ so that the relationship between a voltage gradient and gradient in occupation statistics is therefore given as per:

$$\nabla f_0 = (-e)\left(-\frac{\partial f_0(E)}{\partial E}\right)\nabla V. \tag{2.33}$$

By combining Equation 2.30 and Equation 2.33, one gets the current density for electron transport by a voltage gradient:

$$\mathbf{j}_{e,\nabla V} = -e^2\nabla V\int_{-\infty}^{\infty} G(E)\left(-\frac{\partial f_0(E)}{\partial E}\right)dE. \tag{2.34}$$

Using Ohm's law ($\mathbf{j}_{e,\nabla V} = -\sigma\nabla V$), once again we can extract the **electrical conductivity** and get:

$$\sigma = e^2\int_{-\infty}^{\infty} G(E)\left(-\frac{\partial f_0(E)}{\partial E}\right)dE. \tag{2.35}$$

Die approbierte gedruckte Originalversion dieser Diplomarbeit ist an der TU Wien Bibliothek verfügbar.
The approved original version of this thesis is available in print at TU Wien Bibliothek.
TU Bibliothek WIEN Your knowledge hub

By specifying the transport function $G(E)$ later, we will see that this is the exact same term as derived from the Boltzmann transport equation. The term $(-\partial f_0(E)/\partial E)$ is called *selection function* $\Phi_{\nabla V}$ for transport by a voltage gradient and decides which carriers are involved in transport. It is symmetric and positive for all energies E, as can be seen in Figure 2.3.

When increasing the temperature, the peak of $\Phi_{\nabla V}$ becomes smaller and the function broadens. When changing the chemical potential μ, $\Phi_{\nabla V}$ simply shifts to higher or lower energy values, as demonstrated in Figure 2.3. The convolution of this function with the energy dependent transport function gives the magnitude of the electrical conductivity σ. The consequences for the ideal electronic structure of a real material will be explained in detail in section 2.5.

Charge transport driven by temperature gradients

Another intuitive driving force for charge carriers are temperature gradients. High energy electrons should be transfered from the hot side to the cold side and low energy electrons the other way around. Again, Landauer theory aims to establish a relationship of a gradient in the Fermi-Dirac distribution ∇f_0 with a gradient in temperature ∇T. This results in:

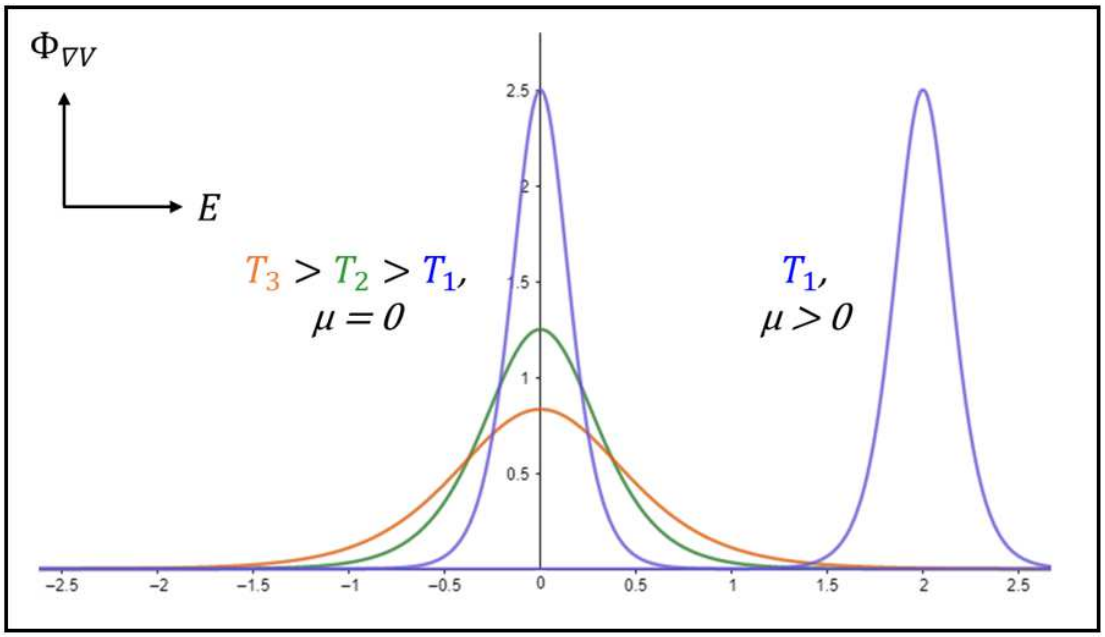

Figure 2.3: Selection function $\Phi_{\nabla V}$ for charge transport induced by a voltage gradient for different temperatures T_1, T_2, T_3 and different chemical potentials $\mu = 0, \mu > 0$.

Die approbierte gedruckte Originalversion dieser Diplomarbeit ist an der TU Wien Bibliothek verfügbar.
The approved original version of this thesis is available in print at TU Wien Bibliothek.
TU Bibliothek Your knowledge hub WIEN

$$\nabla f_0 = \frac{(E-\mu)}{T}\left(-\frac{\partial f_0(E)}{\partial E}\right)\nabla T \tag{2.36}$$

and

$$\mathbf{j}_{e,\nabla T} = e\nabla T \int_{-\infty}^{\infty} G(E)\frac{(E-\mu)}{T}\left(-\frac{\partial f_0(E)}{\partial E}\right) dE. \tag{2.37}$$

Analog to Ohm's law ($\mathbf{j}_{\nabla T} = -\nu\nabla T$), one can define the *Onsager coefficient* ν, that relates the current density to the magnitude of the temperature gradient:

$$\nu = -\frac{e}{T}\int_{-\infty}^{\infty} G(E)(E-\mu)\left(-\frac{\partial f_0(E)}{\partial E}\right) dE. \tag{2.38}$$

In contrary to the electrical conductivity, the selection function for transport induced by a temperature gradient $\Phi_{\nabla T}$, is an odd function with respect to the chemical potential because $(E-\mu)$ is an odd function around μ, as can be seen in Figure 2.4. This means that electrons above the Fermi energy will be driven from the hot end to the cold end, while electrons below the Fermi energy will be transported the opposite way. Subsequently, the integral, which is the convolution of the odd selection function $\Phi_{\nabla T}$ with the transport function $G(E)$, will give a negative value if the overlap of those functions is below the chemical potential and a positive value for energies above μ. This has consequences on what the ideal transport function should look like and will be explained in section 2.5. The current densities induced by a voltage gradient and a temperature gradient, which are $\mathbf{j}_{e,\nabla V}$, $\mathbf{j}_{e,\nabla T}$ respectively, can be additively written as:

$$\mathbf{j}_e = \mathbf{j}_{e,\nabla V} + \mathbf{j}_{e,\nabla T} = -\sigma\nabla V - \nu\nabla T. \tag{2.39}$$

The Seebeck effect is defined at open circuit conditions $\mathbf{j} = 0$ and the Seebeck coefficient is the ratio of the voltage difference and temperature difference:

$$S = \frac{\nu}{\sigma} = \frac{-e}{\sigma}\int_{-\infty}^{\infty} G(E)\left(\frac{E-\mu}{T}\right)\left(-\frac{\partial f_0(E)}{\partial E}\right) dE. \tag{2.40}$$

By particularizing the energy-dependent transport function $G(E)$ later, one will see, that Equation 2.29 and Equation 2.40 are indeed equal and the approach via Landauer theory is consistent with the results achieved by solving the Boltzmann equation. Finally, it can be concluded that charge transport is driven by temperature gradients and voltage gradients and the particles which take part in the transport phenomena have a particular energy range, which is set by the selection functions $\Phi_{\nabla V}$ and $\Phi_{\nabla T}$.

Die approbierte gedruckte Originalversion dieser Diplomarbeit ist an der TU Wien Bibliothek verfügbar.
The approved original version of this thesis is available in print at TU Wien Bibliothek.
TU WIEN Bibliothek Your knowledge hub

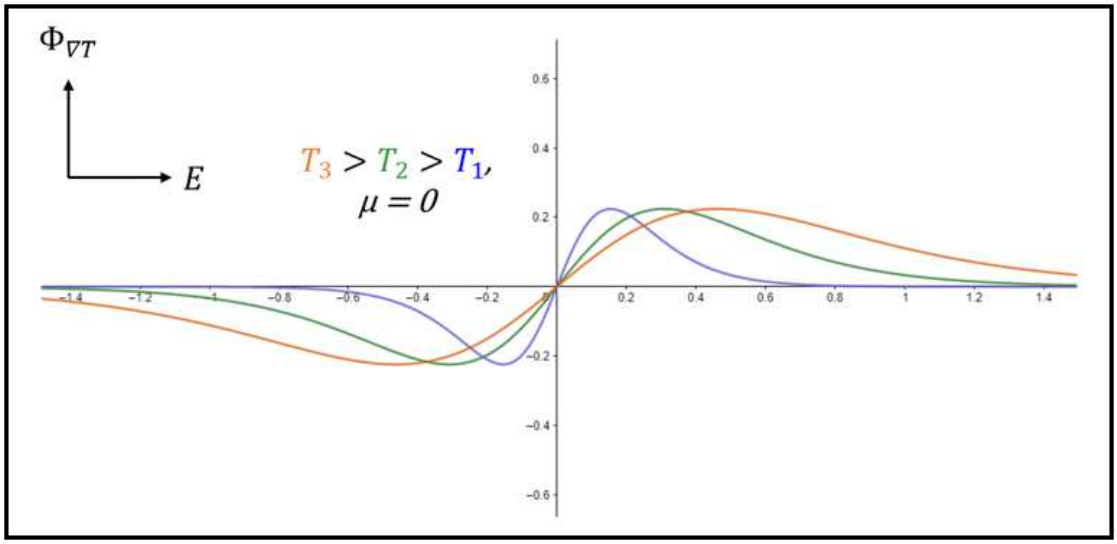

Figure 2.4: Selection function $\Phi_{\nabla T}$ for charge transport induced by a temperature gradient for different temperatures T_1, T_2, T_3 and with the chemical potential $\mu = 0$.

2.4.2 Heat transport

When describing heat transport with Landauer theory, one has to understand how the amount of heat $\delta\mathcal{Q}$ is related to the change of entropy $d\mathcal{S}$, associated with a particle. The second law of thermodynamics states:

$$\delta\mathcal{Q} = Td\mathcal{S}. \tag{2.41}$$

The entropy $\mathcal{S}$, that is defined as:

$$\mathcal{S} = k_B \log\Omega, \tag{2.42}$$

where Ω is the binomial coefficient:

$$\Omega = \binom{N}{c} = \frac{N!}{(N-c)!c!}, \tag{2.43}$$

changes, as a particle moves through a material. The binomial coefficient Ω gives the number of possible configurations for a number of c particles to occupy N given energy states.
Because heat can be carried by electrons, which are fermions, and phonons, which are bosons, one has to distinguish these two cases by using the Fermi-Dirac statistics $f_0(E)$ and the Bose-Einstein statistics $f_b(E)$, which considers the characteristic ability of bosons to occupy the same state at the same time without obeying the Pauli-exclusion principle. The Bose-Einstein distribution function is stated as:

Die approbierte gedruckte Originalversion dieser Diplomarbeit ist an der TU Wien Bibliothek verfügbar.
The approved original version of this thesis is available in print at TU Wien Bibliothek.
TU Bibliothek Your knowledge hub WIEN

$$f_b(E) = \frac{1}{e^{\frac{E}{k_B T}} - 1}. \tag{2.44}$$

The number of particles c is given by the product of the density of states with the respective distribution function $c = D(E)f_0(E), D(E)f_b(E)$. By using the correct combinatorics one gets:

$$\Omega_f(E) = \begin{pmatrix} D(E) \\ D(E)f_0(E) \end{pmatrix}, \tag{2.45}$$

$$\Omega_b(E) = \begin{pmatrix} D_b(E) + D_b(E)f_b(E) - 1 \\ D_b(E)f_b(E) \end{pmatrix}. \tag{2.46}$$

Now, by using Equation 2.42 as well as Equation 2.45 and Equation 2.46 respectively, one can calculate the change of entropy as a particle moves through the material. Under the assumption $D(E) \gg 1$, the change in entropy upon adding another particle, that can be fermionic or bosonic, is:

$$\frac{\partial \mathcal{S}_f}{\partial c} = \frac{E - \mu}{T}, \tag{2.47}$$

$$\frac{\partial \mathcal{S}_b}{\partial c} = \frac{E}{T}. \tag{2.48}$$

With the second law of thermodynamics, the change in entropy is related to the heat change, which is basically the heat carried by the particle as it moves through the material:

$$\frac{\partial \mathcal{Q}_f}{\partial c} = E - \mu, \tag{2.49}$$

$$\frac{\partial \mathcal{Q}_b}{\partial c} = E. \tag{2.50}$$

Like previously mentioned, the Landauer's theory is a very generalized approach and offers a way to describe both heat and charge transport in a similar way. The general term for the current density Equation 2.30 can be easily used to describe heat transport by identifying the general "charge" q in the equation with the heat carried by a particle $\frac{\partial \mathcal{Q}}{\partial c}$. Applying these concepts, the electronic and lattice thermal conductivity can now be derived.

Electronic thermal conductivity

When deriving the electronic thermal conductivity, we have to consider Equation 2.49 because the heat is carried by electrons. Likewise to subsection 2.4.1,

Die approbierte gedruckte Originalversion dieser Diplomarbeit ist an der TU Wien Bibliothek verfügbar.
The approved original version of this thesis is available in print at TU Wien Bibliothek.
TU Bibliothek WIEN Your knowledge hub

the current can be induced by voltage gradients and temperature gradients and the heat current densities for both cases are:

$$\mathbf{j}_{Q,\nabla V} = e\nabla V \int_{-\infty}^{\infty} G(E)(E-\mu)\left(-\frac{\partial f_0(E)}{\partial E}\right) dE, \tag{2.51}$$

$$\mathbf{j}_{Q,\nabla T} = -\nabla T \int_{-\infty}^{\infty} G(E)\frac{(E-\mu)^2}{T}\left(-\frac{\partial f_0(E)}{\partial E}\right) dE. \tag{2.52}$$

Because the selection function for electronic heat transport driven by temperature gradients:

$$\Phi_{Q,\nabla T} = (E-\mu)^2\left(-\frac{\partial f_0}{\partial E}\right) \tag{2.53}$$

,

is an even function, as can be seen in Figure 2.5, heat flow by electrons under a temperature gradient will always be from the hot side to the cold side like one would intuitively expect. Adding up the current densities for heat driven and voltage driven thermal transport to a total heat current $\mathbf{j}_Q = \mathbf{j}_{Q,\nabla V} + \mathbf{j}_{Q,\nabla T}$, one can find the electronic thermal conductivity λ_e from $\mathbf{j}_Q = -\lambda_e \nabla T$, which consists of two terms:

$$\lambda_e = \lambda_0 + \lambda_P = \int_{-\infty}^{\infty} G(E)\frac{(E-\mu)^2}{T}\left(-\frac{\partial f_0(E)}{\partial E}\right) dE - S^2\sigma T. \tag{2.54}$$

The first term is most commonly refered to as λ_0 and represents the thermal diffusion of electrons driven by a temperature gradient. The second term λ_P describes the self-Peltier effect [23], where heat is carried backwards from the high temperature to the low temperature end due to the applied thermoelectric voltage gradient.

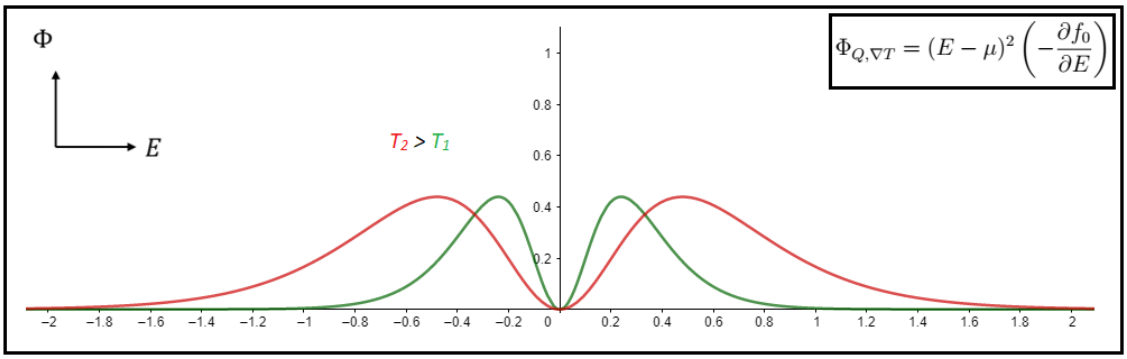

Figure 2.5: Selection function $\Phi_{Q,\nabla T}$ for thermal transport induced by a temperature gradient for different temperatures T_1, T_2 and with the chemical potential $\mu = 0$. The x-axis is energy. The units were chosen arbitrarily. The function is even and symmetric around the chemical potential.

Die approbierte gedruckte Originalversion dieser Diplomarbeit ist an der TU Wien Bibliothek verfügbar.
The approved original version of this thesis is available in print at TU Wien Bibliothek.
TU Bibliothek Your knowledge hub WIEN

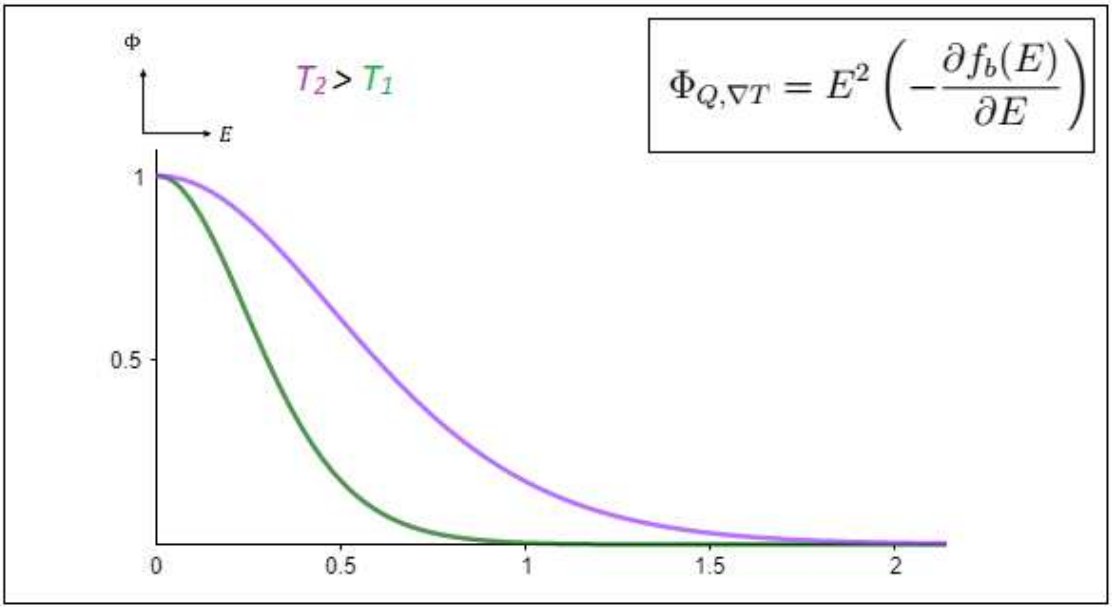

Figure 2.6: Selection function $\Phi_{Q,\nabla T}$ for phononic heat transport induced by a temperature gradient for different temperatures T_1, T_2. The x-axis is energy. The units were chosen arbitrarily.

Lattice thermal conductivity

The lattice thermal conductivity describes how effectively heat in a crystalline material is transported by phonons. Phonons are vibrational quanta in the crystal lattice that are affected by temperature gradients only. When treating phononic transport, one has to consider the previously specified Bose-Einstein statistics $f_b(E)$ and by employing the same methods as in the previous sections, the heat current density of phonons driven by a temperature gradient can be derived. This leads to the lattice thermal conductivity:

$$\lambda_{\text{lattice}} = \int_0^\infty G(E) \frac{(E)^2}{T} \left(-\frac{\partial f_b(E)}{\partial E} \right) dE. \tag{2.55}$$

2.5 The ideal transport function

The energy-dependent transport function $G(E)$ depends on the material and in the case of a crystalline material its crystal structure and electronic structure. Under the assumption that on average every particle scatters after a defined characteristic relaxation time $\tau(E)$, that depends on the energy of the particle, and that the collective transport of all particles is simply related to their average squared

Die approbierte gedruckte Originalversion dieser Diplomarbeit ist an der TU Wien Bibliothek verfügbar.
The approved original version of this thesis is available in print at TU Wien Bibliothek.
TU Bibliothek WIEN Your knowledge hub

velocity $\langle \mathbf{v}(E)^2 \rangle$, the transport function takes the same form as when the transport properties were dervied from the Boltzmann equation in subsection 2.3.4:

$$G(E) = D(E)\tau(E)\langle \mathbf{v}(E)^2 \rangle. \tag{2.56}$$

One can now see that the transport function includes the energy dependence of the density of states $D(E)$, the squared group velocity and the electron scattering time. The density of states, from now on refered to as DOS, and group velocity are directly related to the band structure $E(\mathbf{k})$. The group velocity is the derivative of $E(\mathbf{k})$ and the DOS is the sum over all $\mathbf{k}$-vectors for a given energy E. When thinking in the single parabolic band model, this means that highly dispersive bands will result in a high $\langle \mathbf{v}(E)^2 \rangle$-term, whereas flat bands will result in a high $D(E)$. The scattering time is often considered constant or $\tau(E) \sim E^{\delta}$ at temperatures above room temperature, where δ depends on the type of scattering process. The ideal transport function for an optimal power factor $S^2\sigma$ would be a Dirac delta function, which would require a very high DOS and a very high group velocity at the same time [32]. This can easily be understood when looking at the shape of the selection function for charge transport driven by temperature gradients as in Figure 2.4. The convolution of the odd selection function with a transport function, that has positive values over a wider range of E in both directions of the chemical potential, would result in a cancellation of the negative and positive surface area. Therefore a transport function, which overlaps with only one of the both surfaces, is desirable. Such a $G(E)$ is achieved by a high DOS that has a steep slope together with a high carrier mobility, achieved by high group velocities $\mathbf{v}(E)$. In reality this means that a narrow gap semiconductor with a well defined band gap E_g and a large DOS with a steep slope is necessary for a well performing thermoelectric material. A better understanding of the previous statements is obtained when looking at the ideal position of the Fermi energy or chemical potential.

2.6 The ideal position of the Fermi energy

The Fermi energy is the chemical potential at absolute zero temperature: $E_F = \mu(T = 0)$. Because the electronic structure does not substantially change as a function of temperature, if there is not some kind of phase transition, one can equally refer to the chemical potential as Fermi energy. The Fermi energy can be controlled by doping elements and represents the energy of the electron with the highest energy at 0 K. In an undoped semiconductor the Fermi energy is positioned in the middle of the band gap where $D(E) = 0$. Therefore, both the Seebeck coefficient S and the electrical conductivity σ will be zero. At temperatures $T > 0\,\mathrm{K}$, carriers which have energies about $\pm 1.5 k_B T$ below and above the Fermi energy will be engaged in transport. Depending on the size of the band gap, this will result in a power factor $S^2\sigma > 0$. However, the ideal position for the Fermi energy is near

Die approbierte gedruckte Originalversion dieser Diplomarbeit ist an der TU Wien Bibliothek verfügbar.
The approved original version of this thesis is available in print at TU Wien Bibliothek.
TU Bibliothek Your knowledge hub WIEN

a band edge, where the DOS is small but its slope is high. When looking at Figure 2.3 and Figure 2.4, this becomes easily understandable. If the Fermi energy and therefore the position of the selection functions is too far from either band edge there will be no overlap and the thermoelectric properties will be small. If however, the Fermi energy is shifted too far into the band, the odd selection function for temperature driven transport will bring a cancellation of charge carriers because the overlap of $D(E)$ and $\Phi_{e,\nabla T}$ is too big. This fact is also represented by the well known Mott formula:

$$S(T) \propto -T \left(\frac{1}{D(E)} \frac{\partial D(E)}{\partial E} \right)_{E_F} . \tag{2.57}$$

If the Fermi energy is positioned at a negative slope of $D(E)$ - this means in the valence band edge - the Seebeck coefficient has a positive sign and the main charge carriers will be holes. Carrier doping that leads to a shift of E_F into the conduction band edge will result in a negative Seebeck coefficient and in a n-type material. Figure 2.7 and Figure 2.8 show how the selection functions $\Phi_{e,\nabla V}$ and $\Phi_{e,\nabla T}$ sample the electronic DOS $D(E)$. In the parabolic band model one can assume $D(E) \propto \sqrt{E}$ and $\mathbf{v}^2(E) \propto E$. Even though different scattering mechanisms yield different T-dependences of $\tau(E)$ (Dominant phonon scattering: $T^{-\frac{1}{2}}$ in covalent bonds, T^{-1} in metals, $T^{-\frac{3}{2}}$ in ionic compounds, Ionic impurity scattering: $\tau \propto T^{\frac{3}{2}}$), the scattering time is often considered a constant ($\approx 1 \times 10^{-14}$ s) due to a lack of knowledge and for reasons of simplification [23].

A metallic electronic structure, which is a band structure with no bandgap around the Fermi energy, will always result in very low Seebeck coefficients for previously described reasons. Metals are therefore not suited candidates for thermoelectrics.

In summary, one can say that a narrow gap semiconductor with a DOS that rises sharply in both directions of the Fermi energy is ideal for a thermoelectric material because the chemical potential can easily be shifted towards either edge of the valence band or conduction band to achieve high absolute values of the powerfactor:

$$S^2\sigma = \frac{\left[\int_{-\infty}^{\infty} G(E) \frac{(E-\mu)}{T} \left(-\frac{\partial f_0(E)}{\partial E} \right) dE \right]^2}{\int_{-\infty}^{\infty} G(E) \left(-\frac{\partial f_0(E)}{\partial E} \right) dE}. \tag{2.58}$$

Because the numerator of the equation has the odd function $(E - \mu)$ the ideal position for μ is near the edge of either electronic band. The Seebeck coefficient decreases for the same reason if the band gap closes.

Die approbierte gedruckte Originalversion dieser Diplomarbeit ist an der TU Wien Bibliothek verfügbar.
The approved original version of this thesis is available in print at TU Wien Bibliothek.
TU Bibliothek Your knowledge hub WIEN

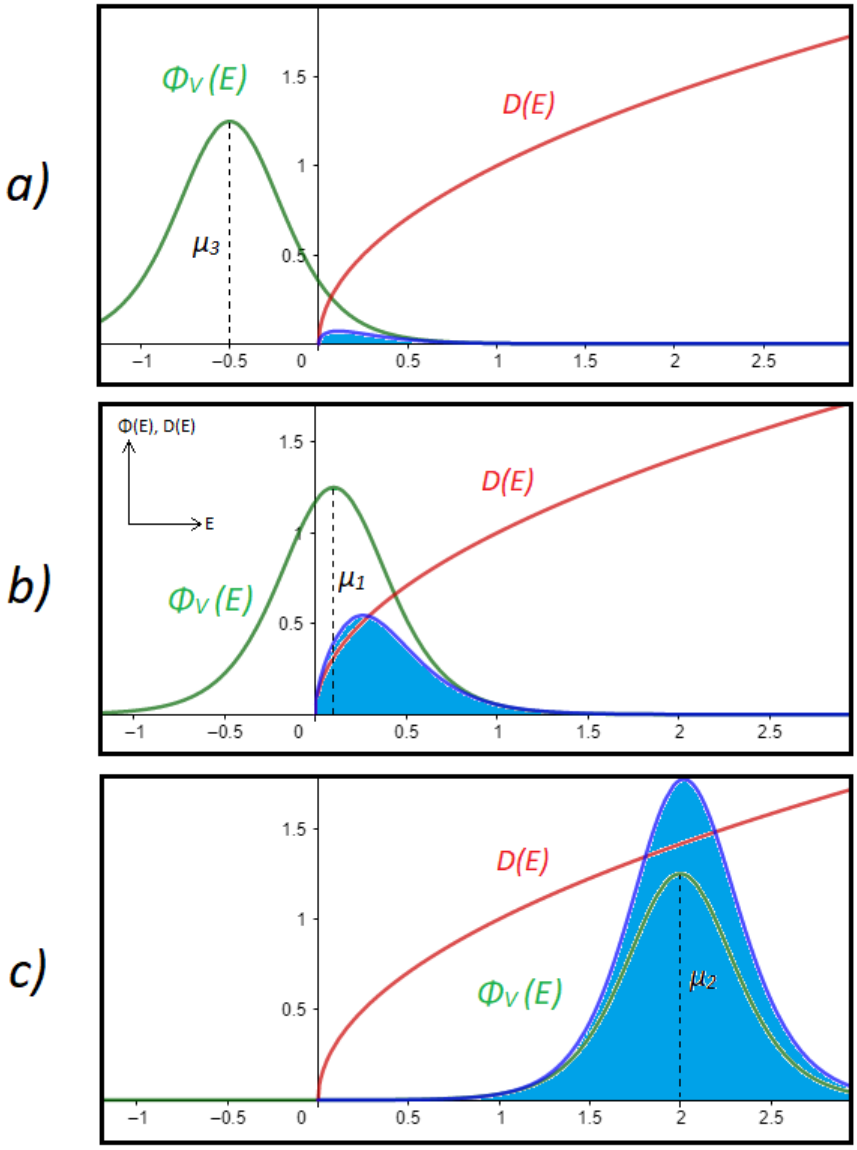

Figure 2.7: Position of the chemical potential a) in the band gap , b) at the conduction band edge and c) far into the conduction band. The blue area represents the convolution of the DOS $D(E)$ with the selection function for voltage driven charge transport $\Phi_{e,\nabla V}$. The electrical conductivity σ increases into the band because more charge carriers are available for transport. Inside the bandgap there are almost no available charge carriers at lower temperatures and the surface area becomes almost zero and for that reason: $\sigma \longrightarrow 0$.

Die approbierte gedruckte Originalversion dieser Diplomarbeit ist an der TU Wien Bibliothek verfügbar.
The approved original version of this thesis is available in print at TU Wien Bibliothek.
TU Bibliothek Your knowledge hub WIEN

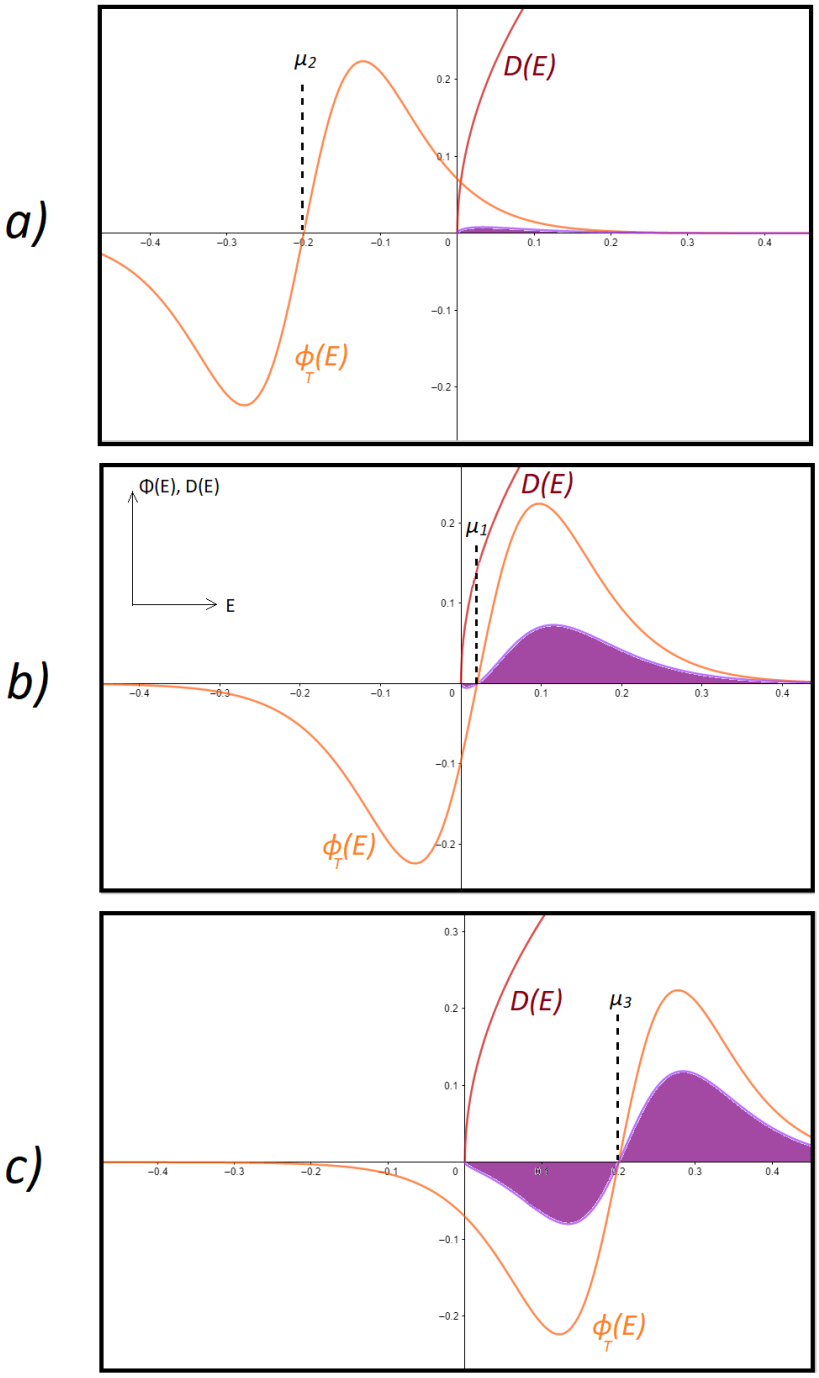

Figure 2.8: Fermi level a) in the band gap, b) at the conduction band edge and c) far into the conduction band. The purple area represents the convolution of the DOS $D(E)$ with the selection function for charge transport driven by temperature gradients $\Phi_{e,\nabla T}$. The integral decreases into the band due to a cancellation of charge carriers above and below μ. The optimal position is near the band edge of the conduction band where the area below the chemical potential becomes almost zero.

Die approbierte gedruckte Originalversion dieser Diplomarbeit ist an der TU Wien Bibliothek verfügbar.
The approved original version of this thesis is available in print at TU Wien Bibliothek.
TU Bibliothek Your knowledge hub WIEN

2.7 Band convergence and valley degeneracy

After having understood the previous sections and figures it should be clear that a high DOS is desirable. This leads to the wrong assumption that a high effective mass m^* is sufficient for a high power factor as a heavy band intrinsically means that the electronic DOS is large. While this assumption is partly true a flat and heavy band also means that the carrier mobility is significantly reduced as $\mathbf{v}(E) \propto \partial E(\mathbf{k})/\partial \mathbf{k}$ and therefore the power factor will remain low. The concept of band convergence solves that problem. Converging many dispersive bands, also called carrier pockets or valleys, leads to a high DOS. The valley degeneracy N_V, which is the number of valence band maxima or conduction band minima at a given energy for different reciprocal vectors $\mathbf{k}$ is directly related to the electronic density of states $D(E)$. N_V becomes especially high if the convergence of electronic bands happens at low symmetry points in the first Brillouin zone, which is a truncated octahedron for fcc structures as sketched in Figure 2.9.

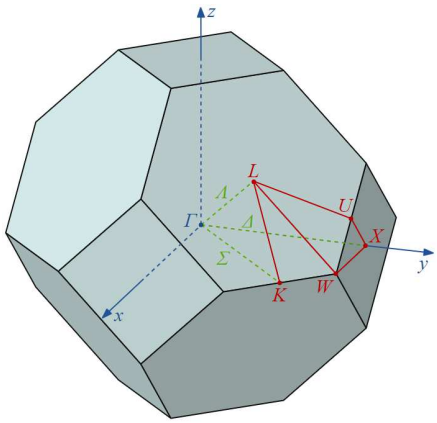

Figure 2.9: First Brillouin zone for a fcc crystal structure with the high symmetrical points W, L, Γ, X, U and K. Σ, Δ and Λ are high symmetry lines that connect the Γ-point with other symmetrical points like illustrated. The x-, y- and z-axis are in reciprocal space. Image taken from [66].

In this case, the Γ-point has the highest symmetry and the valley degeneracy is the lowest. In the case of the X-point however, the degeneracy of carrier pockets is sixfold or eightfold in the case of the L-point, because there are different but equivalent $\mathbf{k}$-directions where those points can be mirrored as can bee seen in Figure 2.10 and Figure 2.11 [45]. Although N_V is at its highest when the bands are exactly degenerate, a many band contribution can be expected when the energy seperation between the bands is small in comparison to $k_B T$. The mobility is almost unswayed by converging bands while the DOS is increased at the same time [45]. Thus, the search for compounds that show a high value of N_V has become a key strategy for improving the ZT. Said strategy is called band engineering and

Die approbierte gedruckte Originalversion dieser Diplomarbeit ist an der TU Wien Bibliothek verfügbar.
The approved original version of this thesis is available in print at TU Wien Bibliothek.
TU Bibliothek Your knowledge hub WIEN

although most compounds with a high valley degeneracy are found by accident, the recent advances in DFT calculations have proven to be an advantageous and helpful tool for predicting new promising thermoelectric materials with a high powerfactor. The following section shall give a short introduction and rough overview into what DFT calculation and theory is based on and how it is most commonly used.

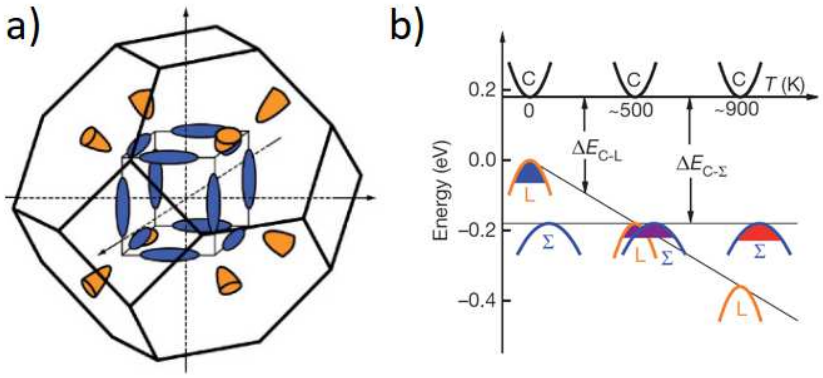

Figure 2.10: a) Fermi surface of the valence band structure of $PbTe_{1-x}Se_x$ showing the eightfold degenerate hole half-pockets at the L point in yellow color and the hole pockets along the Σ line with $N_V = 12$ in blue. b) shows the band convergence of the L and Σ bands at 500 K. Reproduced with permission from [45].

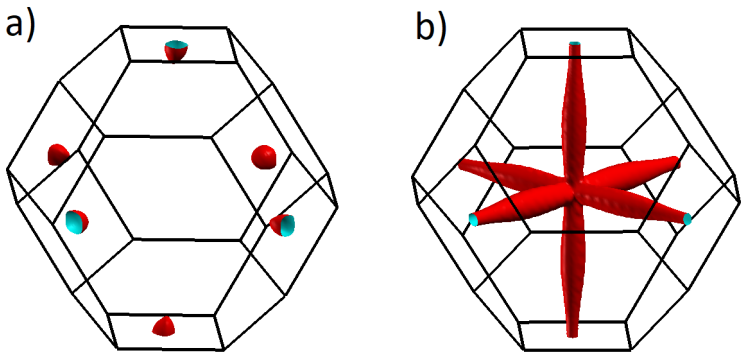

Figure 2.11: a) Fermi surface of the conduction band of Fe_2VAl with sixfold degeneracy at the X point coming from the conduction band minimum controlled by vanadium. b) Orthogonal, tubular Fermi surface of Fe_2TiSn coming from the heavy flat band along the Γ-X direction. Reproduced with permission from [4].

Die approbierte gedruckte Originalversion dieser Diplomarbeit ist an der TU Wien Bibliothek verfügbar.
The approved original version of this thesis is available in print at TU Wien Bibliothek.
TU Bibliothek Your knowledge hub WIEN

2.8 Density functional theory and band structure calculation

The band structure is essential for understanding the quality and performance of bulk thermoelectric materials. Thus, it would be of great interest to calculate the band structure in advance. Like previously established, the electronic band structure $E(\mathbf{k})$ is represented by the energy eigen values of the Schrödinger equation in a periodic potential. However, calculating the ground state energy and wave functions of this many body Schrödinger equation (see Equation 2.1) is impossible. For that reason, so-called density functional theory DFT, which became popular in the 1990s in quantum chemistry [6] and solid state physics, provides a solution to significantly reduce the high dimensional problem by using the electronic density $n(\mathbf{r})$:

$$n(\mathbf{r}) = N \int d^3r_2 \int d^3r_3 ... \int d^3r_N |\Psi(\mathbf{r}, \mathbf{r}_2 ..., \mathbf{r}_N)|^2, \tag{2.59}$$

which when multiplied with d^3r is the probability to find an electron in the infinitesimal region d^3r. [8]
Because DFT calculations do not require any knowledge of material parameters or any other higher order quantities but instead are derived directly from quantum theory they are also often called *ab initio* or *first principles* calculations.

2.8.1 Hohenberg-Kohn theorems

For simplification, the Coulomb interaction from the nuclei of the atoms is treated as an external potential V_{ext} in which the electrons move. The heart of density functional theory are the so-called Hohenberg-Kohn theorems.

1st theorem:

The first theorem (see Figure 2.12) states that the above mentioned external potential is a unique functional of the electronic particle density $n(\mathbf{r})$. This implies, that all other properties such as the energy and wave function are functionals of the electron density as well:

$$V_{ext} = V_{ext}[n] \rightarrow E = E[n], \Psi = \Psi[n]. \tag{2.60}$$

2nd theorem:

The second theorem states that the energy E can be minimized until the ground state energy E_0 is found if the ground state wave function Ψ_0 can reproduce the real

Die approbierte gedruckte Originalversion dieser Diplomarbeit ist an der TU Wien Bibliothek verfügbar.
The approved original version of this thesis is available in print at TU Wien Bibliothek.
TU Bibliothek Your knowledge hub WIEN

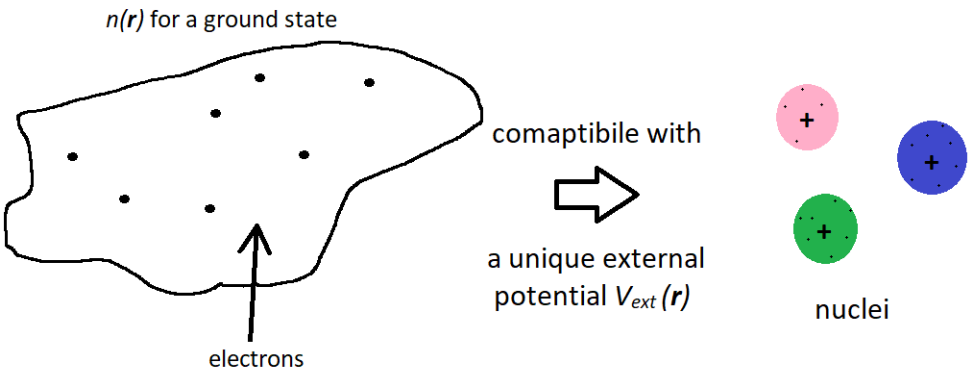

Figure 2.12: Schematic visualisation of the first Hohenberg-Kohn theorem: the electron density for a ground state defines a unique number of electrons and corresponds to a unique constellation of nuclei. Therefore the potential V_{ext} is defined by the electronic density function $n(\mathbf{r})$ [13].

ground state density n_0. More precisely, one has found the ground state electron density if the energy functional can be minimized by that ground state density:

$$E_0 = \min_{n \to n_0} \langle \Psi[n] | \hat{H}[n] | \Psi[n] \rangle, \tag{2.61}$$

where $\hat{H} = \hat{T} + \hat{U} + \hat{V}_{ext}$ is the Hamiltonian that consists of the kinetic energy term $\hat{T}$, the electron-electron interaction term $\hat{U}$ and the already mentioned external potential $\hat{V}_{ext}$. The total energy functional $E[n] > E_0[n_0]$ can be written as:

$$E[n] = \min_{n \to n_0} \langle \Psi[n] | \hat{T}[n] + \hat{U}[n] | \Psi[n] \rangle + \int n(\mathbf{r}) V_{ext}(\mathbf{r}) d^3r. \tag{2.62}$$

If $n = n_0$ and the energy can no longer be minimized, the wave function Ψ will be the ground state of the system Ψ_0 that self-consistently reproduces the ground state density $n_0(\mathbf{r})$ [8].

2.8.2 Kohn-Sham equations

The electron-electron interaction $\hat{U}[n]$ can be separated in a Hatree-Fock energy $E_H[n]$ and an exchange-correlation potential $v_{XC}[n]$ that includes other quantum mechanical effects and in general is very complicated to estimate correctly:

$$\hat{U}[n] = E_H[n] + v_{XC}[n] = e^2 \int \frac{n(\mathbf{r}')}{|\mathbf{r} - \mathbf{r}'|} d^3r' + v_{XC}[n]. \tag{2.63}$$

It is this unknown term which is the main reason for uncertainty in electronic

Die approbierte gedruckte Originalversion dieser Diplomarbeit ist an der TU Wien Bibliothek verfügbar.
The approved original version of this thesis is available in print at TU Wien Bibliothek.
TU Bibliothek WIEN Your knowledge hub

structure calculations. Now, one can rewrite the many body Schrödinger equation of many interacting electrons to many non-interacting one-electron equations also called Kohn-Sham equations:

$$\left(\hat{T} + \hat{v}_{KS}\right) |\phi_i\rangle = \epsilon_i |\phi_i\rangle. \tag{2.64}$$

The single-electron eigen functions $\phi_i(\mathbf{r})$ and the corresponding eigen energy values ϵ_i need to be calculated and represent the band structure $\epsilon_i(\phi_i) \rightarrow E(\mathbf{k})$. The calculated wave functions $\phi_i(\mathbf{r})$ are used to calculate the electron density $n(\mathbf{r})$ which is then again used for calculating a new set of $\phi_i(\mathbf{r})$. This self-consistent iteration is repeated until the ground state energy is found. The second term in the Hamiltonian is the effective Kohn-Sham potential v_{KS} in which the electrons move and which contains the previously mentioned terms:

$$v_{KS}(\mathbf{r}) = V_{ext}(\mathbf{r}) + e^2 \int \frac{n(\mathbf{r}')}{|\mathbf{r} - \mathbf{r}'|} d^3r' + v_{XC}(\mathbf{r}). \tag{2.65}$$

The exchange correlation term and its corresponding energy E_{XC}:

$$v_{XC}(\mathbf{r}) \equiv \frac{\delta E_{XC}[n]}{\delta n(\mathbf{r})} \tag{2.66}$$

are unknown and need to be approximated. The most commonly used and easiest approximations are the local density approximation LDA and the general gradient approximation GGA, which are briefly introduced in the following.

Local density apprixomation:

The LDA like its name suggests solely considers the local density at the coordinate where the functional is evaluated [7]:

$$E_{XC}^{LDA} = \int \Upsilon_{XC}(n_\uparrow(\mathbf{r}), n_\downarrow(\mathbf{r})) d^3r, \tag{2.67}$$

with the exchange-correlation density Υ_{XC} and the electron densities for spin-up and spin-down electrons $n_\uparrow(\mathbf{r}), n_\downarrow(\mathbf{r})$. In the case of strongly correlated electron systems the LDA fails to reproduce correct values for the electronic structure and there have been made attempts to combine concepts of the LDA with other theoretical models for strongly interacting systems like the Hubbard model. One of those attempts is the LDA+U approximation, which frequently appears in literature.

General gradient approximation

As already mentioned the LDA has its limits and often underestimates the bandgap up to 40% [46]. Another commonly used approximation is the GGA which takes

Die approbierte gedruckte Originalversion dieser Diplomarbeit ist an der TU Wien Bibliothek verfügbar.
The approved original version of this thesis is available in print at TU Wien Bibliothek.
TU Bibliothek WIEN Your knowledge hub

into account that the energy density depends on the gradient of the electronic density as well [7, 47]:

$$E_{XC}^{GGA} = \int \Upsilon_{XC}(n_\uparrow(\mathbf{r}), n_\downarrow(\mathbf{r}), \nabla n_\uparrow(\mathbf{r}), \nabla n_\downarrow(\mathbf{r}))d^3r. \tag{2.68}$$

There are many other approximations, that will not be presented in this work and which have a higher accuracy than the GGA (e.g. meta-GGA, hyper-GGA). However, they are often not necessary or take too much calculation time. If a more profound understanding of density functional theory is desired, one can find an in-depth discussion of DFT and related topics in [6, 8].

2.9 Photoemission spectroscopy as a way to study the electronic structure

In the previous sections it was established that there are mainly two intrinsic factors responsible for the thermoelectric powerfactor $S^2\sigma$: First of all the nature of the electronic band structure and secondly the position of the Fermi level E_F. Since first-principle calculations still have a lot of limitations and it would be of great interest to probe the electronic structure experimentally, some methods to examine the electronic structure of materials have been developed. One of those methods is photoemission electron spectroscopy (PES). PES techniques allow to investigate the valence band structure of a sample by calculating the binding energy E_B of electrons that are emitted due to the photoelectric effect:

$$E = \hbar\omega - E_B - \Phi, \tag{2.69}$$

where E is the measured kinetic energy of the emitted electron, $\hbar\omega$ is the photon energy and Φ is the so-called work function that represents the minimum energy required to remove an electron. While conventional spectroscopic methods can only give an integrated spectrum over all energy states (DOS of the valence band), angle-resolved photo emission spectroscopy (ARPES) poses a highly advanced and powerful tool for preserving the information about the **k**-space of valence electrons. A schematic representation of an experimental ARPES set-up is shown in Figure 2.13.

The momentum of the outgoing electron, whose energy can be detected at a certain angle, is related to the in-crystal electrons through the conservation of momentum and energy. For the parallel components of the **k**-vector translational symmetry yields $k_\parallel = k'_\parallel$ where $k_\parallel$ and $k'_\parallel$ are the k-components in the plane of the crystal surface as depicted in Figure 2.14. Because the components perpendicular to the surface are usually not conserved $k_\perp \neq k'_\perp$ one frequently makes the assumption of a free-electron-like dispersion for the final states:

Die approbierte gedruckte Originalversion dieser Diplomarbeit ist an der TU Wien Bibliothek verfügbar.
The approved original version of this thesis is available in print at TU Wien Bibliothek.
TU Bibliothek WIEN Your knowledge hub

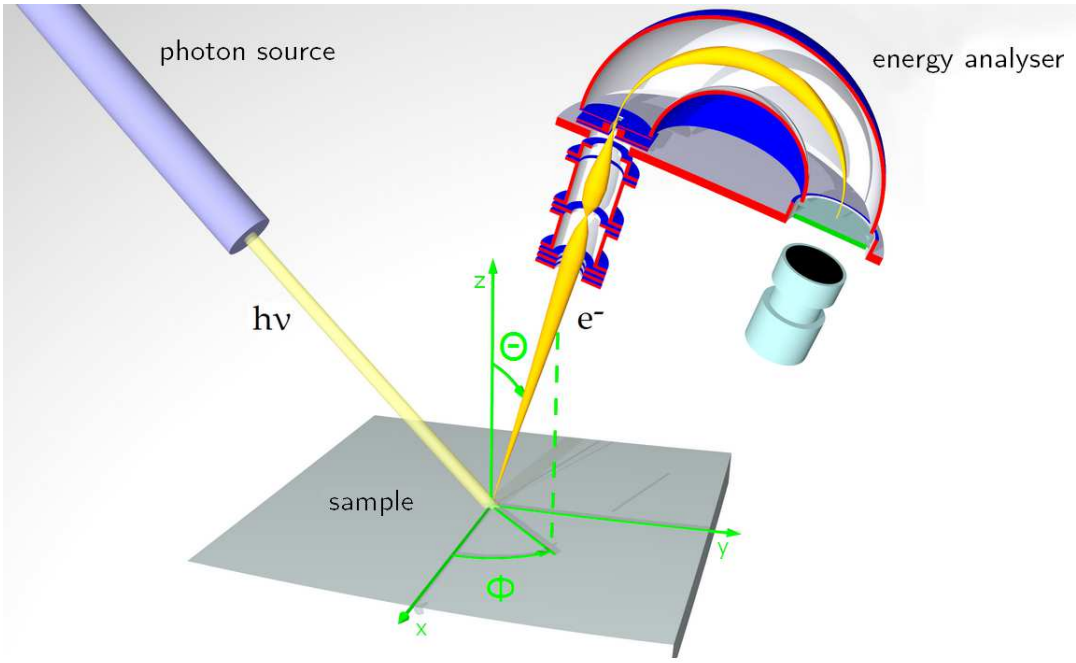

Figure 2.13: Demonstration of the ARPES method: The sample is exposed to a photon beam with a defined energy $h\nu$ and electrons in the surface of the sample get emitted at different angles, which are then measured. Image taken from [64].

$$E_f(\mathbf{k}) \approx \frac{(\mathbf{k}+\mathbf{G})^2}{2m^*} + V_0, \tag{2.70}$$

with the reciprocal lattice vector $\mathbf{G}$, the effective mass m^* and the band depth from vacuum V_0 that is related to the workfunction via $V_0 = \Phi + (E_{vac} - E_F)$ with the vacuum level E_{vac} [29]. This assumption is almost correct for materials with simple Fermi surfaces of nearly spherical topology and one gets [9]:

$$k_{\parallel} = \frac{1}{\hbar}\sqrt{2mE}\sin\theta \tag{2.71}$$

and

$$k_{\perp} = \frac{1}{\hbar}\sqrt{2m(E\cos^2\theta + V_0)}. \tag{2.72}$$

By solving Equation 2.71 and Equation 2.72 together with Equation 2.69 one can find the dispersion relation between the binding energy E_B and $\mathbf{k}$. Derivations and formulae were taken from [9, 29].

Die approbierte gedruckte Originalversion dieser Diplomarbeit ist an der TU Wien Bibliothek verfügbar.
The approved original version of this thesis is available in print at TU Wien Bibliothek.
TU Bibliothek WIEN Your knowledge hub

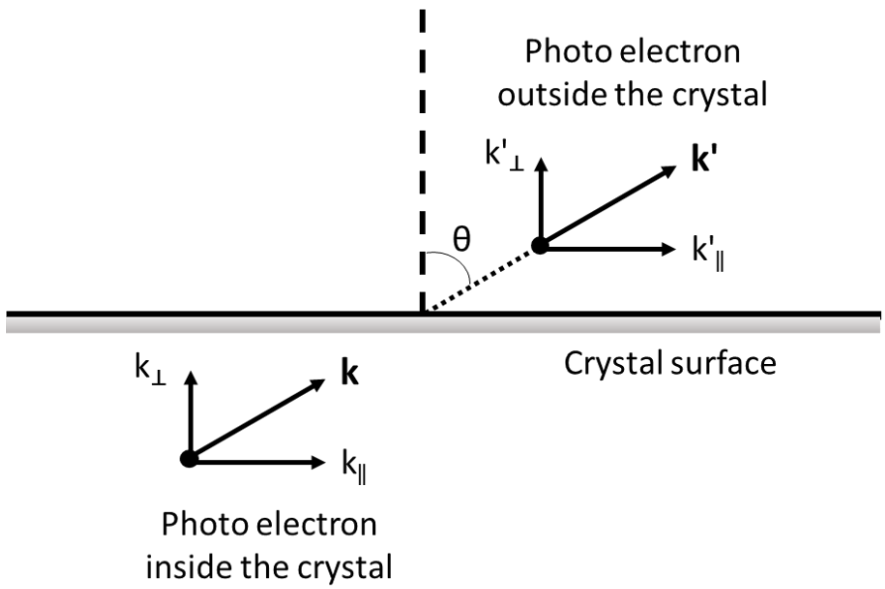

Figure 2.14: Geometrical demonstration of how a photo-electron inside the crystal leaves the crystal surface into vacuum under an angle θ.

Die approbierte gedruckte Originalversion dieser Diplomarbeit ist an der TU Wien Bibliothek verfügbar.
The approved original version of this thesis is available in print at TU Wien Bibliothek.
TU Bibliothek Your knowledge hub WIEN

Die approbierte gedruckte Originalversion dieser Diplomarbeit ist an der TU Wien Bibliothek verfügbar.
The approved original version of this thesis is available in print at TU Wien Bibliothek.

3 Characteristics of full-Heusler materials based on Fe2VAl

Heusler alloys are intermetallic compounds that can be subclassified into half-Heusler and full-Heusler alloys. Their discovery was accomplished by German chemist Friedrich Heusler in 1903 when he detected ferromagnetic behaviour in Cu_2MnAl by stoichiometrically combining the pure elements Cu, Mn and Al which are not ferromagnetic [62]. Heusler alloys are ternary compounds consisting of X,Y,Z-elements, where X and Y are usually transition metals and Z is a p-block element. Half-Heusler compounds have the stoichiometric composition 1:1:1 and full-Heusler materials 2:1:1. They have semiconducting and semimetallic electronic structures and - next to a broad range of other applications - are considered for thermoelectrics due to their high power factor, mechanical strength, low cost and non-toxic properties. Especially half-Heusler materials have drawn a lot of interest in the field because their ZT value is much higher compared to full-Heusler compounds with $ZT > 1$ being achieved in p-type Ti-doped FeNbSb [11]. The maximum ZT values for full-Heusler materials on the other hand vary around $ZT = 0.1 - 0.2$ which is due to their large thermal conductivities. Nonetheless, full-Heusler compounds have been studied as a thermoelectric material for energy harvesting applications for about 20 years with Fe_2VAl-based compounds being the most prominent [22]. In this chapter the characteristics of this compound in terms of crystal structure and electronic structure as well as the effects of doping, off-stoichiometry and anti-site defects will be discussed.

3.1 Crystal structure

Fe_2VAl, like all other full-Heusler compounds, crystallizes in the cubic $L2_1$ structure, which is in the space group $Fm\overline{3}m$ no. 225 with Cu_2MnAl being the archetype. The Fe atoms occupy the Wyckoff position 8c (1/4, 1/4, 1/4), the V atoms sit at 4a (0, 0, 0) and the Al atoms at 4b (1/2, 1/2, 1/2). Figure 3.1 shows the crystal structure of Fe_2VAl, which can be interpreted as four interpenetrating *fcc* sublattices. Two of those sublattices are formed by the Fe atoms and the other two by the V and Al atoms. The latter form a NaCl-type structure as can be seen in Figure 3.2, while the Fe atoms sit in tetrahedral holes. Another possible way to understand the full-Heusler crystal structure is by a zinc blende-type structure (ZnS) that is built up

Die approbierte gedruckte Originalversion dieser Diplomarbeit ist an der TU Wien Bibliothek verfügbar.
The approved original version of this thesis is available in print at TU Wien Bibliothek.
TU WIEN Bibliothek Your knowledge hub

by one Fe and Al while the remaining Fe is occupying the tetrahedal holes and the octahedral holes are filled by V atoms. In this ZnS-type structure the Fe and Al atoms form hybrid t_2 and a_1 orbitals from their s and p states. The hybridization leads to the formation of one set of antibonding states and a set of bonding states as shown in Figure 3.3, whereas only the latter are occupied due to the large difference in energy. Because of the tedrahedal geometry the $d_{x^2-y^2}$, d_{z^2} and d_{xy}, d_{xz}, d_{yz} orbitals of the Fe atoms are split into a pair of twofold degenerate e orbitals of lower energy and threefold degenerate t_{2g} orbitals of higher energy. The d states of the V atom are similarily split and with the Fermi energy positioned as seen in Figure 3.3 this results in a semiconductor-like electronic structure. However, as will be shown in section 3.4, this pseudo energy gap which is formed due to the previously described hybridization and splitting of the orbitals is very small. Therefore, slight changes in the electronic structure or position of E_F due to atomic disorder, off-stoichiometric sample preparation or doping with other elements can lead to drastic changes in the thermoelectric properties.

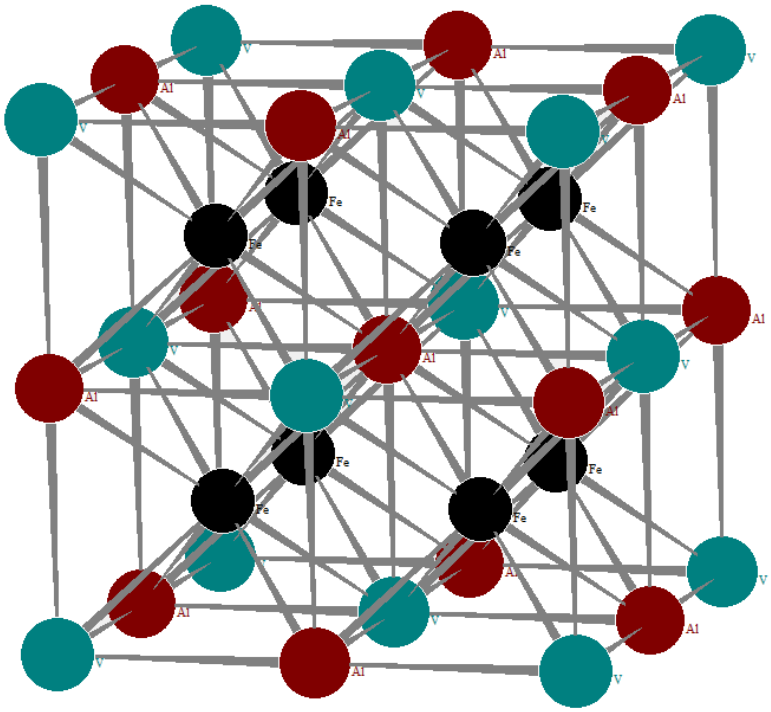

Figure 3.1: Crystal structure of Fe_2VAl. The Fe atoms are portrayed in black, the V atoms blue and the Al atoms red.

Die approbierte gedruckte Originalversion dieser Diplomarbeit ist an der TU Wien Bibliothek verfügbar.
The approved original version of this thesis is available in print at TU Wien Bibliothek.
TU WIEN Bibliothek Your knowledge hub

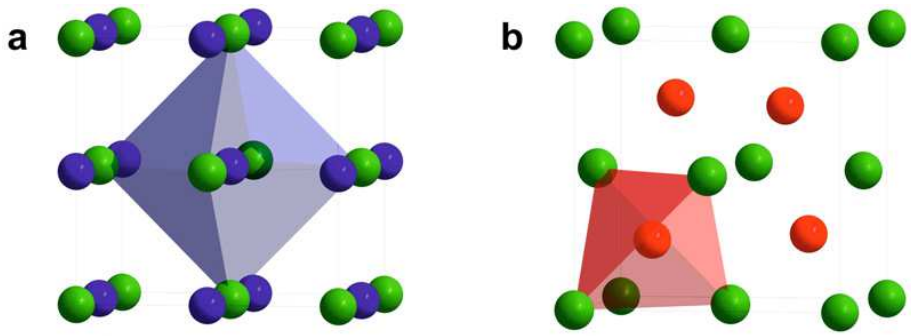

Figure 3.2: a) NaCl-type crystal structure with the blue and green atoms representing vanadium and aluminum respectively. b) Zinc blende-type structure with Fe atoms (in red) sitting in tetrahedral holes and Al atoms in green.

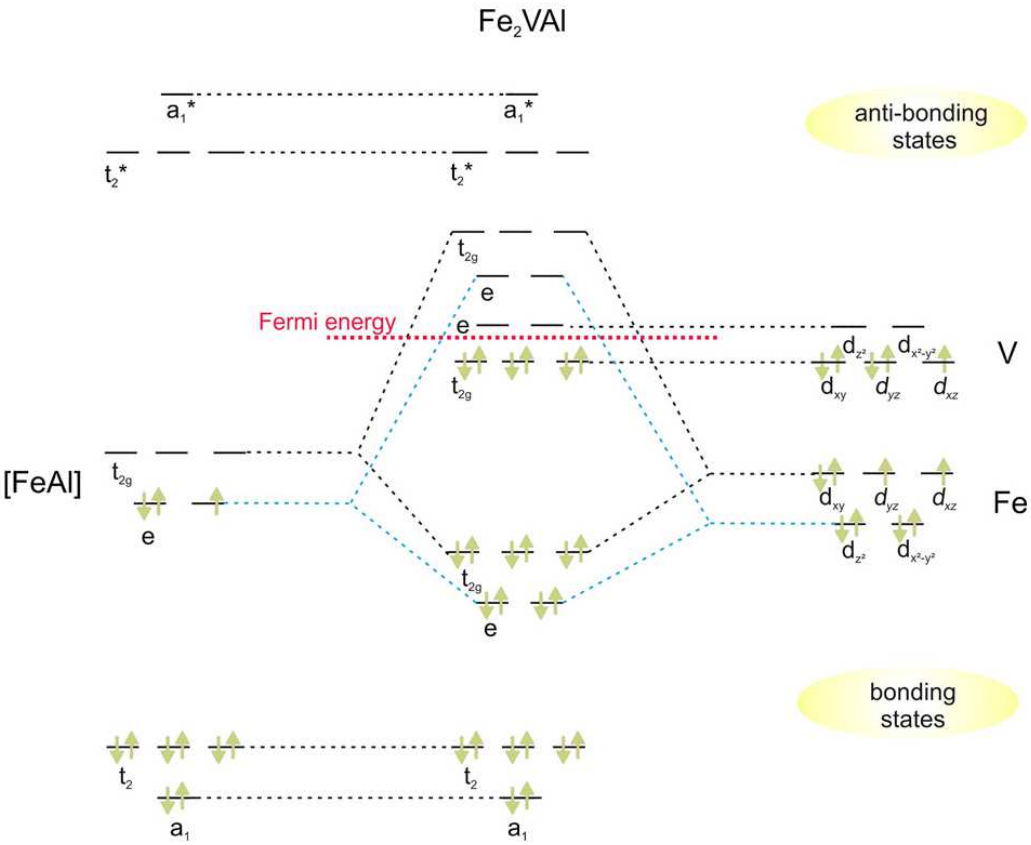

Figure 3.3: Orbital hybridization in Fe_2VAl. Reproduced with permission from [17].

Die approbierte gedruckte Originalversion dieser Diplomarbeit ist an der TU Wien Bibliothek verfügbar.
The approved original version of this thesis is available in print at TU Wien Bibliothek.

3.2 Anti-site disorder

The $L2_1$ structure is a completely ordered crystal structure where every atom has its defined Wyckoff position. Anti-site disordering is the condition that some of the atoms are not occupying their respective lattice sites, hence reducing the symmetry. Because the atomic radii of Fe, V and Al are comparable and due to the nature of chemical bonding in Fe_2VAl, atomic disorder is quite frequent. In the following the most prominent types of atomic disorder for this compound will be introduced (DO_3, B2, A2) as can be seen in Figure 3.4.

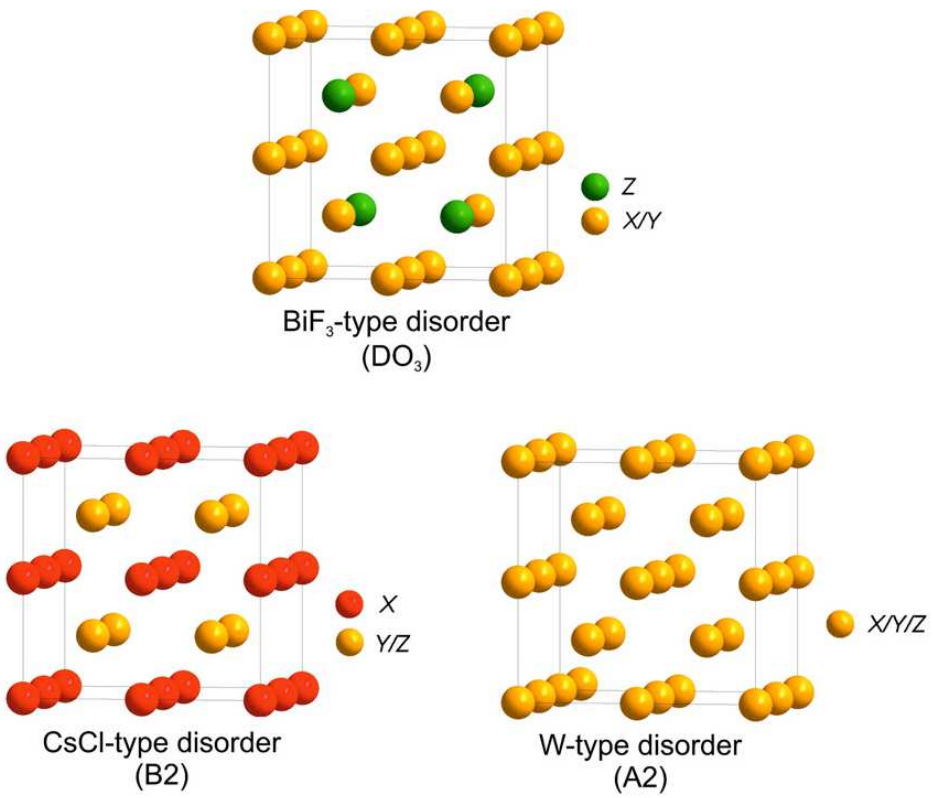

Figure 3.4: Most prominent types of atomic disorder in Fe_2VAl. Reproduced with permission from [17].

BiF_3-type disorder (DO_3)

If the Fe and V atoms on the 8c and 4a sites distribute randomly among eachother a BiF_3-type disorder can be observed. The structre is called DO_3 and is the crystal

Die approbierte gedruckte Originalversion dieser Diplomarbeit ist an der TU Wien Bibliothek verfügbar.
The approved original version of this thesis is available in print at TU Wien Bibliothek.
TU WIEN Bibliothek Your knowledge hub

structure of Fe_3Al. Therefore, in the case of Fe/V-offstoichiometry, this type of disorder is prevalent. The same is true for Fe and Al.

CsCl-type disorder (B2)

In the case of a random and even distribution of V and Al atoms the 4a and 4b Wyckoff positions become equivalent and the B2-structure with the space group $Pm\overline{3}m$ no. 221 is obtained. This CsCl-type disorder is very common, especially in V/Al-offstoichiometric samples. Moreover, it has been shown that the fully ordered $L2_1$ structure undergoes a phase transition into the B2 structure at higher temperatures around 1373 K [33].

W-type disorder (A2)

The fully disordered case is the A2 structure where all Wyckoff positions become equivalent and the lattice becomes *bcc*. Like the B2 structure, this W-type disorder is achieved at higher temperatures until a full phase transition into the A2 structure happens at around 1473 K in the case of Fe_2VAl as a Rietveld analysis of an *in situ* neutron powder diffraction experiment during continuously increasing temperature by Maier et.al. suggests [33].

Figure 3.5 shows the XRD patterns (20-50 deg.) of the previously shown structures.

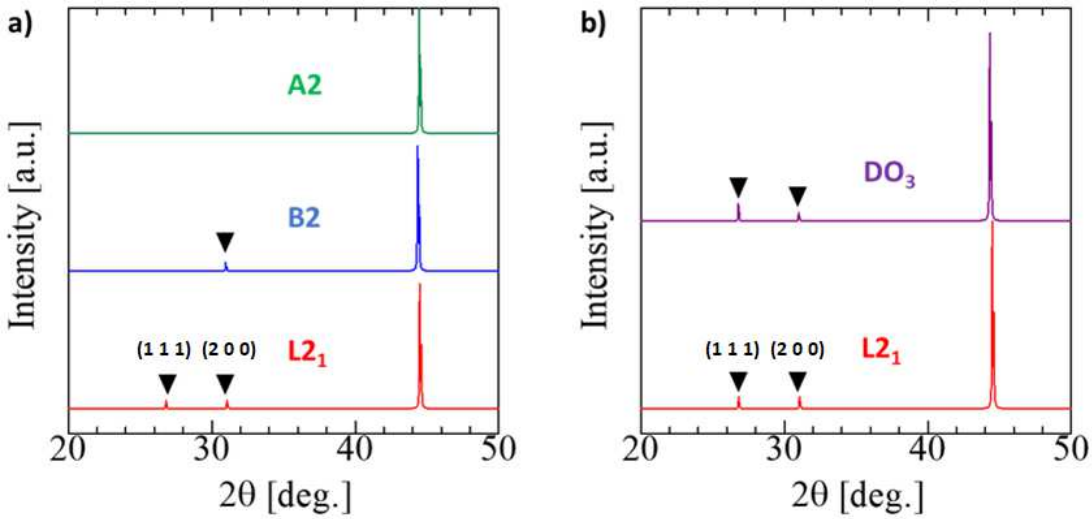

Figure 3.5: XRD patterns comparing the first three visible peaks of the $L2_1$ structure with a) partially disordered B2 and fully disordered A2 structure patterns and b) the BiF_3-type DO_3 pattern.

Die approbierte gedruckte Originalversion dieser Diplomarbeit ist an der TU Wien Bibliothek verfügbar.
The approved original version of this thesis is available in print at TU Wien Bibliothek.
TU Bibliothek Your knowledge hub WIEN

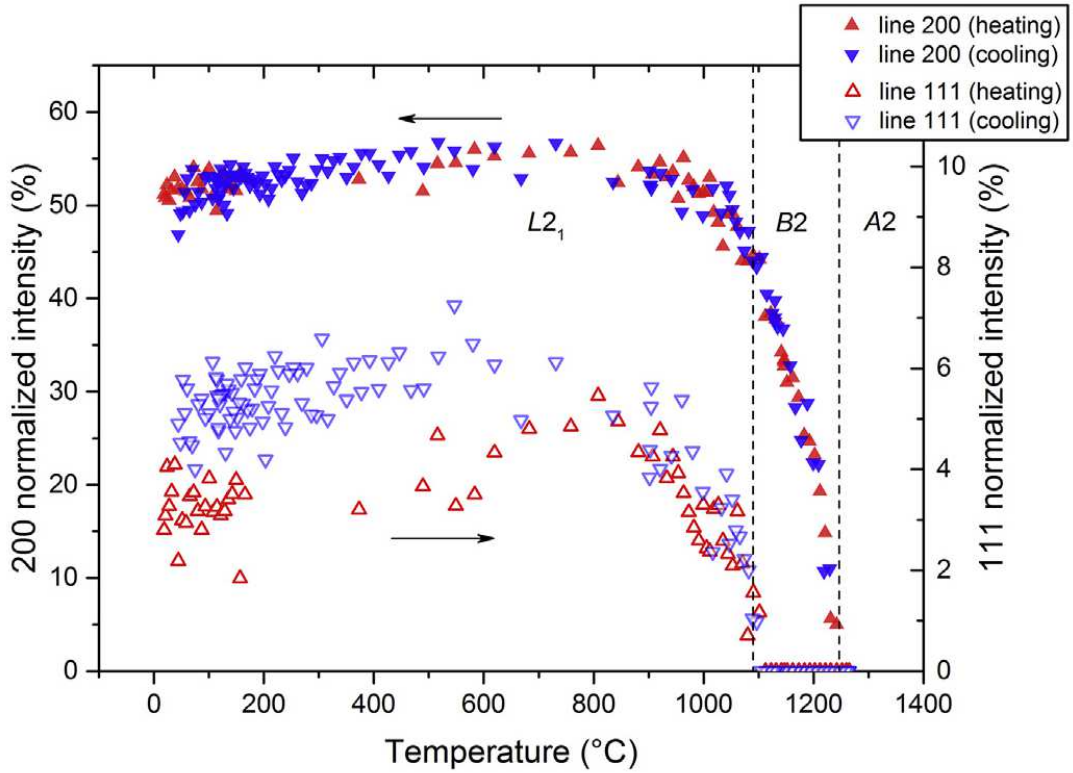

Figure 3.6: Continuous decrease of the (111) and (200) peak intensities in stoichiometric Fe_2VAl with increasing temperature and growing disorder. Upon slow cooling the $L2_1$ order is retrieved. Reproduced with permission from [33].

It has been shown in various papers by DFT calculations that anti-stite disorder has a distinct influence on the electronic structure of full-Heusler compounds and thus on the magnetic and thermoelectric properties [3, 33, 36, 49, 61]. Especially Fe/Al and Fe/V anti-site defects form impurity states near the Fermi energy. For the A2 structure a closure of the pseudogap and transition from the semimetallic to a metallic electronic structure can be expected [33, 61]. Therefore, annealing at immaculate conditions and stoichiometric sample preparation are mandatory for retaining the desired $L2_1$ structure of Fe_2VAl and optimizing the thermoelectric properties. Nonetheless, it has been shown in numerous studies that deliberately introducing off-stoichiometry into the sample's composition can optimize the thermoelectric properties [38, 52, 56]. To summarize, it should be accentuated that a careful determination of the crystal structure by XRD measurements is necessary. Peak intensities that are mismatching the full-Heusler pattern, as in Figure 3.5 and Figure 3.6, are a strong indication for atomic disorder.

Die approbierte gedruckte Originalversion dieser Diplomarbeit ist an der TU Wien Bibliothek verfügbar.
The approved original version of this thesis is available in print at TU Wien Bibliothek.
TU Bibliothek Your knowledge hub WIEN

3.3 Ternary phase diagrams for the (Fe,V,Al)-system

The off-stoichiometric effect has shown to be an effective way to improve the thermoelectric properties in Fe_2VAl-based compounds. Furthermore, different synthesis routes and annealing conditions have shown to yield quite ambiguous values of S and σ. This is due to the very small energy pseudogap in Fe_2VAl. Hence, small changes in terms of anti-site disorder and off-stoichiometry severely affect the electronic DOS near E_F. Moreover, the incorporation of nanostructured secondary phases into the main matrix has proven to be an effective way for reducing the thermal conductivity in other materials and could be a key strategy for reducing the rather high λ in Fe_2VAl full-Heusler compounds. Those reasons alone are a good argument for why detailed knowledge about the thermodynamic properties and a ternary phase diagram for (Fe,V,Al) would be of great interest. Unfortunately, it is very time-consuming to experimentally obtain a complete ternary phase diagram for various temperatures. So far, only specific regions of the ternary phase diagram have been investigated [26]. However, it is possible to use DFT calculations in order to gain an insight into phase equilibria of ternary systems such as (Fe,V,Al). A quick excursion into thermodynamics shows that a phase is in its equilibrium if the Gibbs free energy $\mathcal{G}$ is minimized and $d\mathcal{G} = 0$. The Gibbs free energy is defined as

$$\mathcal{G} = \mathcal{H} - T\mathcal{S}, \tag{3.1}$$

where $\mathcal{H}$ is the enthalpy

$$\mathcal{H} = \mathcal{U} + pV, \tag{3.2}$$

T the temperature, $\mathcal{S}$ the entropy, $\mathcal{U}$ the internal energy, V the volume of the system and p the pressure which is considered constant. Therefore:

$$d\mathcal{H} = d\mathcal{U} + p\,dV. \tag{3.3}$$

In the isothermal case and assuming that $dV = 0$ in solids the total differential of $\mathcal{G}$ which needs to be zero for reaching an equilibrium is:

$$d\mathcal{G} = d\mathcal{U} - Td\mathcal{S}. \tag{3.4}$$

This means that at $T = 0$ K the total differential of the Gibbs free energy $d\mathcal{G}$ can be calculated from the total energy $\mathcal{U}$ which can be acquired from DFT calculations. Furthermore, $\mathcal{G} = \mathcal{H}$ at absolute zero so the enthalpy of formation $\Delta_f\mathcal{H}$ of a ternary phase $Fe_xV_yAl_z$ can be calculated as has been performed in an *ab initio* study by [2]:

Die approbierte gedruckte Originalversion dieser Diplomarbeit ist an der TU Wien Bibliothek verfügbar.
The approved original version of this thesis is available in print at TU Wien Bibliothek.
TU Bibliothek Your knowledge hub WIEN

$$\Delta_f \mathcal{H}^{0K}(\mathrm{Fe}_x\mathrm{V}_y\mathrm{Al}_z) = \mathcal{U}(\mathrm{Fe}_x\mathrm{V}_y\mathrm{Al}_z) - \frac{x\mathcal{U}(Fe) + y\mathcal{U}(V) + z\mathcal{U}(Al)}{x+y+z}. \tag{3.5}$$

By combining experimentally drawn sections of the ternary phase diagrams at 773 K by [15, 26] and results from DFT calculations, Berche and Jund provide suggestions for a complete ternary phase diagram of the (Fe,V,Al) system at 773 K and 400 K (see Figure 3.7) [2]. It can be seen that the single phase domain for the desired $L2_1$ phase is extremely small. Thus, deviations from the Fe_2VAl-stoichiometry will result in multiphase regions.

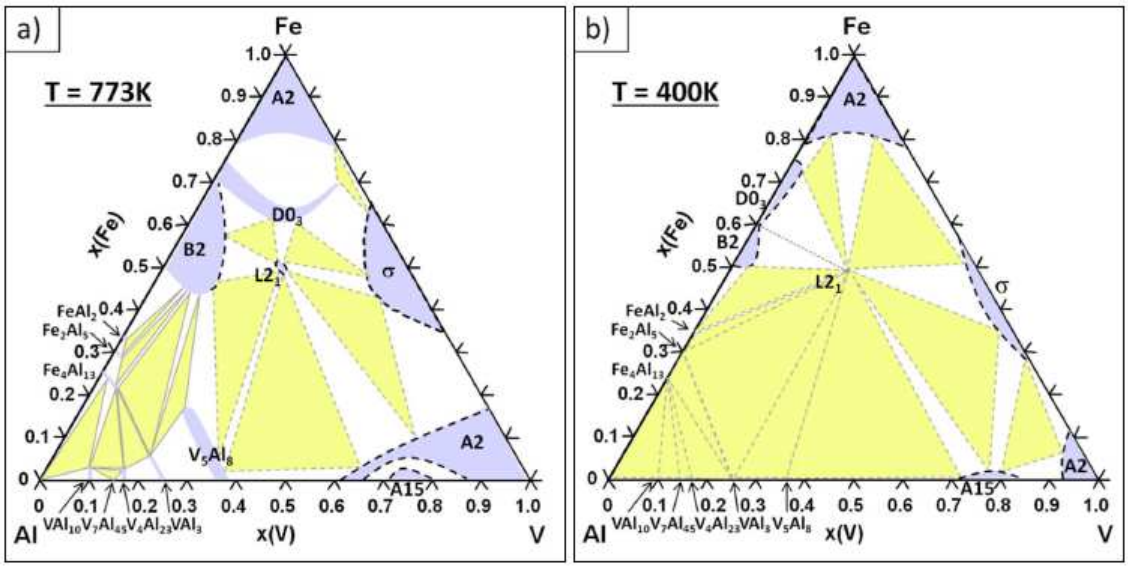

Figure 3.7: Isothermal sections of a complete ternary phase diagram for (Fe,V,Al) at a) 773 K and b) 400 K. Single phase regions are portrayed in blue, two phase regions in white and three face regions in yellow. Reproduced with permission from [2].

Die approbierte gedruckte Originalversion dieser Diplomarbeit ist an der TU Wien Bibliothek verfügbar.
The approved original version of this thesis is available in print at TU Wien Bibliothek.

3.4 Electronic structure

The electronic structure of Fe_2VAl has been studied thoroughly by both first principle calculations [53] and experimental methods such as optical conductivity [43] and photoelectron spectroscopy measurements [55] and a pseudogap of 0.1-0.2 eV was clearly substantiated. The electronic DOS, as can be seen in Figure 3.8, clearly shows steep edges in both directions of the Fermi energy which is necessary for attaining high n- and p-type values of S as has been discussed in chapter 2. The Fermi energy is positioned in the valence band edge which means that the stoichiometric compound Fe_2VAl is in fact p-type with a Seebeck coefficient of $S \approx +30\,\mu V/K$ at room temperature [42]. One has to note that this value for the Seebeck coefficent applies to samples synthesized by arc melting. Other synthesis routes such as mechanical alloying have resulted in quite differing values $S \approx -20$ µV/K [35] which is due to off-stoichiometry or effects of atomic disordering that occur during the synthesis process. Although literature often refers to the semiconductor-like nature of Fe_2VAl, the band gap is in fact of negative sign which means that the conduction band minimum $E_{c,min}$ is below the valence band maximum $E_{v,max}$. The energy of the band gap $E_g = E_{c,min} - E_{v,max} < 0$, which makes this material a classic semimetal. This can be clearly seen when looking at the calculated band structure of Fe_2VAl in Figure 3.9. The band structure was calculated implementing the Wien2k code and GGA for the exchange correlation functional by Y. Iwasaki at the University of Tokyo. Later it will be shown that opening this pseudogap combined with carrier density optimization will lead to higher values of S than can be expected for the rigid band model. A flat band in the ΓX direction is controlled by Fe e states, while the highly dispersive lowest conduction band shows dominant V e character. The highest valence band is controlled by Al and Fe t_{2g} states. Due to the fact, that the flat and heavy bands of Fe e character are dispersive in other directions of the Brillouin zone, Fe_2VAl is able to produce large values of $S^2\sigma$ for n-type carrier doping [4]. However, this band is not contributing to thermoelectric transport at room temperature with the E_F positioned in the valence band edge and one has to substitute elements with higher valence electron concentration in order to increase the carrier density and shift the Fermi energy towards the flat and dispersive conduction band. Several elements have been investigated to fulfill that purpose, which has been achieved with great success as will be shown in the upcoming section.

Die approbierte gedruckte Originalversion dieser Diplomarbeit ist an der TU Wien Bibliothek verfügbar.
The approved original version of this thesis is available in print at TU Wien Bibliothek.
TU Bibliothek Your knowledge hub WIEN

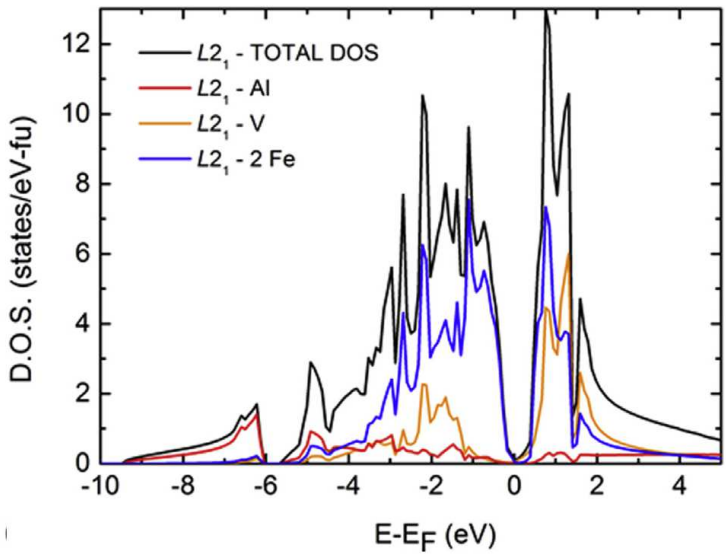

Figure 3.8: Electronic DOS of Fe_2VAl. The Fermi energy is positioned near the valence band edge. Reproduced with permission from [33].

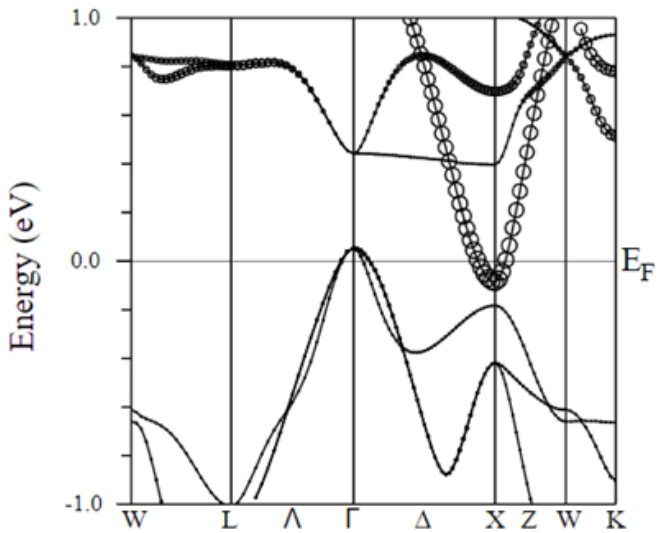

Figure 3.9: Band structure of Fe_2VAl, calculated in Wien2k code with the GGA for the exchange correlation functional. The size of the circles represent the contribution of the vanadium d-states which contribute mainly to the parabolic conduction band with its minimum at the X point of the first Brillouin zone. The Fermi level is positioned near the valence band edge. Reproduced with permission from [19].

Die approbierte gedruckte Originalversion dieser Diplomarbeit ist an der TU Wien Bibliothek verfügbar.
The approved original version of this thesis is available in print at TU Wien Bibliothek.
TU Bibliothek WIEN Your knowledge hub

3.4.1 Rigid band model

In the compound Fe_2VAl it is necessary to shift the Fermi level to its optimum position for improving both the Seebeck coefficient and electrical conductivity. This is achieved by elemental substitution on either Fe-, V-, or Al-site. Regardless of which site the doping elements will usually have a higher or smaller number of valence electrons and in the rigid band model this implies that n-type and p-type materials will be the result respectively, as increasing the number of valence electrons should increase the electron carrier density and decreasing should lead to a boost in hole carriers. Thus, the Fermi energy E_F will be shifted towards the conduction band or towards the valence band. As a matter of fact, this rigid-band-like shift has been observed for various elements by Nishino et.al. at the Nagoya Institute of Technology [42]. They plotted the values of Seebeck coefficients for Fe_2VAl doped with various different elements as a function of valence electron concentration (VEC), where the VEC for an arbitrary ternary compound $A_x\,B_y\,C_z$ is defined as:

$$\mathrm{VEC} = \frac{xa + yb + zc}{x + y + z}, \tag{3.6}$$

where the number of valence electrons for element A is a , b for B and c for C. In that case VEC $= 6$ for Fe_2VAl, as $a = 8$ for Fe, $b = 5$ for V and $c = 3$ for Al. In Figure 3.10 it can be pointed out that the Seebeck coefficients at $T = 300\,K$ drastically increase to positive values for VEC ≤ 6 and negative values for VEC ≥ 6 and furthermore seem to fall onto the same universal curve for specific doping elements which are pointed out in Figure 3.10. This highly suggests a rigid band model, where the effect of doping mainly shifts the Fermi level from a rather in-gap position towards either band edge but does not or only slightly changes the electronic structure around the Fermi energy. However, the rigid band model does only hold true for specific elements, which are listed in Figure 3.10 and a breakdown of the rigid band model was for example found in $Fe_{2-x}Ni_xVAl$ compounds by Knapp et.al., where a narrow impurity band appears near E_F due to the substitution of Ni atoms at the Fe sites [25].

Die approbierte gedruckte Originalversion dieser Diplomarbeit ist an der TU Wien Bibliothek verfügbar.
The approved original version of this thesis is available in print at TU Wien Bibliothek.
TU Bibliothek WIEN Your knowledge hub

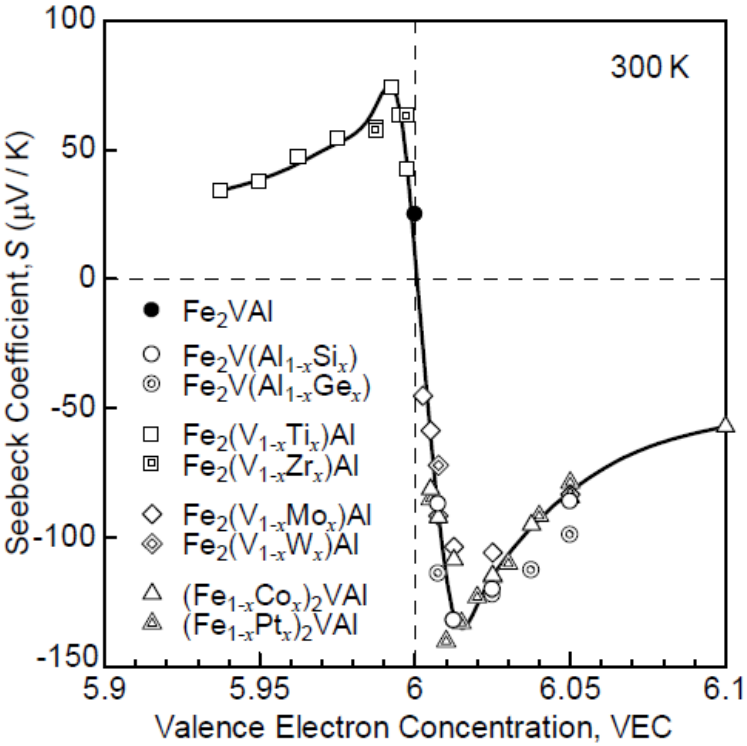

Figure 3.10: Rigid band model: Seebeck coefficients of Fe_2VAl-based compounds, doped with various elements as a function of VEC at 300 K fall on a similar curve. The stoichiometric composition Fe_2VAl has a slightly positive Seebeck coefficient $S \approx 30\,\mu V/K$ at VEC $= 6$. Reproduced with permission from [42].

3.5 Choice of doping elements

3.5.1 Silicon doping effect

For n-type materials there have been a variety of candidates for doping elements such as tungsten for vanadium, cobalt or even platinum for iron. However, the elemental substitution of silicon for aluminum has proven to be one of the most effective and has been diligently researched over the past decade in several studies [21, 31, 60]. The doping effect of Si can be well described in most cases by the rigid band model, although some calculations show a modification of the band structure in terms of the lowering of the maximum valence band at the Γ point in the first Brillouin zone [4]. Figure 3.11 shows the temperature dependence of the Seebeck coefficient and electrical resistivity of $Fe_2VAl_{1-x}Si_x$. The Seebeck coefficient S reaches a maximum for $x = 0.05$ and decreases with higher amounts of Si content as the Fermi level is shifted deeply into the conduction band, hence leading to bipolar transport and a cancellation of charge carriers. The resistivity ρ on the

Die approbierte gedruckte Originalversion dieser Diplomarbeit ist an der TU Wien Bibliothek verfügbar.
The approved original version of this thesis is available in print at TU Wien Bibliothek.
TU Bibliothek WIEN Your knowledge hub

other hand decreases gradually with the amount of Si doping. Then, more charge carriers become available for transport as mentioned in section 2.6. Moreover, a semiconductor-like behaviour for ρ is observed in Fe_2VAl and promptly disappears for $x > 0$. As a matter of fact the low temperature resistivity decreases to such an extent that ρ is almost two orders of magnitude lower for $Fe_2VAl_{0.8}Si_{0.2}$ than in the undoped sample. It should be remarked that the maximum power factor achieved by substituting Si is around 5.5×10^{-3} W/mK^2 in $Fe_2VAl_{0.9}Si_{0.1}$ which is among the highest for any material classes in the thermoelectrics field [21]. Unfortunately, the thermal conductivity which is equally important as the power factor for procuring high values of ZT is about one order of magnitude higher compared to state-of-the-art thermoelectric materials. This is a consequence of the rather simple cubic crystal structure which allows for undisturbed phonon transport and leads to a very high λ_{lattice}. For that compelling reason the main focus has been to reduce the high thermal conductivity by controlling the microstructure or by heavy element substitution. The latter was reliably and successfully accomplished by doping Ta for V. While the effect of reducing λ_{lattice} by Ta substitutions has been thoroughly investigated, the effect of Ta on the electronic structure and the power factor is only fractionally and inconsistently reported [1, 37]. In the following, the Ta doping effect on the electronic structure will be elucidated and a slight enhancement of the thermoelectric properties will be manifested.

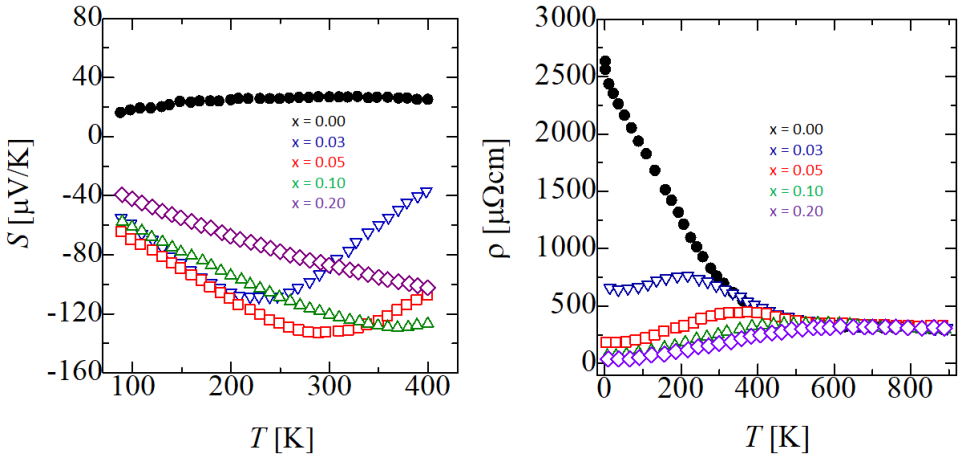

Figure 3.11: Temperature dependence of the Seebeck coefficient and electrical resistivity of $Fe_2VAl_{1-x}Si_x$ [42].

3.5.2 Tantalum doping effect

The effect of heavy element substitution of Ta for V in order to reduce λ_{lattice} has been extensively studied [34, 50, 58, 59]. However, the focus in this work is the

Die approbierte gedruckte Originalversion dieser Diplomarbeit ist an der TU Wien Bibliothek verfügbar.
The approved original version of this thesis is available in print at TU Wien Bibliothek.
TU Bibliothek Your knowledge hub WIEN

improvement of the power factor and effect of Ta doping on the electronic structure. Although the effect of Ta on the electronic structure of Fe_2VAl-based full Heusler compounds has been partly studied in [1, 37] through synchrotron radiation PES and DFT calculations, it is to some extent contradictory and there is no experimental study with respect to the consequences on the thermoelectric properties. We started by plotting the values of samples containing Ta from literature, such as $Fe_2V_{1-x-y}Ta_xTi_y$ (with $x = 0.05, 0.1$) [39, 59] and $Fe_2V_{0.95}Ta_{0.05}Al_{0.95}Si_{0.05}$ [59] against values that follow the rigid-band model [42] as a function of VEC (see Figure 3.12). One can see that the samples containing Ta have indeed higher values of S and therefore a non-rigid shift of the Fermi energy can be assumed. Band structure calculations of the full substitution of Ta for V show the band structure for the hypothetical composition Fe_2TaAl in Figure 3.13. One can see that in comparison to Fe_2VAl the band gap widens due to the shift of the lowest conduction band to higher energies. The opening of the band gap and convergence of bands at the X point of the first Brillouin zone already suggests an increase of the effective valley degeneracy and improvement of the thermoelectric properties. Like brought up before, an improvement of the Seebeck coefficients can indeed be satisfactorily shown by experimental studies. It can be summarized that successfully embedding Ta in the $L2_1$ full-Heusler structure can improve the electronic structure and thermoelectric properties of the stoichiometric Fe_2VAl-based compounds in addition to the well-known reduction of the lattice thermal conductivity.

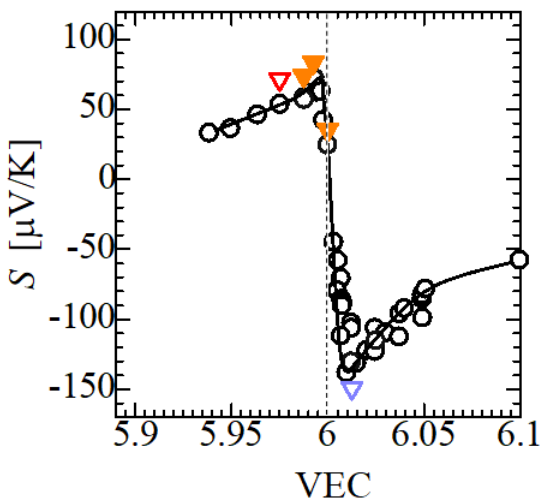

Figure 3.12: Seebeck coefficient against VEC for various Fe_2VAl-based compounds in the rigid band model [42] (black circles) , Ta-doped samples $Fe_2V_{1-x-y}Ta_xTi_y$ with $x = 0.05, 0.1$ [39, 59] (red and orange triangles) and $Fe_2V_{0.95}Ta_{0.05}Al_{0.95}Si_{0.05}$ [59] (blue triangle) following a non-rigid behaviour.

Die approbierte gedruckte Originalversion dieser Diplomarbeit ist an der TU Wien Bibliothek verfügbar.
The approved original version of this thesis is available in print at TU Wien Bibliothek.
TU Bibliothek WIEN Your knowledge hub

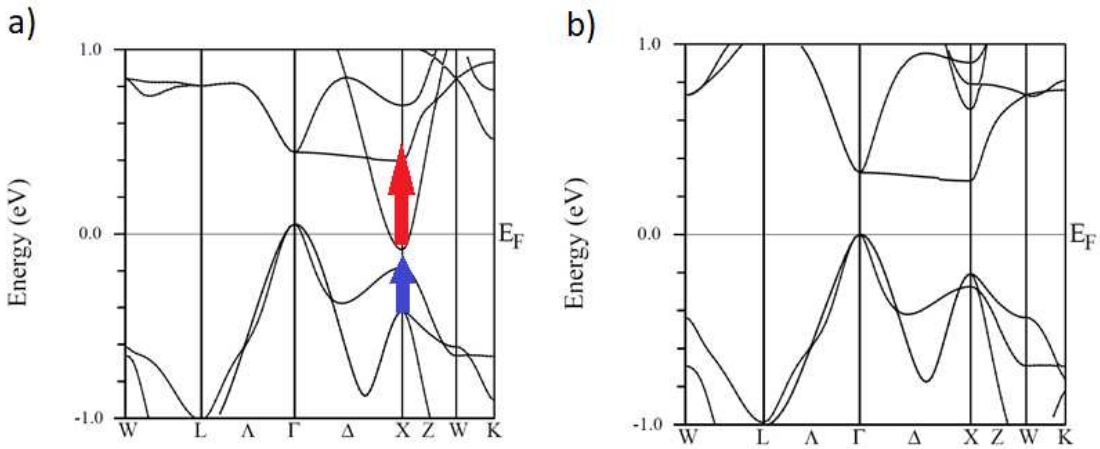

Figure 3.13: Band structure of Fe_2VAl (left panel) and Fe_2TaAl (right panel) calculated in the Wien2k package implementing GGA. The substitution of Ta, due to its higher orbital energies, leads to a shift of the lowest conduction band to higher energies resulting in an opening of the band gap. The convergence of the highly dispersive band at the X point of the first Brillouin zone towards the flat and dispersive band is expected to increase the effective valley degeneracy. Reproduced with permission from [19].

Die approbierte gedruckte Originalversion dieser Diplomarbeit ist an der TU Wien Bibliothek verfügbar.
The approved original version of this thesis is available in print at TU Wien Bibliothek.
TU Bibliothek Your knowledge hub WIEN

Die approbierte gedruckte Originalversion dieser Diplomarbeit ist an der TU Wien Bibliothek verfügbar.
The approved original version of this thesis is available in print at TU Wien Bibliothek.

4 Experimental Methods

4.1 Synthesis

This chapter gives a brief overview of the synthesis, annealing conditions and experimental methods, which were used for analyzing the thermoelectric materials based on $Fe_2V_{1-x}Ta_xAl_{1-y}Si_y$. In order to investigate the microstructure and thermoelectric properties and to find the solubility limit in the case of co-doping Ta and Si a variety of samples were synthesized (see Figure 4.1). The synthesis process included stoichiometric weighing of ≥0.9995 pure bulk elements followed by induction melting. The ingots of around 5 g were then cut into rectangular shape by using a high-speed cutter.

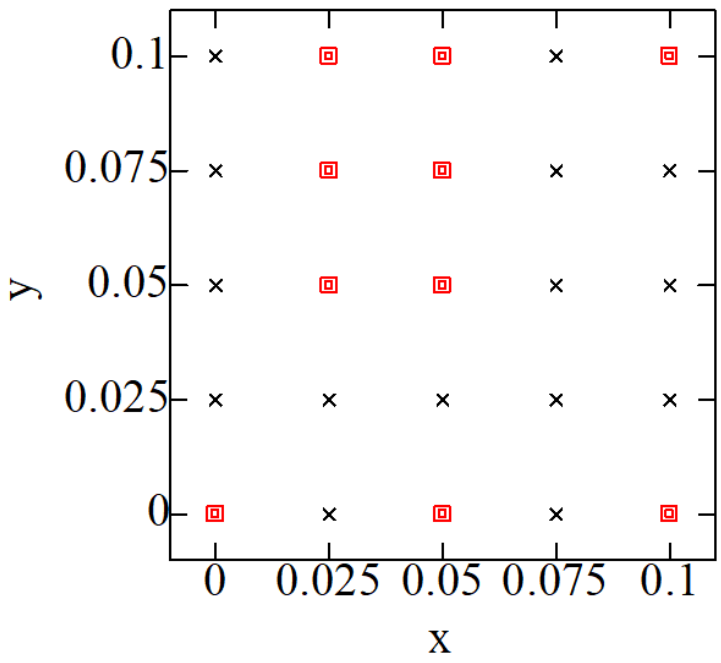

Figure 4.1: Schematic visualisation of the compositions $Fe_2V_{1-x}Ta_xAl_{1-y}Si_y$ aimed to be synthesized in this work (red squares). Grid points of the compositions $x, y \in [0, 0.1]$, which were not synthesized in this work are marked by black crosses.

Die approbierte gedruckte Originalversion dieser Diplomarbeit ist an der TU Wien Bibliothek verfügbar.
The approved original version of this thesis is available in print at TU Wien Bibliothek.
TU Bibliothek Your knowledge hub WIEN

4.1.1 Induction melting

By making practical use of Faraday's law of induction

$$\nabla \times \mathbf{E} = -\frac{\partial \mathbf{B}}{\partial t} \tag{4.1}$$

one is able to homogeneously melt pure metals into alloys and intermetallic compounds such as Fe_2VAl. Contrary to arc melting, bigger and heavier samples can be synthesized and the homogeneity and density of the final material is of high standard. Figure 4.2 shows the set-up during the melting process. Up to four samples can be placed inside a copper trench, which is sealed in a quartz tube under argon atmosphere. One sample at a time can be manually positioned inside a copper coil which is run through by a high frequency current. A water pump assures cooling whilst the materials are being heated by induction and Joule heating.

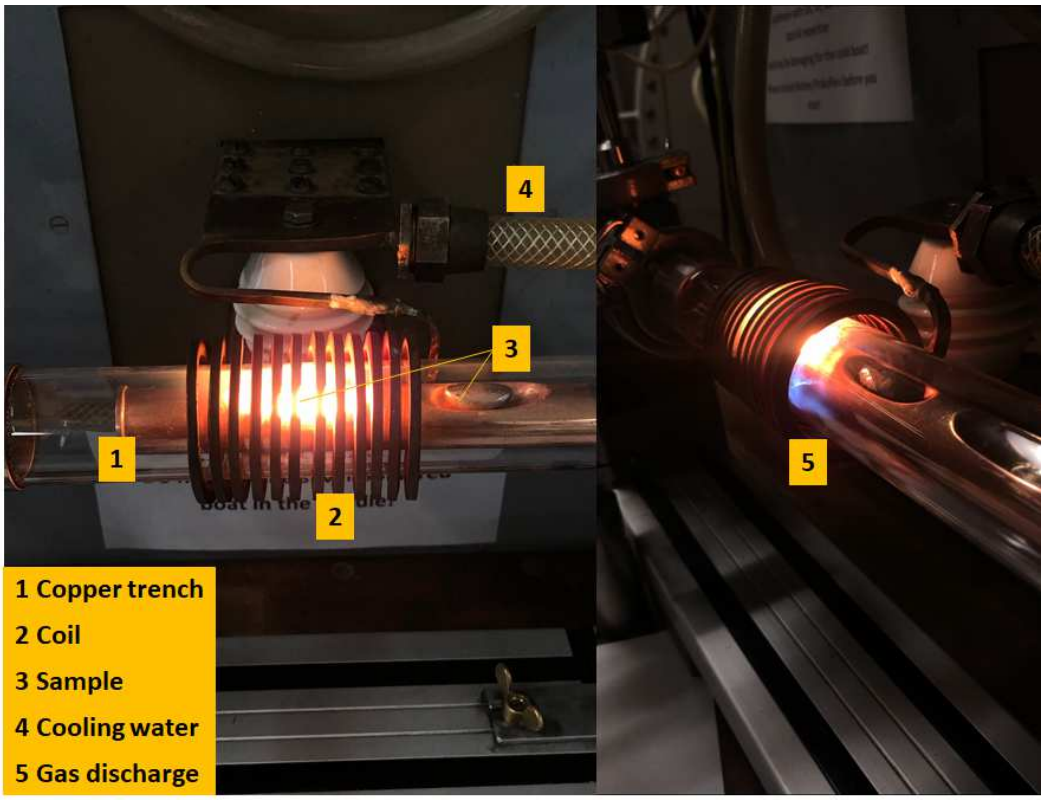

Figure 4.2: Material synthesis set-up for induction melting under argon atmosphere.

Die approbierte gedruckte Originalversion dieser Diplomarbeit ist an der TU Wien Bibliothek verfügbar.
The approved original version of this thesis is available in print at TU Wien Bibliothek.
TU Bibliothek Your knowledge hub WIEN

4.2 Annealing conditions

For the purpose of retaining a high amount of the desired $L2_1$ phase and to investigate the microstructure and phase stability, several different annealing programs have been carried out, varying annealing temperatures and durations. The samples were therefore cut, wrapped in Ta foil for protection, evacuated and sealed in a quartz tube under argon atmosphere before being placed inside the annealing furnace. $Fe_2V_{1-x}Ta_xAl_{1-y}Si_y$ with $x = 0.05, 0.1$; $y = 0.1$ were annealed as can be seen in Figure 4.3. The samples with $x = 0.05, 0.1$; $y = 0$ were annealed at 1073 K for seven days. The remaining specimen with compositions according to Figure 4.1 were cut into two pieces of equal size, that were annealed at 1073 K and 1273 K for seven days respectively in order to compare the effect of annealing temperature for equal annealing durations.

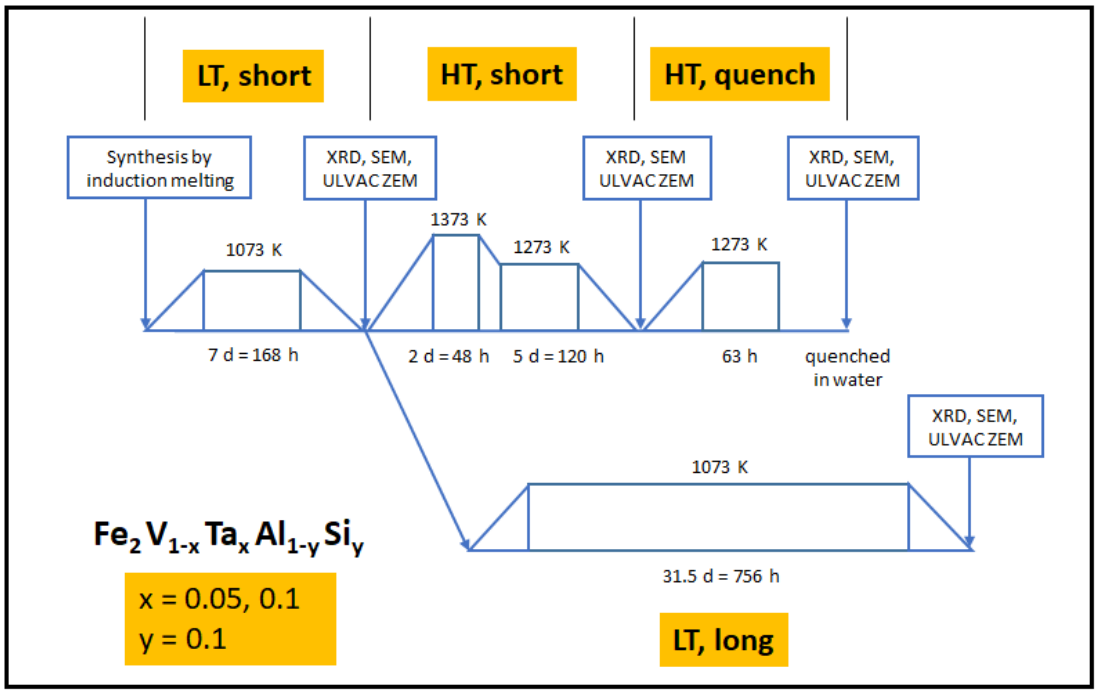

Figure 4.3: Annealing conditions for $Fe_2V_{1-x}Ta_xAl_{1-y}Si_y$ with $x = 0.05, 0.1$; $y = 0.1$. Two high temperature (HT) and two low temperature (LT) programs have been performed as depicted in the diagram. The (HT,quenched)- and (LT,long)-conditions were only applied to the sample with $x = 0.05$. The annealing and measurements were executed at The University of Tokyo, GSFS, Department of Advanced Materials Science.

Die approbierte gedruckte Originalversion dieser Diplomarbeit ist an der TU Wien Bibliothek verfügbar.
The approved original version of this thesis is available in print at TU Wien Bibliothek.
TU Bibliothek Your knowledge hub WIEN

4.3 XRD measurement set-up

Since most physical properties of a solid material are defined by its composition and crystal structure, the phase identification and analysis of crystal structure are essential for making a statement and prediction of its thermoelectric properties. The crystal structure of the samples in this work has been probed by conventional X-ray diffractometry (XRD) by making use of Bragg's law

$$n\lambda = 2d\sin\theta, \quad n \in \mathbb{N}, \tag{4.2}$$

where λ is the wave length of the incident X-rays, d and θ are lattice plane distance and angle as depicted in Figure 4.4.

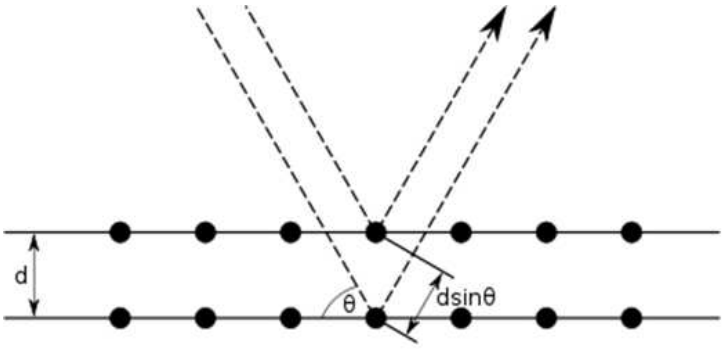

Figure 4.4: Illustration of Bragg's law. The black circles symbolize atoms in the lattice planes. Two different X-ray wave fronts with the same wave legnth are scattered at the upper and lower lattice planes. Constructive interference occurs in accordance with Bragg's law. Image taken from [63].

The measurement is conducted in a Bragg-Brentano (θ, θ)-geometry employing a "Rigaku SmartLab" and the "XPert Pro MPD" by PANalytical. The sample is fixed in a horizontal level and the X-ray source and detector are positioned opposite to each other in an angle θ from the surface of the sample. Usually, the material is ground to a fine powder by hand and put on a sample holder before the measurement. For identifying impurity phases and other crystal structures Rietveld simulations were performed using VESTA (Visualization for electronic and structure analysis), PowderCell and the inorganic crystal structure database ICSD, FIZ Karlsruhe.

4.4 Observation of microstructure by SEM

Sometimes however, if the crystal structure analysis by XRD is insufficient or if one is interested in the spatial distribution, topography or composition of impurity

Die approbierte gedruckte Originalversion dieser Diplomarbeit ist an der TU Wien Bibliothek verfügbar.
The approved original version of this thesis is available in print at TU Wien Bibliothek.
TU Bibliothek Your knowledge hub WIEN

phases, the microstructure needs to be observed. In this study the microstructure was observed by scanning electron microscopy (SEM). For that reason the specimen were satisfactorily polished in order to obtain a smooth surface. An electron beam screens the sample's surface, which is placed in a vacuum chamber inside the microscope. The images can be either chosen from back-scattered electrons which arise from almost elastic scattering processes and have a much higher escape depth or from secondary electrons which are a consequence of inelastic scattering near the surface and therefore give more detailed information about the topography of the sample. In the case of a back-scattered electron image (BEI) which will give a higher contrast and resolution of the composition of the sample, heavier elements inside the sample will give a higher count and therefore a brighter contrast. SEM images for this work were taken with a "JSM-IT100" by JEOL at the Department of Advanced Materials Science, The University of Tokyo and with a "Quanta 250 FEG" at USTEM, TU Wien. Different magnifications were chosen appropriately in order to see the spatial distribution of impurity phases and the evolution of the microstructure. The composition was investigated by energy dispersive X-ray analysis (EDX).

4.5 Measurement of Seebeck coefficient and electrical resistivity

After being cut into rectangular shape and after the crystal structure analysis, the Seebeck coefficient and electrical resistivity for temperatures above room temperature up to 800 K were measured with both the ULVAC ZEM1 and ZEM3. The Seebeck coefficient is evaluated from

$$S = -\frac{\Delta V}{\Delta T}. \tag{4.3}$$

The set-up for the measurement is shown in Figure 4.5 where one side of the sample is heated in opposite to the other and a stable temperature gradient is maintained. A thermocouple is inserted from the side for measuring the voltage while a temperature sensor is measuring the operating temperature. The chamber is evacuated and flushed with an inert gas like helium or argon. The electrical resistivity is measured with the four-terminal sensing method. At high temperatures (300 K up to 800 K) the measurement is performed together with the Seebeck coefficient whereas the low temperature resistivity is measured in a liquid helium cooled bath cryostate from almost 4 K up to room temperature.

Die approbierte gedruckte Originalversion dieser Diplomarbeit ist an der TU Wien Bibliothek verfügbar.
The approved original version of this thesis is available in print at TU Wien Bibliothek.
TU Bibliothek Your knowledge hub WIEN

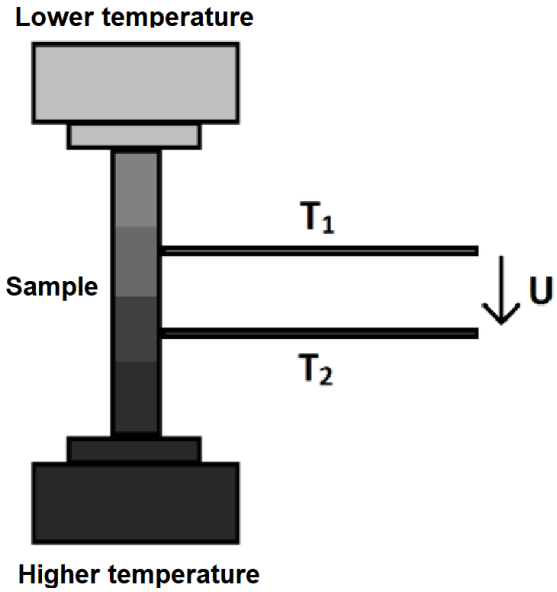

Figure 4.5: Illustration of a Seebeck measurement. A stable temperature gradient is required in the sample and two thermocouples are measuring a voltage U from the side.

Die approbierte gedruckte Originalversion dieser Diplomarbeit ist an der TU Wien Bibliothek verfügbar.
The approved original version of this thesis is available in print at TU Wien Bibliothek.
TU Bibliothek Your knowledge hub WIEN

5 Results

This chapter provides a summary of the most important results encompassing XRD patterns, SEM images and plots of the temperature dependence of ρ and S for various compositions. The aim of this study is to show the solubility of Ta and Si into the $L2_1$ structure and the distribution of the observed impurity phase once the solubility is reached. This leads to a variety of very interesting microstructures. The second half of this chapter focuses on the effect of Ta- and Si-doping on the transport properties S and ρ and tries to establish a relation between the microstructure and thermoelectric properties. Ultimately, the power factor is calculated and maximum values are compared with literature.

5.1 XRD patterns

In any given material the crystal structure directly determines most of its properties, including the phononic and electronic structure. Since the Seebeck coefficient, electrical resistivity and thermal conductivity are all mostly governed by phonon and electron dispersion relations and their scattering times τ_{ph}, τ_{el}, they are therefore inherently tied to the crystal structure. It is safe to say that XRD is the most fundamental and crucial analysis for evaluating a thermoelectric material as it gives an insight into intrinsic quantities such as lattice parameter and disorder in the sample and allows one to detect impurity phases. It should be stressed that performing a XRD measurement is also the first mandatory step after melting and annealing the sample in order to investigate upon whether the process of synthesis of the desired single phase material was succesful or not. Assuming one refrains from any structural analysis of the sample or one or more impurity phases are present, it is then impossible to make any correct statement about the thermoelectric properties of the single phase material.
The XRD patterns for a large number of samples with the stoichiometric composition $Fe_2V_{1-x}Ta_xAl_{1-y}Si_y$ were evaluated in order to find out the solubility limit of Ta and Si into the full-Heusler structure. Some of the samples were annealed under a variety of different conditions with respect to annealing time and temperature. For an annealing duration of one week at a temperature of 1073 K all of the samples with the exception of $Fe_2V_{0.9}Ta_{0.1}Al_{0.9}Si_{0.1}$ showed that they retained the desired $L2_1$ structure of Fe_2VAl, as can be seen in Figure 5.1. For the exceptional case of $x = 0.1$ and $y = 0.1$ however, two impurity peaks at around 37 and 41

Die approbierte gedruckte Originalversion dieser Diplomarbeit ist an der TU Wien Bibliothek verfügbar.
The approved original version of this thesis is available in print at TU Wien Bibliothek.
TU WIEN Bibliothek Your knowledge hub

degrees were noticeable. They could be attributed to the hexagonal C14 structure of Fe_2Ta, which belongs to the class of so-called Laves phases. The same impurity peaks could be faintly observed in $Fe_2V_{0.95}Ta_{0.05}Al_{0.9}Si_{0.1}$ upon changing the annealing conditions which were mentioned in chapter 4. This is shown in Figure 5.2, together with a magnification of the region in the diffractogram, in which the peaks of the secondary phase appear. The XRD analysis already indicates that a small amount of secondary phase appears when increasing either x and y or the annealing duration.

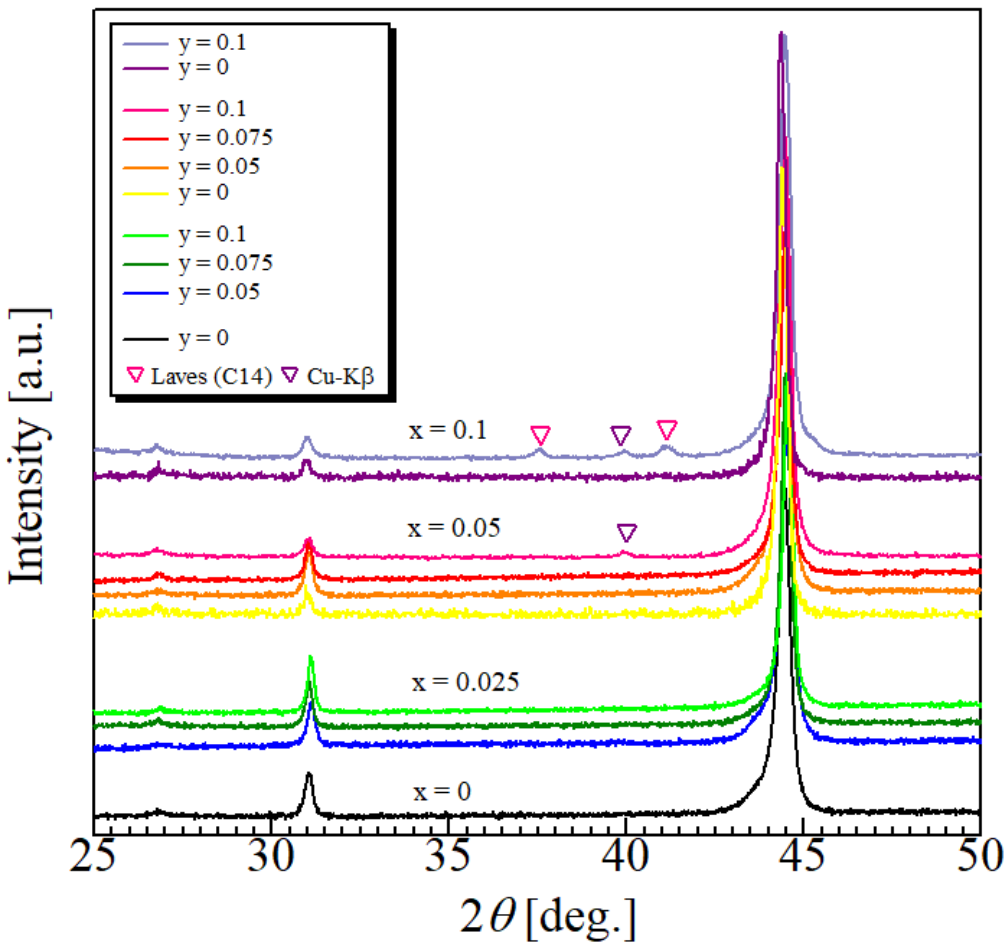

Figure 5.1: XRD patterns of $Fe_2V_{1-x}Ta_xAl_{1-y}Si_y$, annealed at 1073 K for one week. Only the sample with $x = 0.1$ and $y = 0.1$ shows two small impurity peaks at around 37 and 41 degrees.

Die approbierte gedruckte Originalversion dieser Diplomarbeit ist an der TU Wien Bibliothek verfügbar.
The approved original version of this thesis is available in print at TU Wien Bibliothek.
TU Bibliothek Your knowledge hub WIEN

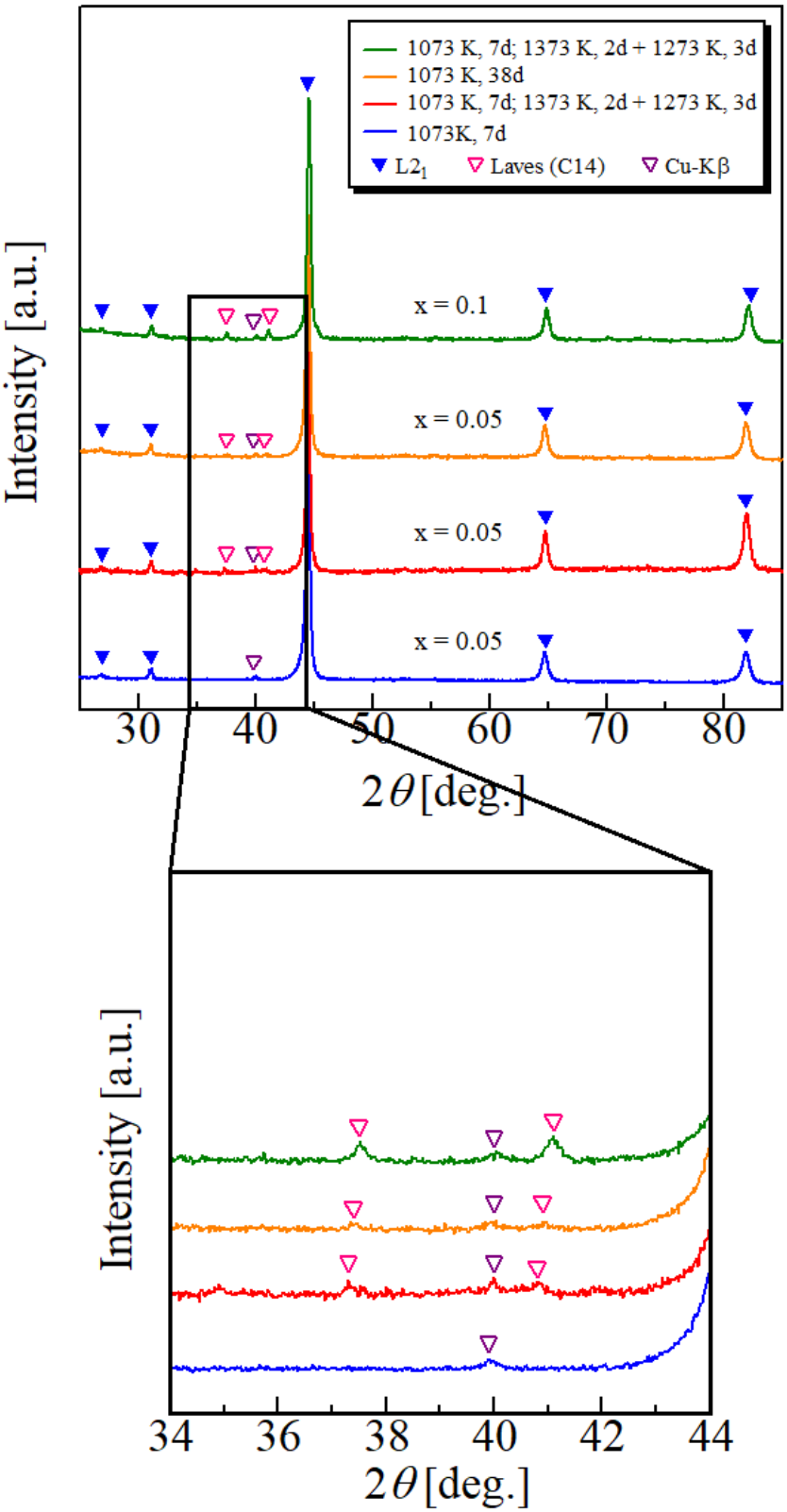

Figure 5.2: XRD patterns of $Fe_2V_{1-x}Ta_xAl_{0.9}Si_{0.1}$ under various annealing conditions.

Die approbierte gedruckte Originalversion dieser Diplomarbeit ist an der TU Wien Bibliothek verfügbar.
The approved original version of this thesis is available in print at TU Wien Bibliothek.
TU Bibliothek Your knowledge hub WIEN

5.1.1 Lattice parameter

One of the quantities of interest regarding the crystal structure is the lattice parameter as it exposes significant characteristics such as anti-site disorder, solubility of dopants and other features, which are ultimately determining transport properties such as electrical and thermal conductivity. For instance, one of the main attempts to reduce the lattice thermal conductivity in Fe_2VAl-based compounds so far has been the elemental substitution with heavy elements, which have a larger atomic radius and are compromising phonon transport by distorting the rather primitive cubic crystal structure. One of those elements is Ta, which fulfills that role by replacing V atoms in the lattice, hence leading to a larger lattice parameter due to its larger atomic radius. The substitution of Si atoms for Al atoms on the other hand, leads to a decrease of the lattice parameter, as can be seen in Figure 5.3. Therefore, the lattice parameter varies with different concentration of x and y and typically increases from the value of the stoichiometric composition as x becomes larger or decreases when y becomes larger. This tendency can indeed be observed in Figure 5.3. However, due to the previously established solubility limit of Ta and Si, the lattice parameter does not linearly change for all samples. Therefore, $Fe_2V_{0.95}Ta_{0.05}Al_{0.9}Si_{0.1}$ and $Fe_2V_{0.9}Ta_{0.1}Al_{0.9}Si_{0.1}$ for instance, exhibit almost the same value.

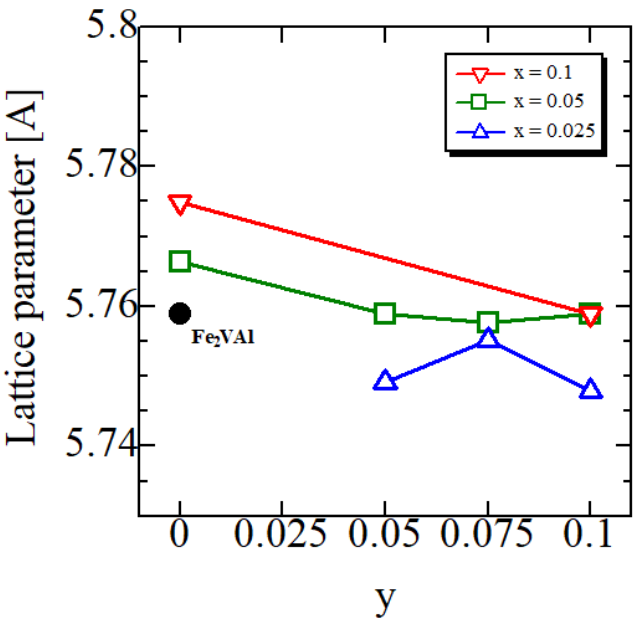

Figure 5.3: Lattice parameter of $Fe_2V_{1-x}Ta_xAl_{1-y}Si_y$ as a function of y for various values of x after annealing at 1073 K for one week.

Die approbierte gedruckte Originalversion dieser Diplomarbeit ist an der TU Wien Bibliothek verfügbar.
The approved original version of this thesis is available in print at TU Wien Bibliothek.
TU Bibliothek WIEN Your knowledge hub

5.2 Microstructure

It has been shown that in most materials the thermoelectric properties heavily depend on the microstructure and therefore the value of ZT can often be improved by optimzing microstructural properties such as grain size, distribution and shape of secondary phases, vacancies, composites and others [5, 28, 44, 54]. In order to investigate the microstructure of Fe_2VAl-based compounds that have been co-doped with Ta and Si and to further manifest the solubility limit and single phase region, samples with eight different compositions corresponding to $Fe_2V_{1-x}Ta_xAl_{1-y}Si_y$ where $x = 0.025, 0.05$, $y = 0.05, 0.075, 0.1$ and $x = 0.1$, $y = 0, 0.1$ which were all annealed at 1073 K for one week have been examined by SEM. Moreover, the microstructural evolution upon changing the annealing conditions was studied for $Fe_2V_{0.95}Ta_{0.05}Al_{0.9}Si_{0.1}$ which showed the most promising performance with respect to the thermoelectric properties. The aim has been to understand the modifications in the microstructure with annealing and composition, in order to potentially establish a relationship with the thermoelectric properties, specifically S and ρ in section 5.3 and section 5.4.

5.2.1 Single phase region and solubility limit

For an annealing duration of one week at 1073 K, the SEM results showed that five out of the eight samples were single phase. As can be seen in Figure 5.4, the increase of either x or y leads to the appearance of an impurity phase, which by EDX was found to be Ta- and Si-rich. The crystal structure of the impurity phase is most likely a hexagonal Fe_2Ta-type C14 structure as suggested by Rietveld simulations of the XRD patterns in section 5.1. This structure belongs to a prevalent class of so-called Laves phases, which are intermetallic compounds that are known for their high electrical conductivity and strong metallic behaviour. The sample with the composition $Fe_2V_{0.95}Ta_{0.05}Al_{0.9}Si_{0.1}$ showed diffuse contrasts in the image that indicate an oversaturated Heusler phase, which is not in the thermal equilibrium. Those diffuse contrasts could also be faintly observed in $Fe_2V_{0.9}Ta_{0.1}Al$, as can be seen in Figure 5.5. Images at higher magnifications of the sample's surface indicate nanoscale precipitation of impurity phase within the supersaturated Heusler region which is shown in Figure 5.6. We believe that those samples are therefore at the borderline of the single phase region. High contrast images of those borderline samples are given in Figure 5.7. They show secondary phase precipitates, whose grain size starts from a few hundred nanometers until they connect and grow. Grain boundary segregation and a formation of Laves-rich grain boundaries within the oversaturated diffuse regions are expected.

Die approbierte gedruckte Originalversion dieser Diplomarbeit ist an der TU Wien Bibliothek verfügbar.
The approved original version of this thesis is available in print at TU Wien Bibliothek.
TU Bibliothek WIEN Your knowledge hub

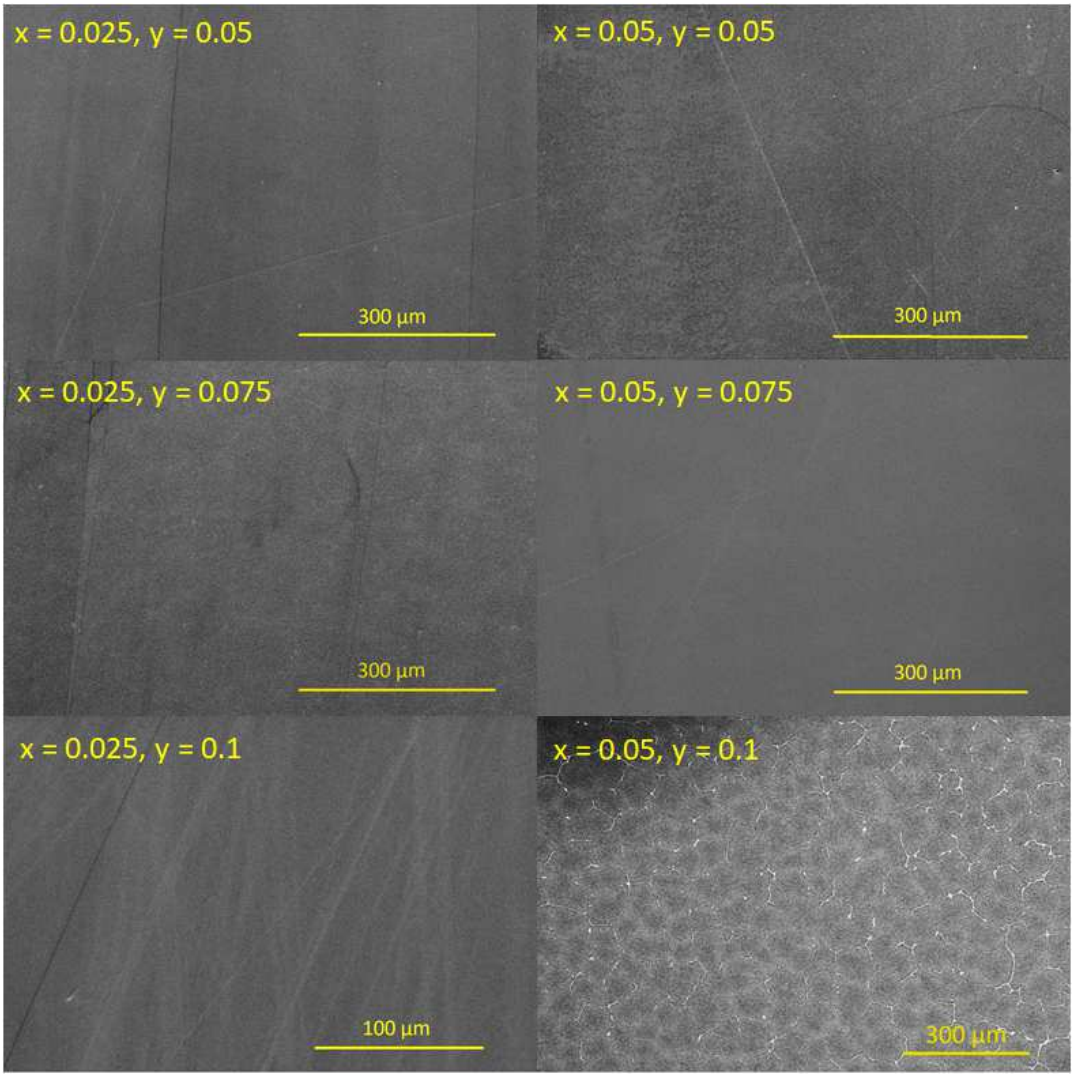

Figure 5.4: SEM images of $Fe_2V_{1-x}Ta_xAl_{1-y}Si_y$, annealed at 1073 K for one week. When changing the composition towards increasing either x or y a secondary impurity phase appears (bright white region in the lower right panel). Diffuse contrasts in $Fe_2V_{0.95}Ta_{0.05}Al_{0.9}Si_{0.1}$ indicate a supersaturated Ta-rich Heusler phase that is in a non-equilibrium state.

Die approbierte gedruckte Originalversion dieser Diplomarbeit ist an der TU Wien Bibliothek verfügbar.
The approved original version of this thesis is available in print at TU Wien Bibliothek.
TU Bibliothek WIEN Your knowledge hub

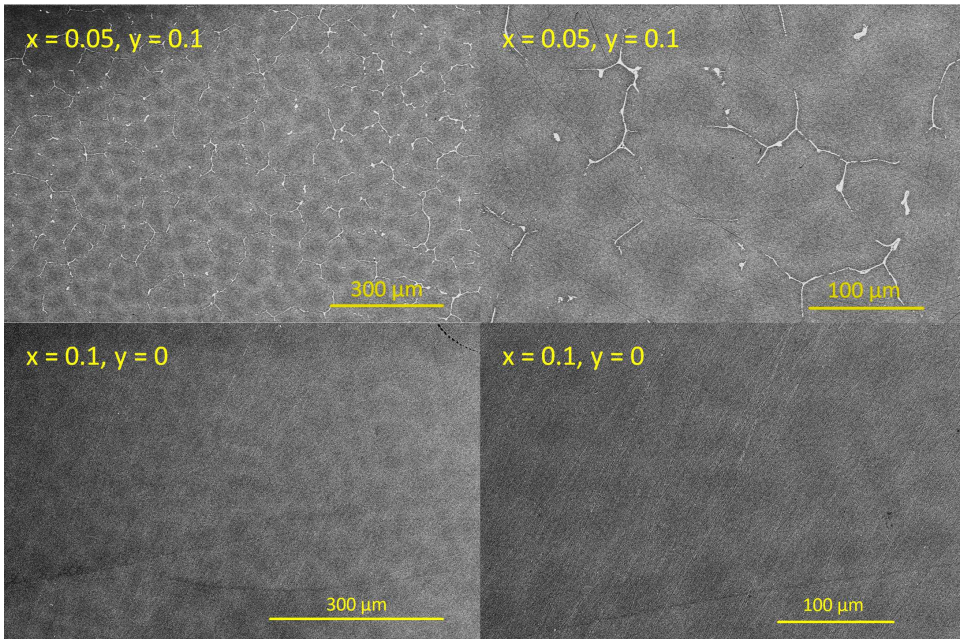

Figure 5.5: Diffuse contrasts in the SEM images of $Fe_2V_{0.9}Ta_{0.1}Al$ and $Fe_2V_{0.95}Ta_{0.05}Al_{0.9}Si_{0.1}$ which have been annealed at 1073 K for one week.

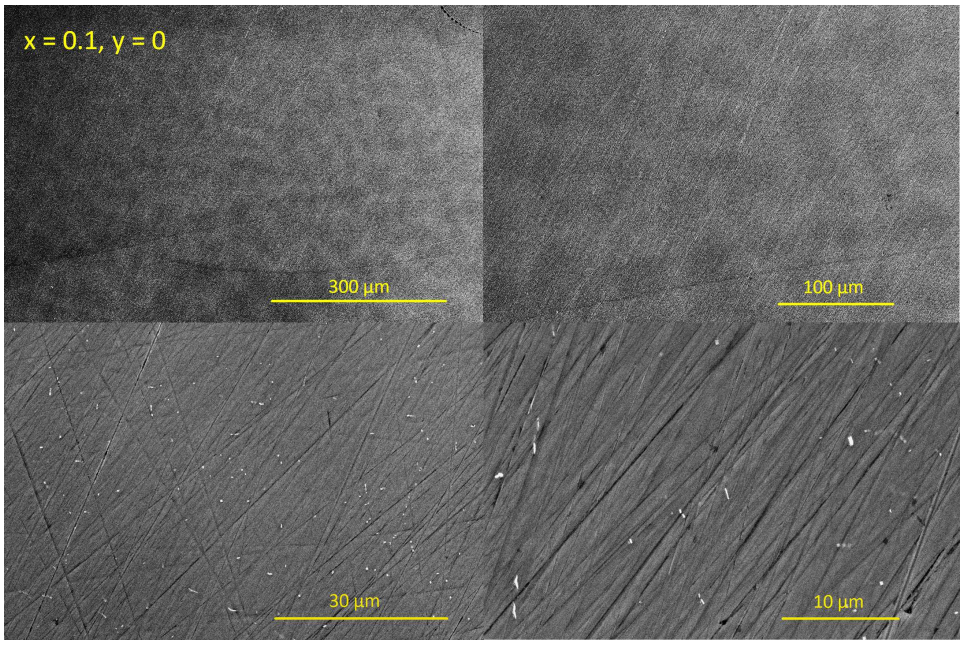

Figure 5.6: $Fe_2V_{0.9}Ta_{0.1}Al$, annealed at 1073 K for one week. SEM images at a higher magnification show nanoscale Laves precipitates that emerge inside the regions of oversaturated Heusler phase.

Die approbierte gedruckte Originalversion dieser Diplomarbeit ist an der TU Wien Bibliothek verfügbar.
The approved original version of this thesis is available in print at TU Wien Bibliothek.
TU Bibliothek Your knowledge hub WIEN

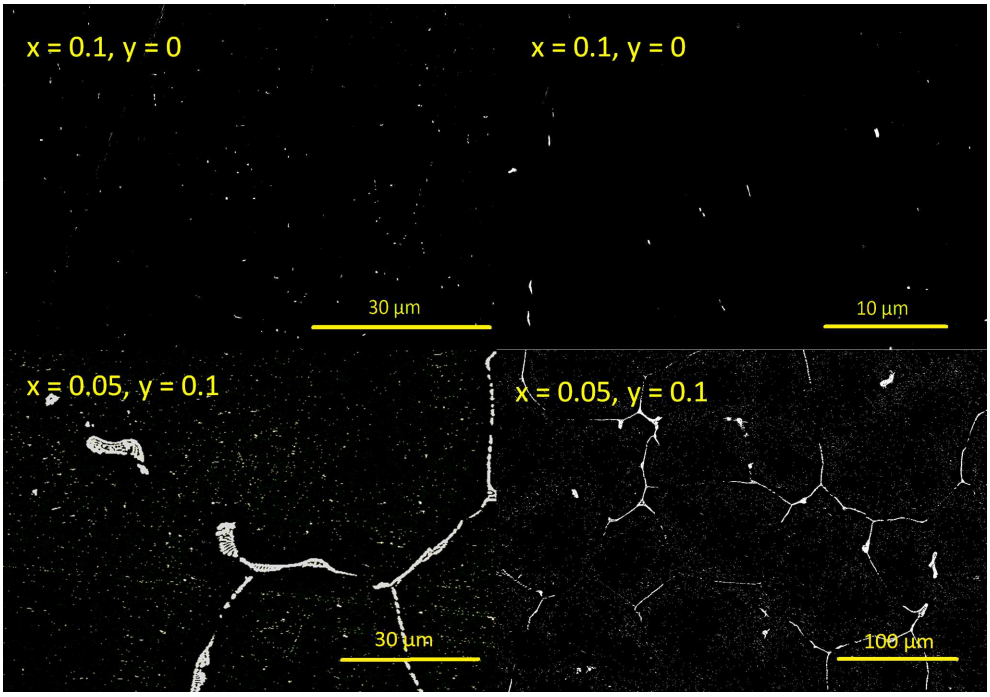

Figure 5.7: High contrast SEM images of $Fe_2V_{1-x}Ta_xAl_{1-y}Si_y$, annealed at 1073 K for one week. Nanoscale impurity precipitates which grow in size until they connect and form grain boundaries.

5.2.2 Microstructural evolution with annealing

Due to the fact that $Fe_2V_{0.95}Ta_{0.05}Al_{0.9}Si_{0.1}$ shows signs of a non-equilibrium state together with very promising thermoelectric properties, different annealing conditions varying temperature and annealing duration (see section 4.2) were tested in order to investigate the effect of annealing and to possibly dissolve the impurity phase. However, as can be seen in Figure 5.8, the amount of secondary phase increased with annealing time and revealed a diversity of microstructures for the respectively applied annealing conditions. When increasing the annealing duration by one week and the temperature to 1373 K and 1273 K, the diffuse contrasts disappeared and were instead replaced by clearly visible grain boundaries that formed distinct grains with a diameter of a few hundred micrometers, as can be seen in the upper right image of Figure 5.8. Inside those grains a lot of point-shaped precipitation was observed, which almost completely vanished upon further increasing the annealing duration. The microstructure continued to change and the most amount of secondary phase showed up for the sample which was annealed for 38 days at 1073 K. In summary, the complete dissolution of Ta and Si into the full-Heusler structure turned out to be unsuccesful and in fact the amount of impurity phase increased with annealing time. Figure 5.9 shows a high contrast image of

Die approbierte gedruckte Originalversion dieser Diplomarbeit ist an der TU Wien Bibliothek verfügbar.
The approved original version of this thesis is available in print at TU Wien Bibliothek.
TU Bibliothek WIEN Your knowledge hub

$Fe_2V_{0.95}Ta_{0.05}Al_{0.9}Si_{0.1}$, annealed for 14 days and 17 days respectively, as depicted in section 4.2. The previously described microstructures once again show the precipitation of an impurity phase, which segregate within grain boundaries, as well as unconnected precipitates that accumulate in certain regions which are depicted by the yellow lines. When following the alignment of the unconnected precipitates one can expect the emergence of new grain boundaries within those regions. This leads to a microstructure with smaller grain size and more pronounced grain boundaries. Ultimately, if the composition is changed towards $Fe_2V_{0.9}Ta_{0.1}Al_{0.9}Si_{0.1}$ or when the annealing time is increased to 38 days for $Fe_2V_{0.95}Ta_{0.05}Al_{0.9}Si_{0.1}$, a lamellar structure is obtained. Figure 5.10 shows SEM images at different magnifications for the eutectic Laves phase which is embedded in the full-Heusler phase. It is quite remarkable that two different compositions yield an almost identical microstructure. This once again shows that this two-phase system is very susceptible to a variation of the annealing parameters.

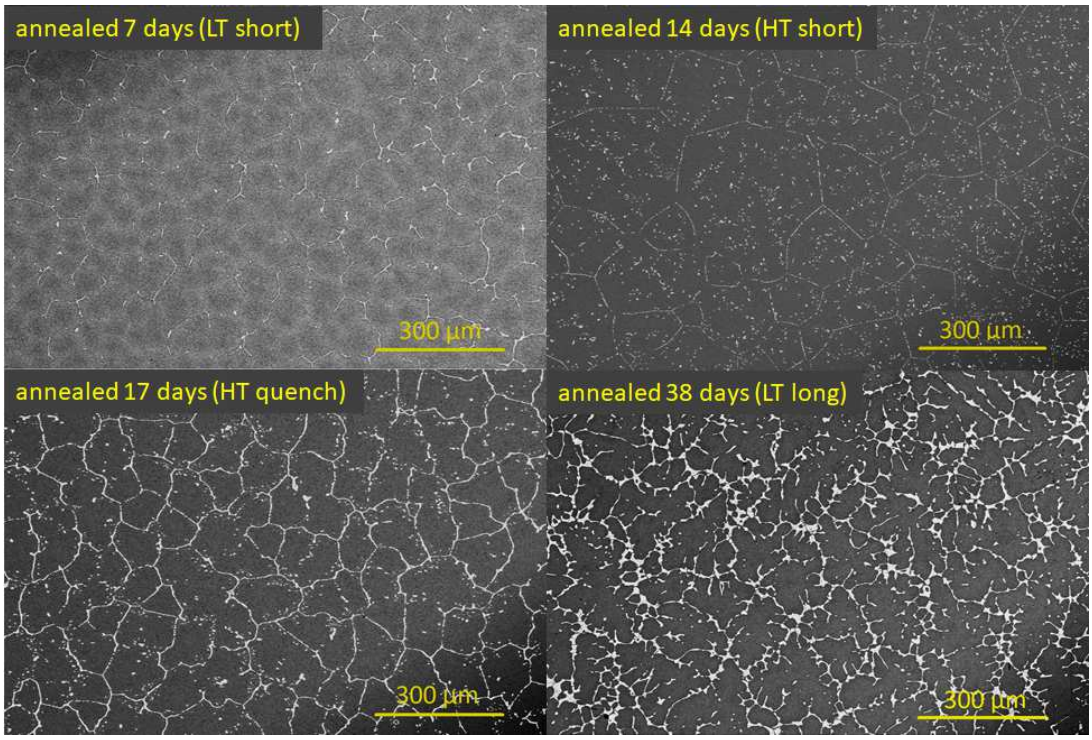

Figure 5.8: $Fe_2V_{0.95}Ta_{0.05}Al_{0.9}Si_{0.1}$ under different annealing conditions varying annealing duration and temperature which results in a multitude of different microstructures. The amount of secondary phase increases with annealing time.

Die approbierte gedruckte Originalversion dieser Diplomarbeit ist an der TU Wien Bibliothek verfügbar.
The approved original version of this thesis is available in print at TU Wien Bibliothek.
TU Bibliothek WIEN Your knowledge hub

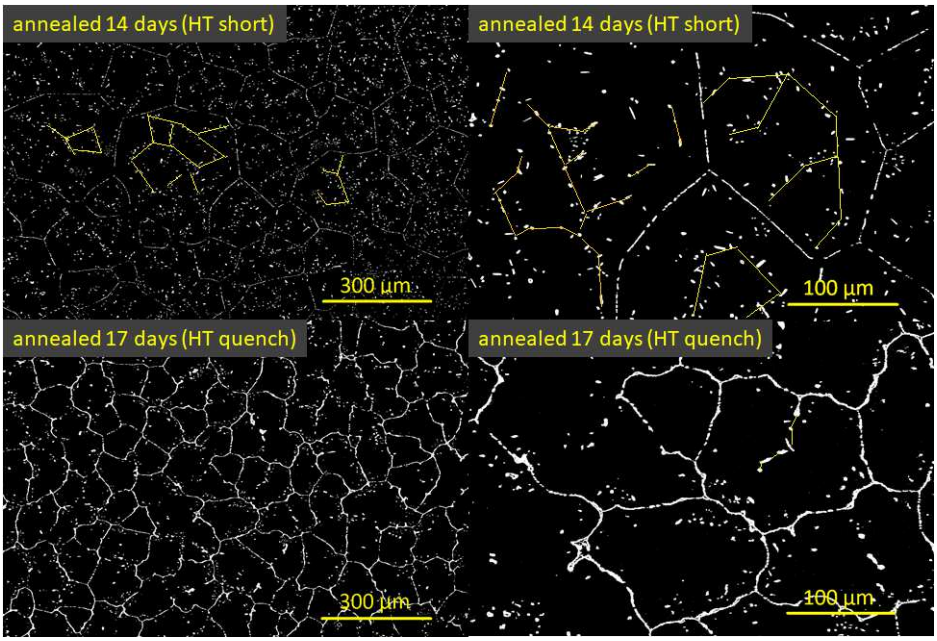

Figure 5.9: High contrast SEM images of $Fe_2V_{0.95}Ta_{0.05}Al_{0.9}Si_{0.1}$ under different annealing conditions. Unconnected Laves precipitates accumulate in regions which are marked by yellow lines. A reduction of grain size due to the formation of new grain boundaries is expected.

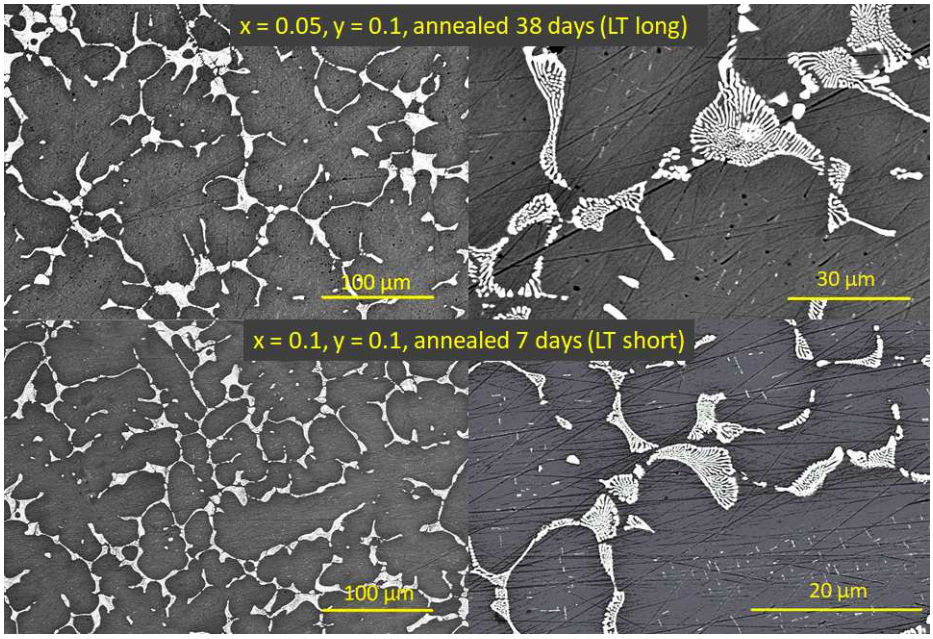

Figure 5.10: SEM images of $Fe_2V_{0.95}Ta_{0.05}Al_{0.9}Si_{0.1}$ and $Fe_2V_{0.9}Ta_{0.1}Al_{0.9}Si_{0.1}$, annealed at 1073 K for 38 days and one week respectively. An almost identical microstructure is obtained where a lamellar Laves phase is embedded in the Heusler matrix.

Die approbierte gedruckte Originalversion dieser Diplomarbeit ist an der TU Wien Bibliothek verfügbar.
The approved original version of this thesis is available in print at TU Wien Bibliothek.
TU WIEN Bibliothek Your knowledge hub

5.3 Electrical resistivity

The electrical resistivitiy is one of the most fundamental properties of a material and directly reflects its abilitiy to transport electric charge carriers. Due to the fact that ρ is an all-embracing quantitiy that encompasses intrinsic material properties such as the band structure but also all extrinsic properties such as lattice defects and impurities, one has to be very cautious when interpreting values of ρ. It is therefore also of great interest to measure ρ in a wide temperature range and have some theoretical concept of what to expect from such a measurement. In this work we measured ρ from around 4 K up to 800 K for $Fe_2V_{1-x}Ta_xAl_{1-y}Si_y$-based compounds.

5.3.1 Effect of Ta- and Si-substitution

As already discussed in subsection 3.5.2 the elemental substitution of Ta on the V-site leads to a modification of the electronic band structure. More precisely, the lowest dispersive conduction band at the X point gets shifted towards higher energies, resulting in an opening of the pseudogap. Figure 5.11 and Figure 5.12 support that statement and show that the low temperature resistivity is almost doubled when x goes up.

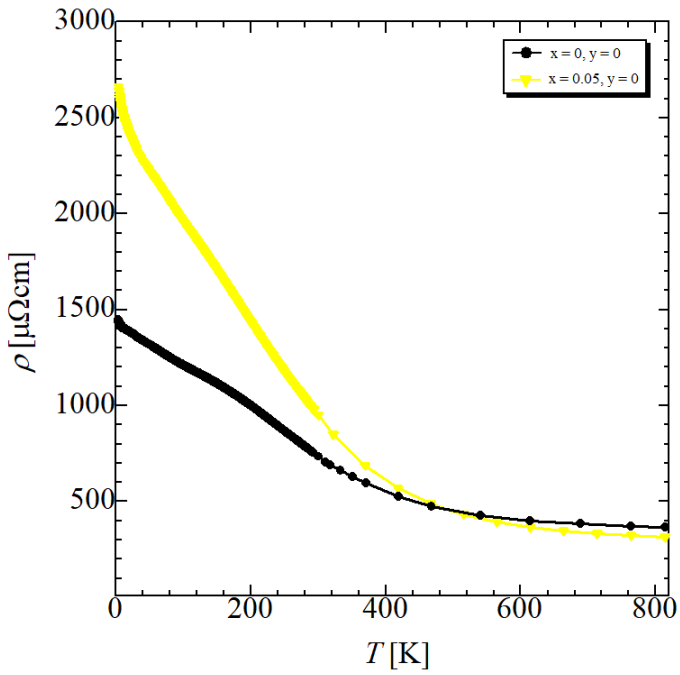

Figure 5.11: Temperature dependence of electrical resistivity of $Fe_2V_{1-x}Ta_xAl_{1-y}Si_y$ annealed at 1073 K for one week.

Die approbierte gedruckte Originalversion dieser Diplomarbeit ist an der TU Wien Bibliothek verfügbar.
The approved original version of this thesis is available in print at TU Wien Bibliothek.
TU Bibliothek WIEN Your knowledge hub

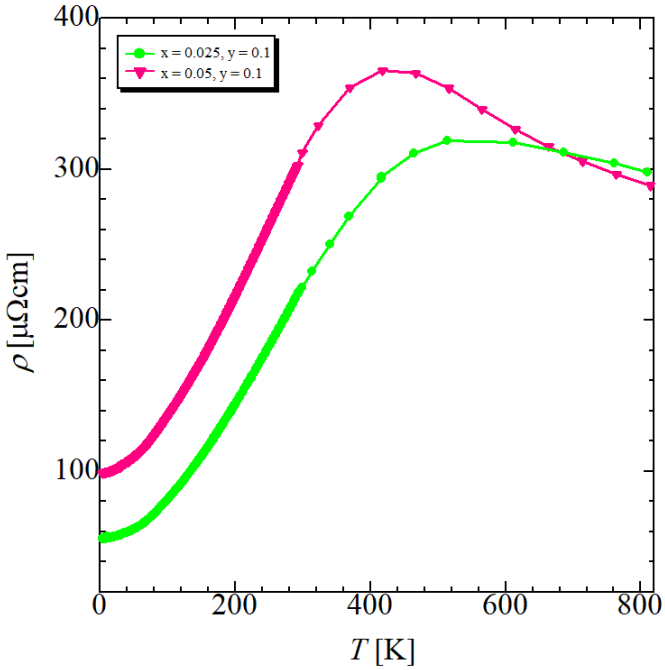

Figure 5.12: Temperature dependence of electrical resistivity of $Fe_2V_{1-x}Ta_xAl_{1-y}Si_y$ annealed at 1073 K for one week. The low temperature resistivtiy is increased for a higher amount of Ta-substitution.

Figure 5.13 shows the resistivity curves for all synthesized samples which were annealed at 1073 K for one week. The effect of Si-substitution according to the rigid band model can clearly be seen at first glance as the semiconductor-like nature of the low temperature resistivity quickly vanishes upon carrier doping. Instead, a very metallic behaviour of ρ can be observed for low temperatures that only recedes above room temperature or at higher temperatures when the excitation of charge carriers in the valence band leads to a decrease of ρ. As already mentioned, this effect is well explicable in the rigid band model where a rigid shift of the Fermi energy towards the conduction band is predicted. Nonetheless, there are some samples whose resistivity behaviour cannot be explained by the two previously described assumptions and which will be discussed in the next section.

Die approbierte gedruckte Originalversion dieser Diplomarbeit ist an der TU Wien Bibliothek verfügbar.
The approved original version of this thesis is available in print at TU Wien Bibliothek.
TU Bibliothek WIEN Your knowledge hub

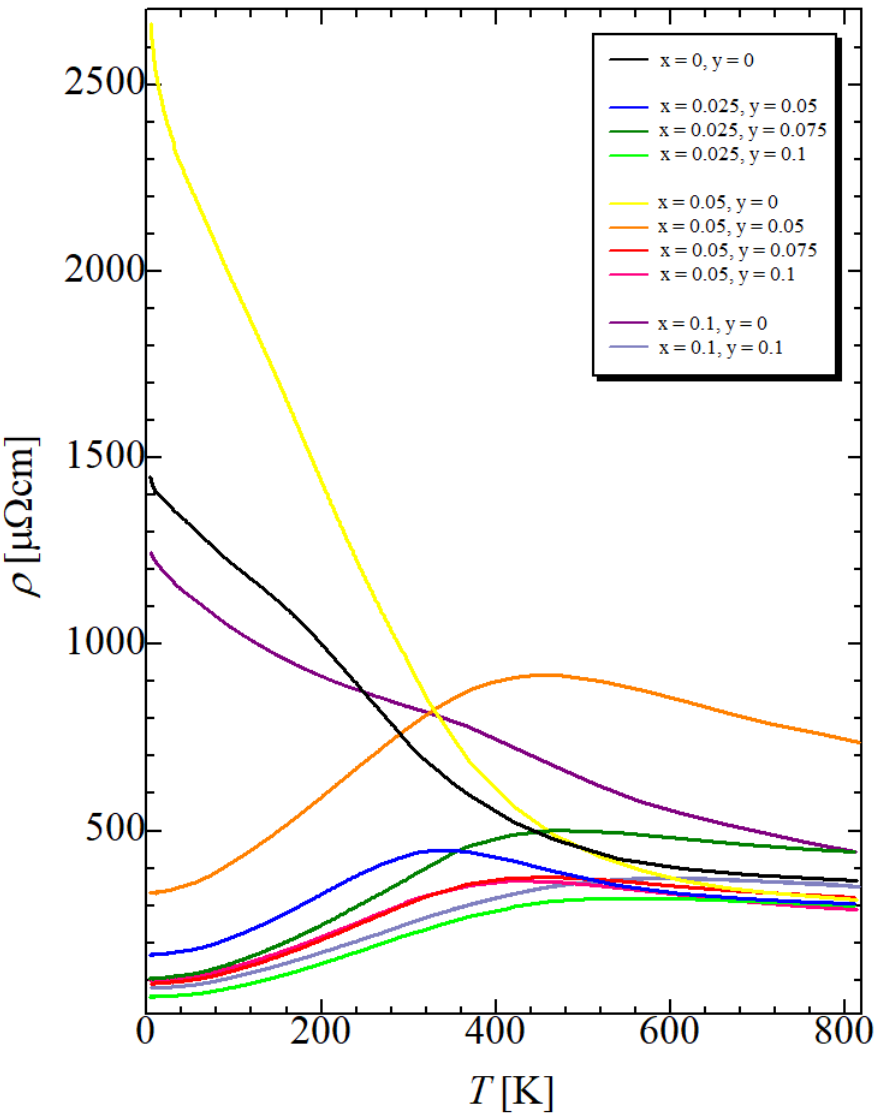

Figure 5.13: Temperature dependence of electrical resistivity of $Fe_2V_{1-x}Ta_xAl_{1-y}Si_y$, annealed at 1073 K for one week.

Die approbierte gedruckte Originalversion dieser Diplomarbeit ist an der TU Wien Bibliothek verfügbar.
The approved original version of this thesis is available in print at TU Wien Bibliothek.
TU Bibliothek Your knowledge hub WIEN

5.3.2 Effect of impurity phase and annealing

Figure 5.14 shows two samples for which an increase of x unintuitively leads to a decrease in ρ. The study of the microstructure by SEM leads to the conclusion that the solubility limit for Ta is rather low and an impurity phase with metallic characteristics appears. This explains the fact that ρ does not continue to increase above a certain composition x and instead shows metallic features. Even though the nanoscale composites of secondary phase are unconnected in the microstructure of $Fe_2V_{0.9}Ta_{0.1}Al$, the resistivity seems to be strongly affected. This however is not uncommon as a composite effect that foresees a reduction of ρ by metallic nanoinclusions has already been frequently reported in the past [20, 48, 57].
The microstructural evolution by variation of the annealing conditions, which was explained in the previous sections, gave the conclusion that the amount of secondary phase precipitates increased homogeneously across the sample. This directly reflects in the electrical resistivity, as can be seen in Figure 5.15. The low temperature values of ρ gradually decline with annealing time and the maximum of the resistivity curves shift towards higher temperatures as the metallic behaviour caused by the impurity phase prevails.

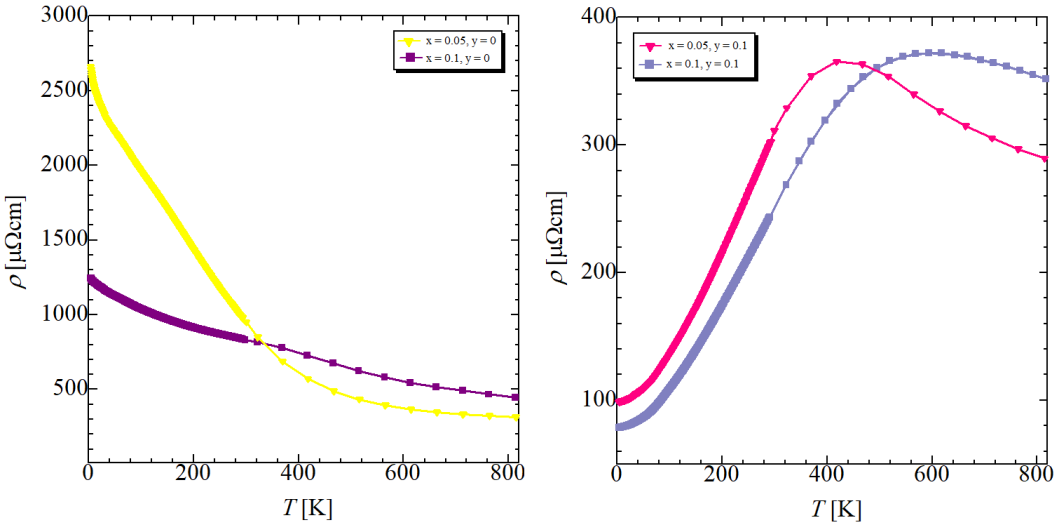

Figure 5.14: Temperature dependence of electrical resistivity of $Fe_2V_{1-x}Ta_xAl_{1-y}Si_y$, annealed at 1073 K for one week. Metallic secondary phase severely affects ρ.

Die approbierte gedruckte Originalversion dieser Diplomarbeit ist an der TU Wien Bibliothek verfügbar.
The approved original version of this thesis is available in print at TU Wien Bibliothek.
TU Bibliothek Your knowledge hub WIEN

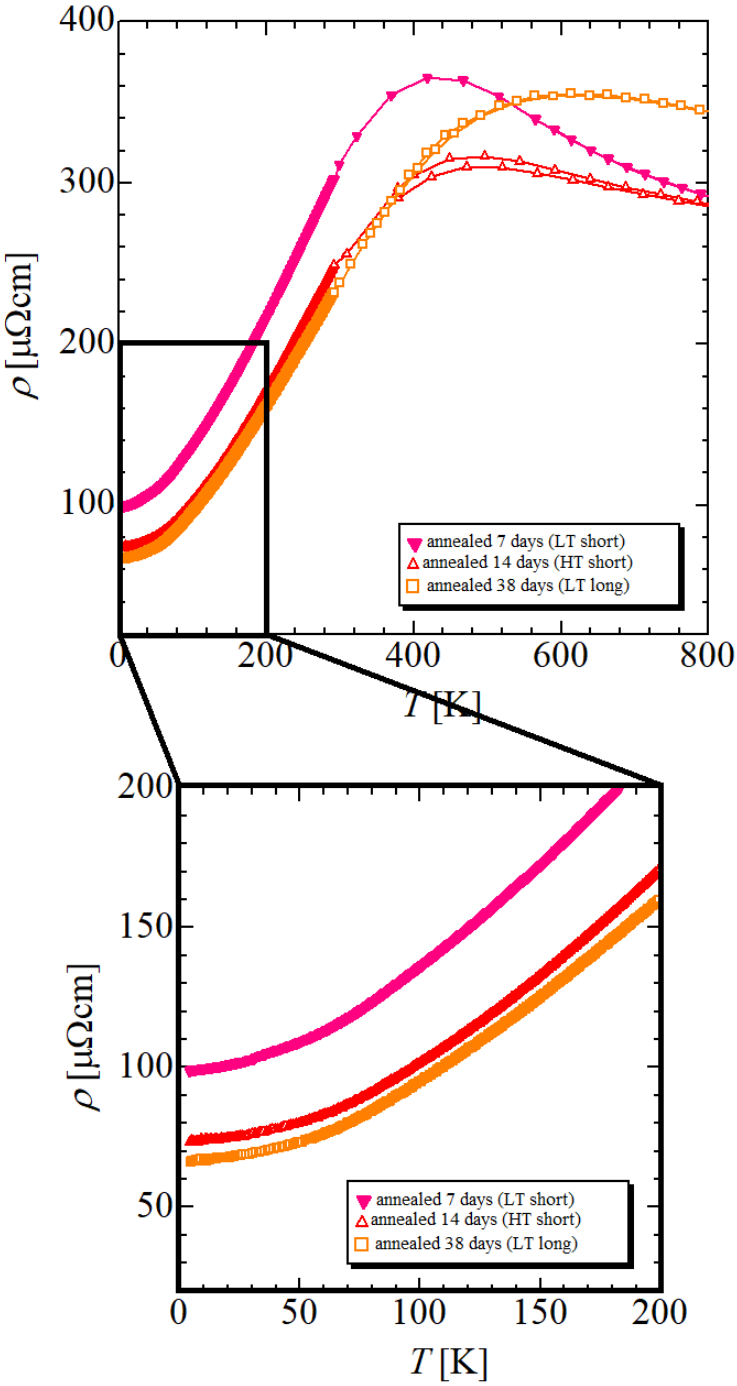

Figure 5.15: Temperature dependence of electrical resistivity of $Fe_2V_{0.95}Ta_{0.05}Al_{0.9}Si_{0.1}$ under different annealing conditions. Metallic secondary phase reduces ρ at low temperatures.

Die approbierte gedruckte Originalversion dieser Diplomarbeit ist an der TU Wien Bibliothek verfügbar.
The approved original version of this thesis is available in print at TU Wien Bibliothek.
TU Bibliothek Your knowledge hub WIEN

5.4 Seebeck coefficient

The Seebeck coefficient is an intrinsic material property which mainly depends on the carrier concentration, effective mass, electron and hole mobility and the energy dependence of the electron relaxation time of a material. It can be measured as the linear response of a thermoelectric voltage to an applied temperature gradient. One can safely say that it should be a primary concern to have a high S in order to attain high values of ZT, when building a thermoelectric device. Due to its remarkable DOS in both directions of the Fermi energy, Fe_2VAl shows promising values of S when appropriately doped. In the following, it will be shown that by substituting Ta for V and Si for Al some of the highest Seebeck coefficients in stoichiometric Fe_2VAl-based compounds can be obtained.

5.4.1 Effect of Ta- and Si-substitution

The proclaimed opening of the pseudogap as well as the expected convergence of dispersive bands in the valence band and in the conduction band at the X point should lead to an increase of the Seebeck coefficient for both p-type and n-type samples. Such an improvement of S could assuredly be observed and is shown in Figure 5.16. Albeit the resistivity was decreased in $Fe_2V_{1-x}Ta_xAl$ for $x = 0.05 \rightarrow x = 0.1$, S did not deteriorate, but instead even increased by a striking amount. While $S \approx 30\,\mu V/K$ in Fe_2VAl, S is almost quadrupled in $Fe_2V_{0.9}Ta_{0.1}Al$. This is quite astonishing as the low temperature electrical resistivity was also reduced by half of its orgininal value. A possible explanation for the high Seebeck coefficient could be the so-called energy filtering effect, which has been widely accepted as a way to increase S [10, 30, 40, 69]. Here, a strong energy dependence of the electron scattering time is assumed and taken advantage of. Low energy charge carriers will be scattered more strongly and will therefore be filtered by potential barriers which are present in the material in the form of interfaces or heterostructures. Especially metallic impurity inclusions which are evenly dispersed over a semiconductor-like host material are believed to lead to such interface potentials. This gives rise to band bending and the formation of a so-called Schottky barrier at the metal-semiconductor boundaries and has a severe impact on the transport of electric charge carriers [10, 14].
Figure 5.17 shows the Seebeck coefficient of all samples which were annealed at 1073 K for one week as a function of temperature from 300 K up to 800 K. The Si-doping effect can clearly be observed as S rapidly changes its sign and takes large absolute values due to the rigid-band-like shift of E_F to a steep position at the edge of the electronic DOS. However, as opposed to $Fe_2VAl_{1-y}Si_y$-based compounds, which are found to possess maximum values of $|S|$ that are about $120 - 130\,\mu V/K$, most samples of this study rank slightly above those.

Die approbierte gedruckte Originalversion dieser Diplomarbeit ist an der TU Wien Bibliothek verfügbar.
The approved original version of this thesis is available in print at TU Wien Bibliothek.
TU WIEN Bibliothek Your knowledge hub

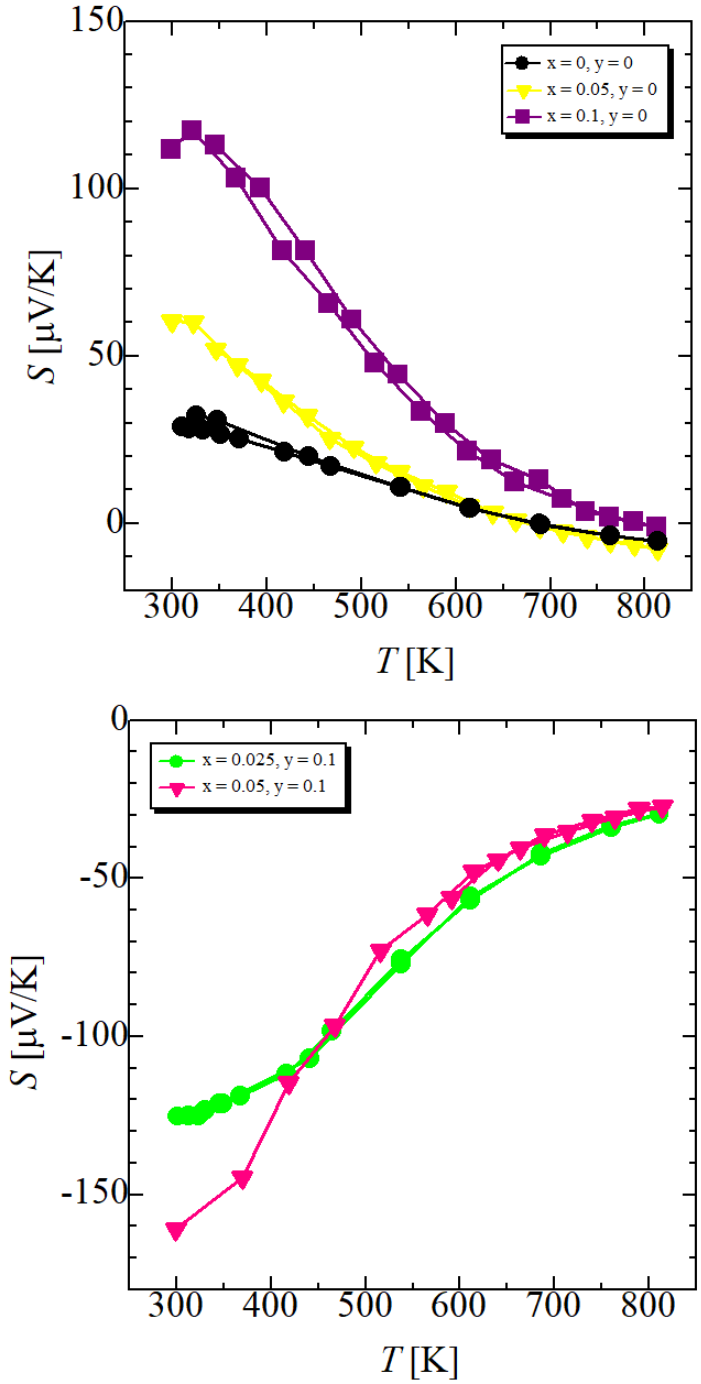

Figure 5.16: Seebeck coefficient as a function of temperature for $Fe_2V_{1-x}Ta_xAl_{1-y}Si_y$, annealed at 1073 K for one week. The opening of the pseudogap caused by the substitution of Ta leads to an increase of S.

Die approbierte gedruckte Originalversion dieser Diplomarbeit ist an der TU Wien Bibliothek verfügbar.
The approved original version of this thesis is available in print at TU Wien Bibliothek.
TU Bibliothek Your knowledge hub WIEN

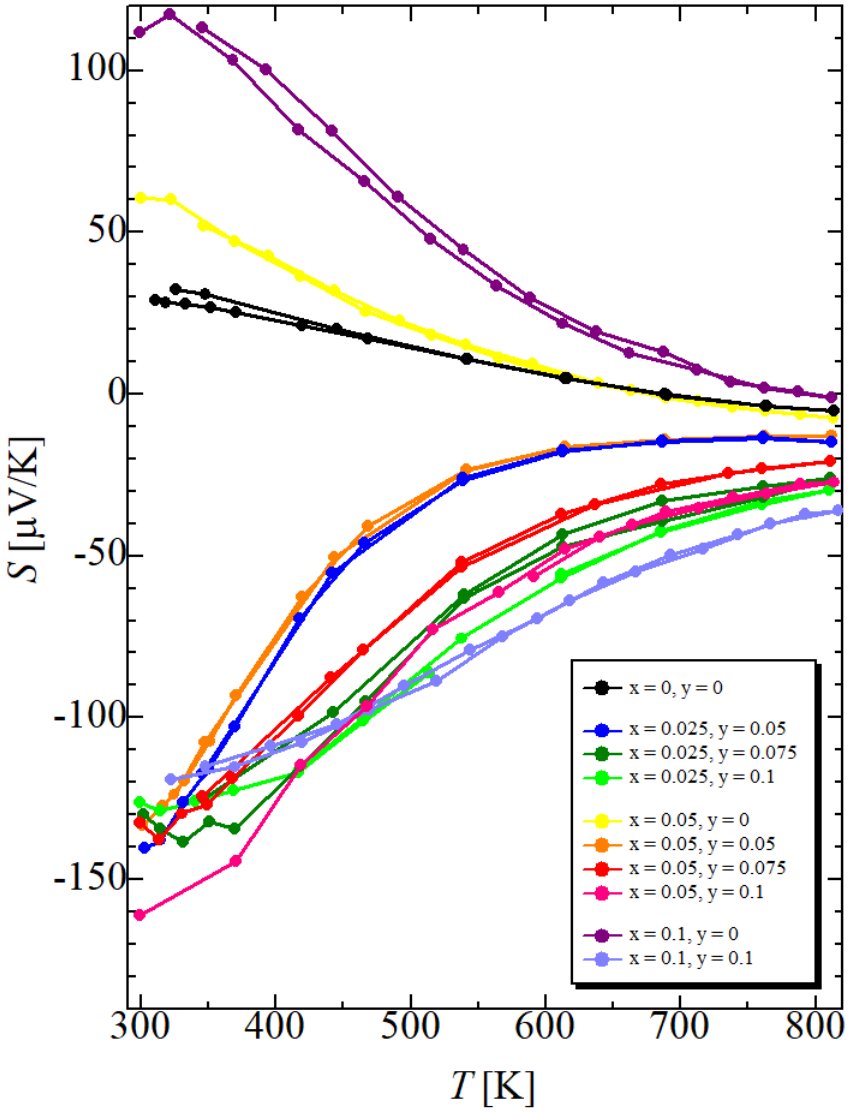

Figure 5.17: Seebeck coefficient as a function of temperature for all samples with the composition $Fe_2V_{1-x}Ta_xAl_{1-y}Si_y$ that were annealed at 1073 K for one week.

Die approbierte gedruckte Originalversion dieser Diplomarbeit ist an der TU Wien Bibliothek verfügbar.
The approved original version of this thesis is available in print at TU Wien Bibliothek.
TU Bibliothek Your knowledge hub WIEN

5.4.2 Effect of impurity phase and annealing

A rather speculative attempt to explain the simultaneous improvement of S and ρ in $Fe_2V_{0.9}Ta_{0.1}Al$ was given with the energy filtering effect in the previous section. Such effect, if present at all, is expected to occur for nanoscale precipitates only, when a sufficient amount of interfaces is provided. A large amount of metallic phase will most definitely decrease S, especially if the precipitates are connected and establish a path for the charge carriers. Figure 5.18 shows the effect of the secondary phase and microstructure on the Seebeck coefficient of $Fe_2V_{0.95}Ta_{0.05}Al_{0.9}Si_{0.1}$ and $Fe_2V_{0.9}Ta_{0.1}Al_{0.9}Si_{0.1}$. At room temperature S decreases with annealing time as more of the impurity phase percolates. Both samples that equally display a lamellar microstructure exhibit an almost identical behaviour for the Seebeck coefficient. This once again exemplifies the importance of the microstructure regarding the thermoelectric properties.

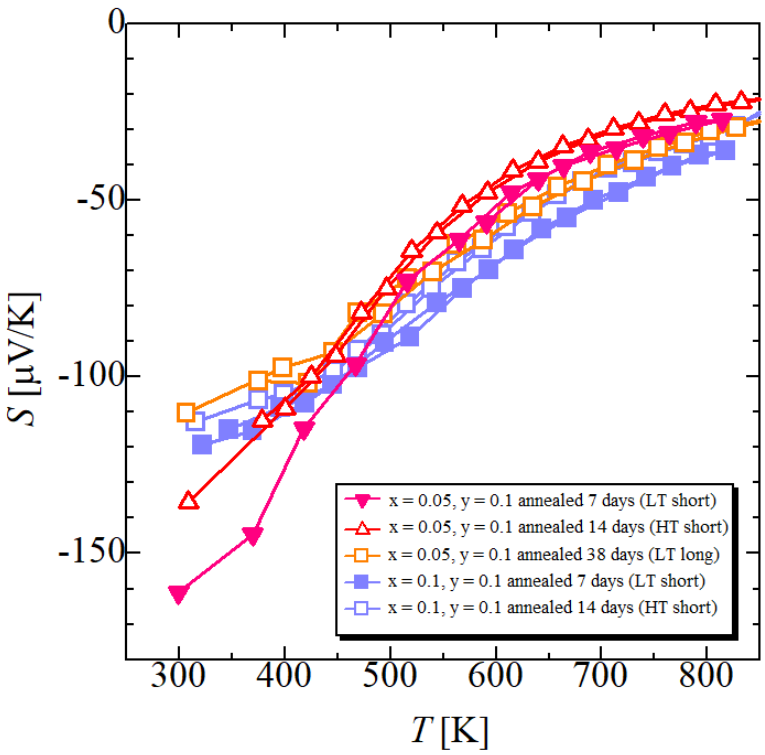

Figure 5.18: Seebeck coefficient as a funtion of temperature for $Fe_2V_{0.95}Ta_{0.05}Al_{0.9}Si_{0.1}$ and $Fe_2V_{0.9}Ta_{0.1}Al_{0.9}Si_{0.1}$ under different annealing conditions. Metallic secondary phase reduces S.

Die approbierte gedruckte Originalversion dieser Diplomarbeit ist an der TU Wien Bibliothek verfügbar.
The approved original version of this thesis is available in print at TU Wien Bibliothek.
TU Bibliothek Your knowledge hub WIEN

5.5 Power factor

Figure 5.19 shows the temperature dependence of the calculated power factor for all samples based on $Fe_2V_{1-x}Ta_xAl_{1-y}Si_y$ that were annealed at 1073 K for one week. Here PF_{max} was around $7-8\,mW/mK^2$ which is among the highest reported values in Fe_2VAl-based bulk materials.

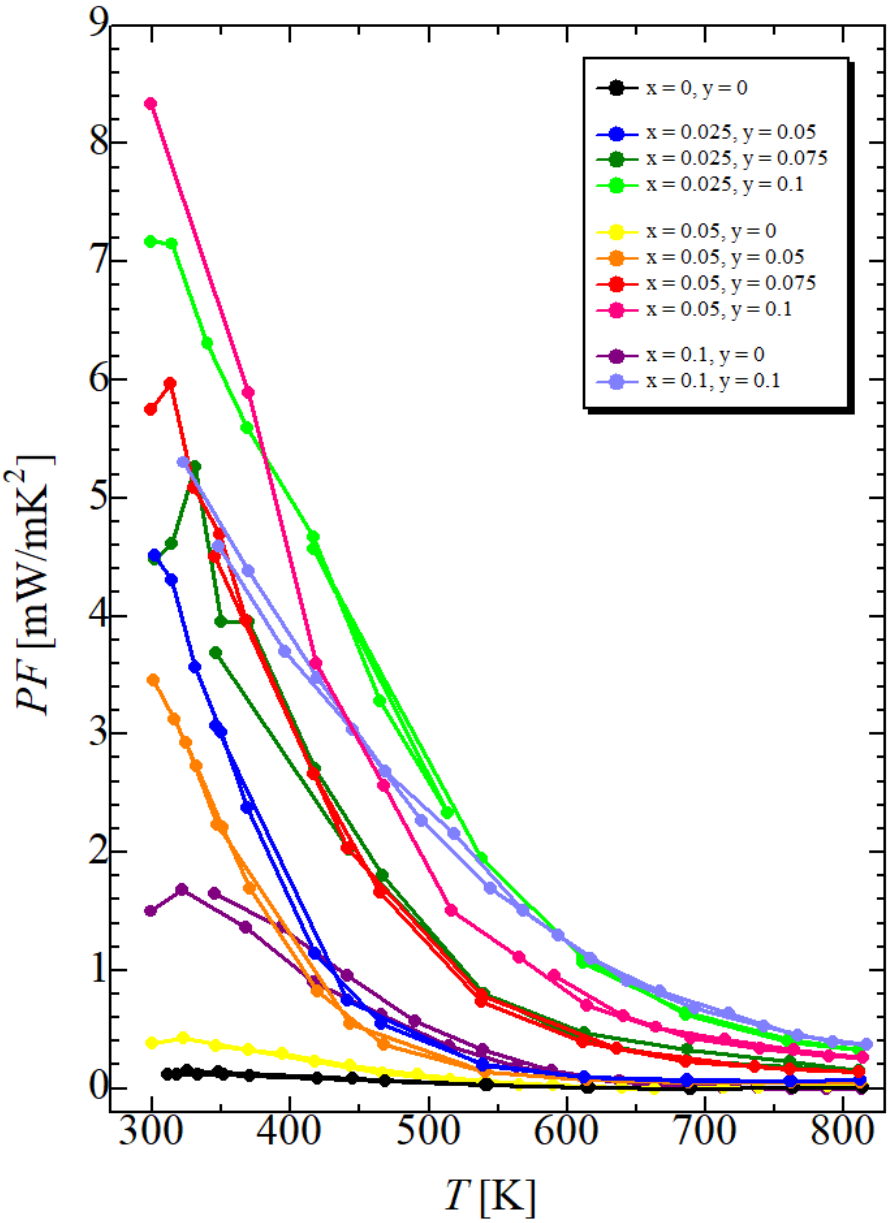

Figure 5.19: Power factor for all samples based on $Fe_2V_{1-x}Ta_xAl_{1-y}Si_y$ that were annealed at 1073 K for one week.

Die approbierte gedruckte Originalversion dieser Diplomarbeit ist an der TU Wien Bibliothek verfügbar.
The approved original version of this thesis is available in print at TU Wien Bibliothek.
TU Bibliothek Your knowledge hub WIEN

While a large amount of the secondary phase in the microstructure decreases the power factor as suggested in Figure 5.20, there seems to be an improvement of PF for a microstructure that shows a small amount of nanoscale precipitates, which are evenly spread across the sample and are unconnected. An overall improvement of 30-50 % compared to $Fe_2VAl_{1-y}Si_y$ samples from literature was achieved as shown in Figure 5.21 [42]. The significant improvement of S together with very low values of ρ at room temperature are responsible for that matter.

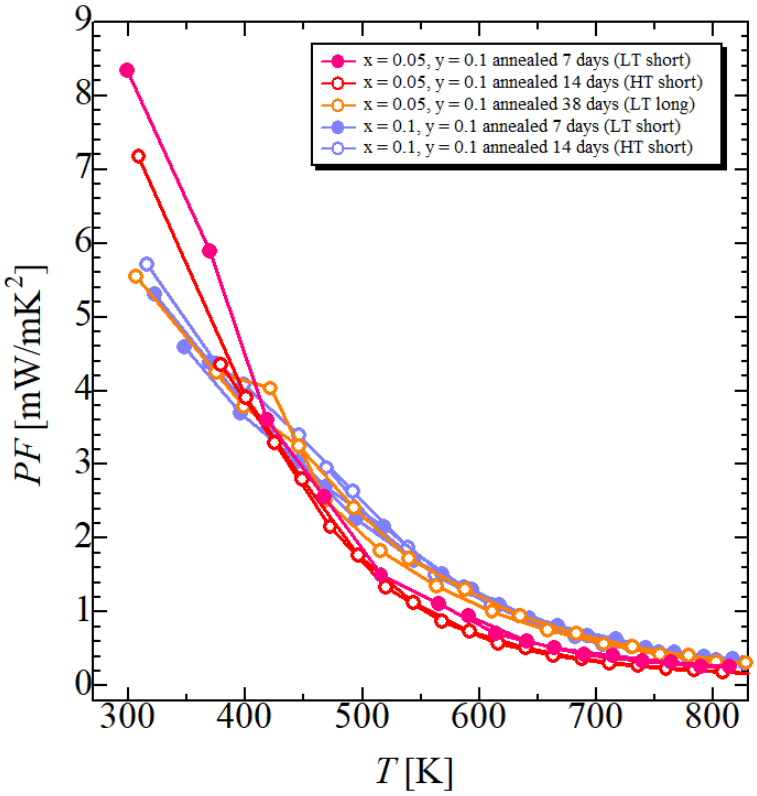

Figure 5.20: Power factor of $Fe_2V_{0.95}Ta_{0.05}Al_{0.9}Si_{0.1}$ and $Fe_2V_{0.9}Ta_{0.1}Al_{0.9}Si_{0.1}$ under different annealing conditions.

Die approbierte gedruckte Originalversion dieser Diplomarbeit ist an der TU Wien Bibliothek verfügbar.
The approved original version of this thesis is available in print at TU Wien Bibliothek.
TU Bibliothek Your knowledge hub WIEN

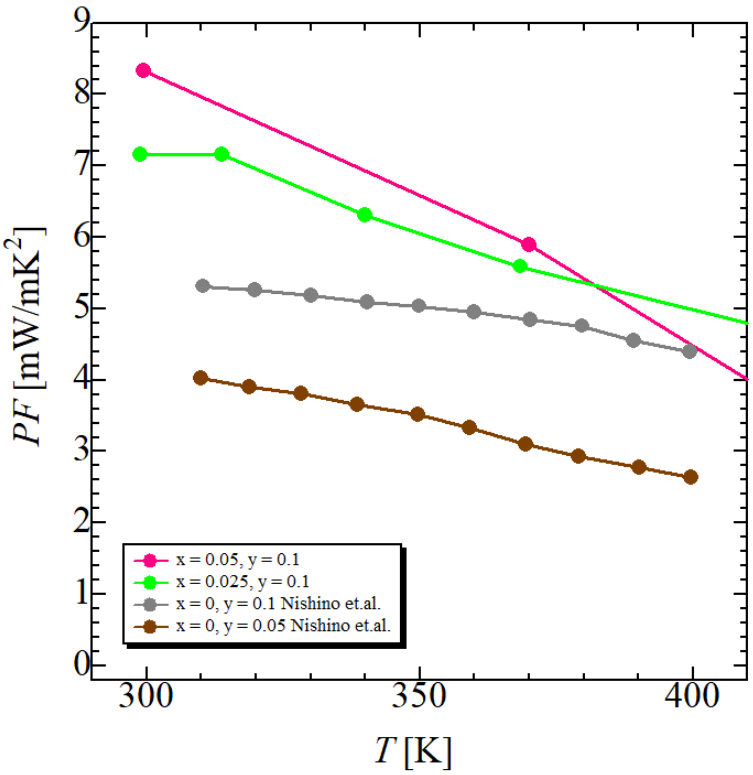

Figure 5.21: Comparison of the power factor of $Fe_2V_{1-x}Ta_xAl_{1-y}Si_y$ with literature.

Die approbierte gedruckte Originalversion dieser Diplomarbeit ist an der TU Wien Bibliothek verfügbar.
The approved original version of this thesis is available in print at TU Wien Bibliothek.

6 Conclusion

To summarize this work, we investigated stoichiometric full-Heusler compounds based on $Fe_2V_{1-x}Ta_xAl_{1-y}Si_y$ with respect to two major aspects:

1) The evolution of the microstructure with composition and annealing.
2) The thermoelectric properties, specifically the temperature dependent electrical resistivity and thermopower.

Co-doping of Ta and Si leads to the precipitation of a Ta- and Si-rich secondary phase, which was identified by XRD as a Laves phase that crystallizes in the hexagonal C14 structure. We found that both doping elements procure the impurity phase and established a solubility limit that is slightly below $y = 0.1$ for samples with $x = 0.05$ and just below $x = 0.1$ for samples with $y = 0$. Those borderline cases showed diffuse contrasts in the SEM images which is an indication for a non-equilibrium state. The evolution of the microstructure included several steps and started with the emergence of unconnected precipitates within supersaturated regions of the full-Heusler phase. By either increasing the doping parameters x, y or with further annealing time, one could observe that a higher amount of the impurity phase percolated, which resulted in a grain-like microstructure with grain boundary segregation of Laves-type impurities. This impurity phase ultimately forms a lamellar microstructure, which is embedded in the full-Heusler phase. Results for ρ and S in this work reaffirmed the results from DFT calculations, predicting an opening of the pseudogap for a Ta-substitution on the V-site. This effect, together with an optimized microstructure, leads to an improvement of the thermoelectric properties. We measured Seebeck coefficients of $S_{\max} \approx -160\,\mu\mathrm{V/K}$ near room temperature, together with low values of resistivity $\rho \approx 310\,\mu\Omega\mathrm{cm}$. Due to its metallic character, the impurity phase simultaneously decreased S and ρ, but kept PF astonishingly high. A power factor $PF \approx 7 - 8\,\mathrm{mW/mK^2}$ was achieved, which is an overall improvement of 30-50 % compared to $Fe_2VAl_{1-y}Si_y$-based compounds from literature.

Future work

Lately, reducing the thermal conductivity seems to have been the main strategy for enhancing ZT [24, 27, 34]. This study shows that albeit the power factor is already very high in full-Heusler materials compared to other thermoelectric material

Die approbierte gedruckte Originalversion dieser Diplomarbeit ist an der TU Wien Bibliothek verfügbar.
The approved original version of this thesis is available in print at TU Wien Bibliothek.
TU WIEN Bibliothek Your knowledge hub

classes, it can still be significantly improved. As a future work, the solubility limit of Ta and Si in $Fe_2V_{1-x}Ta_xAl_{1-y}Si_y$ could be further substantiated for $x > 0.05$ and $y < 0.1$. In order to give an estimate of ZT, we also want to measure the thermal conductivity for the respective microstructures in section 5.2, which we expect to be very low due to the effect of heavy element doping by Ta. Co-doping of W and Ta instead of Si and Ta could also pose as an effective way of simultaneously reducing λ_{lattice} through increased phonon scattering, while achieving similar values of PF as in this work. The effect of secondary Laves-type impurity phases needs to be further tested with the goal to find a reproducible way of improving the thermoelectric properties of Fe_2VAl-based full-Heusper compounds by microstructural control.

Die approbierte gedruckte Originalversion dieser Diplomarbeit ist an der TU Wien Bibliothek verfügbar.
The approved original version of this thesis is available in print at TU Wien Bibliothek.
TU Bibliothek WIEN Your knowledge hub

Acknowledgements

Here, I would like to sincerely express my gratitude for all of my supervisors, contributors and others that showed their patience and support of this thesis.

Firstly, I would especially like to thank Prof. Kaoru Kimura for his welcoming attitude and hospitality at the The University of Tokyo. His effort and guidance not only helped me to progress my research for this thesis but also inspired and motivated me to continue working in the academic field. Secondly, I want to thank Prof. Yukari Katsura for her participation in this work. I greatly appreciate her astute and critical way of thinking as well as her profound knowledge in the field. My sincere thanks also goes to Dr. Kazuki Tobita, who helped me in all aspects with my research, theoretically and practically and who was above all an excellent mentor and advisor.

From my research group at the TU Wien I want to deeply thank Prof. Ernst Bauer for his continuous support and interest in this work, his insightful comments and encouragement as well as my lab mates Dipl.-Ing. Alexander Riss, Dipl.-Ing. Michael Parzer and Dipl.-Ing. Bernhard Hinterleitner for the ongoing efforts and stimulating discussions they provided. Their ideas highly contributed to the writing of this thesis.

I also want to point out the assistance of USTEM and the X-ray center (XRC) at the TU Wien for providing their equipment.

Last but not least, I would like to thank my family, especially my parents who supported me throughout my entire life by fostering and encouraging my interests and capabilities as well as my high school teacher who motivated me to study physics.

Die approbierte gedruckte Originalversion dieser Diplomarbeit ist an der TU Wien Bibliothek verfügbar.
The approved original version of this thesis is available in print at TU Wien Bibliothek.
TU Bibliothek WIEN Your knowledge hub

List of Figures

Figure 1.1 Seebeck and Peltier effect 2
Figure 1.2 Thermoelectric power conversion efficiency 3
Figure 1.3 Temperature dependence of ZT for various material classes 3
Figure 1.4 Carrier concentration dependence of S and ρ 4

Figure 2.1 Bloch wave 6
Figure 2.2 Evolution with time of a phase space element due to external forces 9
Figure 2.3 Selection function for charge transport driven by voltage gradients 14
Figure 2.4 Selection function for charge transport driven by temperature gradients 16
Figure 2.5 Selection funtion for thermal transport by electrons driven by temperature gradients 18
Figure 2.6 Selection funtion for thermal transport by phonons driven by temperature gradients 19
Figure 2.7 Convolution of voltage driven selection funtion with the electronic DOS of a 3D electron gas 22
Figure 2.8 Convolution of temperature driven selection funtion with the electronic DOS of a 3D electron gas 23
Figure 2.9 First Brillouin zone of a generic fcc crystal structure 24
Figure 2.10 Fermi surface and band convergence of $PbTe_{1-x}Se_x$ 25
Figure 2.11 Fermi surface of Fe_2VAl and Fe_2TiSn 25
Figure 2.12 First Hohenberg-Kohn theorem 27
Figure 2.13 Demonstration of an ARPES measurement 30
Figure 2.14 Momentum of a photo electron at a crystal boundary interface 31

Figure 3.1 $L2_1$ crystal structure of Fe_2VAl 34
Figure 3.2 NaCl-type and Zinc blende-type crystal structure 35
Figure 3.3 Orbital hybridization in Fe_2VAl 35
Figure 3.4 Most prominent types of atomic disorder in Fe_2VAl 36
Figure 3.5 XRD patterns of the $L2_1$, B2 and A2 structure 37
Figure 3.6 Temperature-induced phase transitions in Fe_2VAl 38

Die approbierte gedruckte Originalversion dieser Diplomarbeit ist an der TU Wien Bibliothek verfügbar.
The approved original version of this thesis is available in print at TU Wien Bibliothek.
TU WIEN Bibliothek Your knowledge hub

Figure 3.7 Isothermal sections of a complete ternary phase diagram for (Fe,V,Al) . . . 40
Figure 3.8 Calculated electronic DOS of Fe_2VAl . . . 42
Figure 3.9 Calculated band structure of Fe_2VAl . . . 42
Figure 3.10 Seebeck coefficient as a function of valence electron concentration for Fe_2VAl doped in the rigid band model . . . 44
Figure 3.11 Temperature dependence of the Seebeck coefficient and electrical resistivity of $Fe_2VAl_{1-x}Si_x$ . . . 45
Figure 3.12 Seebeck coefficient as a funtion of valence electron cocentration for Ta-doped samples based on Fe_2VAl . . . 46
Figure 3.13 Band structure of Fe_2VAl and Fe_2TaAl . . . 47

Figure 4.1 Compositions $Fe_2V_{1-x}Ta_xAl_{1-y}Si_y$ in this work . . . 49
Figure 4.2 Induction melting set-up . . . 50
Figure 4.3 Annealing conditions in this work . . . 51
Figure 4.4 Demonstration of Bragg's law . . . 52
Figure 4.5 Illustration of a Seebeck measurement . . . 54

Figure 5.1 XRD patterns of all samples, annealed at 1073 K for one week 56
Figure 5.2 XRD patterns of $Fe_2V_{1-x}Ta_xAl_{0.9}Si_{0.1}$ under various annealing conditions . . . 57
Figure 5.3 Lattice parameter . . . 58
Figure 5.4 Solubility limit of $Fe_2V_{1-x}Ta_xAl_{1-y}Si_y$ . . . 60
Figure 5.5 Microstructure of non-equilibrium samples . . . 61
Figure 5.6 Microstructure of $Fe_2V_{0.9}Ta_{0.1}Al$ at different magnifications 61
Figure 5.7 Nanoscale precipitates and grain boundary segregation . . 62
Figure 5.8 Microstructural evolution with annealing . . . 63
Figure 5.9 Formation of new grain boundaries . . . 64
Figure 5.10 Lamellar microstructure . . . 64
Figure 5.11 Effect of Ta on the electrical resistivity #1 . . . 65
Figure 5.12 Effect of Ta on the electrical resistivity #2 . . . 66
Figure 5.13 Electrical resistivity of all samples annealed at 1073 K, 7d . 67
Figure 5.14 Effect of impurity phase on the electrical resistivity . . . 68
Figure 5.15 Effect of annealing on the electrical resistivity . . . 69
Figure 5.16 Effect of Ta on the Seebeck coefficient . . . 71
Figure 5.17 Seebeck coefficient of all samples annealed at 1073 K, 7d . . 72
Figure 5.18 Effect of annealing and secondary phase on the Seebeck coefficient . . . 73
Figure 5.19 Power factor of all samples annealed at 1073 K, 7d . . . 74
Figure 5.20 Effect of annealing and secondary phase on the power factor 75
Figure 5.21 Comparison of the power factor with literature . . . 76

Die approbierte gedruckte Originalversion dieser Diplomarbeit ist an der TU Wien Bibliothek verfügbar.
The approved original version of this thesis is available in print at TU Wien Bibliothek.
TU WIEN Bibliothek Your knowledge hub

Die approbierte gedruckte Originalversion dieser Diplomarbeit ist an der TU Wien Bibliothek verfügbar.
The approved original version of this thesis is available in print at TU Wien Bibliothek.

Bibliography

[1] H Al-Yamani and B Hamad. Thermoelectric properties of Fe_2VAl and $Fe_2V_{0.75}M_{0.25}Al$ (M= Mo, Nb, Ta) alloys: first-principles calculations. *Journal of Electronic Materials*, 45(2):1101–1114, 2016.

[2] Alexandre Berche and Philippe Jund. Ab initio description of the different phases in the Al-Fe-V system: Structure, magnetism and thermodynamics. *Computational Materials Science*, 149:28–36, 2018.

[3] Daniel I Bilc and Philippe Ghosez. Electronic and thermoelectric properties of Fe_2VAl: The role of defects and disorder. *Physical Review B*, 83(20):205204, 2011.

[4] Daniel I Bilc, Geoffroy Hautier, David Waroquiers, Gian-Marco Rignanese, and Philippe Ghosez. Low-dimensional transport and large thermoelectric power factors in bulk semiconductors by band engineering of highly directional electronic states. *Physical review letters*, 114(13):136601, 2015.

[5] Olga Bubnova, Zia Ullah Khan, Abdellah Malti, Slawomir Braun, Mats Fahlman, Magnus Berggren, and Xavier Crispin. Optimization of the thermoelectric figure of merit in the conducting polymer poly (3, 4-ethylenedioxythiophene). *Nature materials*, 10(6):429–433, 2011.

[6] Kieron Burke. The abc of dft. *Department of Chemistry, University of California, Irvine, CA*, 92697:117, 2007.

[7] Kieron Burke and Lucas O Wagner. Dft in a nutshell. *International Journal of Quantum Chemistry*, 113(2):96–101, 2013.

[8] Klaus Capelle. A bird's-eye view of density-functional theory. *Brazilian Journal of Physics*, 36(4A):1318–1343, 2006.

[9] Andrea Damascelli. Probing the electronic structure of complex systems by ARPES. *Physica Scripta*, 2004(T109):61, 2004.

[10] Sergey V Faleev and François Léonard. Theory of enhancement of thermoelectric properties of materials with nanoinclusions. *Physical Review B*, 77(21):214304, 2008.

Die approbierte gedruckte Originalversion dieser Diplomarbeit ist an der TU Wien Bibliothek verfügbar.
The approved original version of this thesis is available in print at TU Wien Bibliothek.
TU WIEN Bibliothek Your knowledge hub

[11] Chenguang Fu, Tiejun Zhu, Yintu Liu, Hanhui Xie, and Xinbing Zhao. Band engineering of high performance p-type FeNbSb based half-Heusler thermoelectric materials for figure of merit ZT> 1. *Energy & environmental science*, 8(1):216–220, 2015.

[12] Chhatrasal Gayner and Kamal K Kar. Recent advances in thermoelectric materials. *Progress in Materials Science*, 83:330–382, 2016.

[13] Paul Geerlings, F De Proft, and W Langenaeker. Conceptual density functional theory. *Chemical reviews*, 103(5):1793–1874, 2003.

[14] Swapnil Ghodke, Akio Yamamoto, Hsuan-Chun Hu, Shunsuke Nishino, Takuya Matsunaga, Dogyun Byeon, Hiroshi Ikuta, and Tsunehiro Takeuchi. Improved Thermoelectric Properties of Re-Substituted Higher Manganese Silicides by Inducing Phonon Scattering and an Energy-Filtering Effect at Grain Boundary Interfaces. *ACS applied materials & interfaces*, 11(34):31169–31175, 2019.

[15] Gautam Ghosh. Aluminium-Iron-Vanadium. In *Landbolt-Bornstein-Group IV: Physical Chemistry*, page 1. Springer Berlin, 2005.

[16] H Julian Goldsmid. The Improvement of a specific material -Bismuth Telluride. In *Introduction to Thermoelectricity*, pages 85–107. Springer, 2016.

[17] Tanja Graf, Claudia Felser, and Stuart SP Parkin. Simple rules for the understanding of Heusler compounds. *Progress in solid state chemistry*, 39(1):1–50, 2011.

[18] Satoshi Hiroi, Shunsuke Nishino, Seongho Choi, Okkyun Seo, Jaemyung Kim, Yanna Chen, Chulho Song, Akhil Tayal, Osami Sakata, and Tsunehiro Takeuchi. Phonon scattering at the interfaces of epitaxially grown fe2val/w and fe2val/mo superlattices. *Journal of Applied Physics*, 125(22):225101, 2019.

[19] Y. Iwasaki. K.Kimura Laboratory, Department of Advanced Materials Science, GSFS, The University of Tokyo.

[20] Mercouri G Kanatzidis, John Androulakis, and Joseph R Sootsman. Thermoelectric compositions and process, December 7 2010. US Patent 7,847,179.

[21] H Kato. Effects of Silicon Substitution on Termoelectric Properties of Heusler-type Fe_2VAl Alloy. *J. Japan. Inst. Metals*, 65:652–656, 2001.

[22] M Kato, Y Nishino, U Mizutani, and S Asano. Electronic, magnetic and transport properties of $(Fe_{1-x}V_x)_3Al$ alloys. *Journal of Physics: Condensed Matter*, 12(8):1769, 2000.

Die approbierte gedruckte Originalversion dieser Diplomarbeit ist an der TU Wien Bibliothek verfügbar.
The approved original version of this thesis is available in print at TU Wien Bibliothek.
TU Bibliothek WIEN Your knowledge hub

[23] Yukari Katsura, Hidenori Takagi, and Kaoru Kimura. Roles of carrier doping, band gap, and electron relaxation time in the Boltzmann Transport Calculations of a Semiconductor's Thermoelectric Properties. *MATERIALS TRANSACTIONS*, 59(7):1013–1021, 2018.

[24] K Kimura, K Yamamoto, K Hayashi, S Tsutsui, N Happo, S Yamazoe, H Miyazaki, S Nakagami, JR Stellhorn, S Hosokawa, et al. Local structure and atomic dynamics in fe 2 val heusler-type thermoelectric material: The effect of heavy element doping. *Physical Review B*, 101(2):024302, 2020.

[25] I Knapp, B Budinska, D Milosavljevic, P Heinrich, S Khmelevskyi, R Moser, R Podloucky, P Prenninger, and E Bauer. Impurity band effects on transport and thermoelectric properties of $Fe_{2-x}Ni_xVAl$. *Physical Review B*, 96(4):045204, 2017.

[26] Takao Kozakai and Toru Miyazaki. Experimental and theoretical investigations on phase diagrams of Fe base ternary ordering alloys. *ISIJ international*, 34(5):373–383, 1994.

[27] K Kudo, S Yamada, J Chikada, Y Shimanuki, T Ishibe, S Abo, H Miyazaki, Y Nishino, Y Nakamura, and K Hamaya. Significant reduction in the thermal conductivity of si-substituted fe 2 val epilayers. *Physical Review B*, 99(5):054201, 2019.

[28] Jae Ki Lee, Min-Wook Oh, Byungki Ryu, Ji Eun Lee, Bong-Seo Kim, Bok-Ki Min, Sung-Jae Joo, Hee-Woong Lee, and Su-Dong Park. Enhanced thermoelectric properties of $AgSbTe_2$ obtained by controlling heterophases with Ce doping. *Scientific reports*, 7(1):1–8, 2017.

[29] JD Lee, T Nagatomi, G Mizutani, and K Endo. Photoemission Electron Spectroscopy IV: Angle-resolved photoemission spectroscopy. *Journal of Surface Analysis*, 2010.

[30] M Liu and XY Qin. Enhanced thermoelectric performance through energy-filtering effects in nanocomposites dispersed with metallic particles. *Applied Physics Letters*, 101(13):132103, 2012.

[31] Chin Shan Lue, CF Chen, JY Lin, YT Yu, and YK Kuo. Thermoelectric properties of quaternary Heusler alloys $Fe_2VAl_{1-x}Si_x$. *Physical Review B*, 75(6):064204, 2007.

[32] GD Mahan and Jorge Osvaldo Sofo. The best thermoelectric. *Proceedings of the National Academy of Sciences*, 93(15):7436–7439, 1996.

Die approbierte gedruckte Originalversion dieser Diplomarbeit ist an der TU Wien Bibliothek verfügbar.
The approved original version of this thesis is available in print at TU Wien Bibliothek.
TU Bibliothek WIEN Your knowledge hub

[33] S Maier, S Denis, S Adam, J-C Crivello, J-M Joubert, and E Alleno. Order-disorder transitions in the Fe_2VAl Heusler alloy. *Acta Materialia*, 121:126–136, 2016.

[34] S Masuda, K Tsuchiya, J Qiang, H Miyazaki, and Y Nishino. Effect of high-pressure torsion on the microstructure and thermoelectric properties of Fe_2VAl-based compounds. *Journal of Applied Physics*, 124(3):035106, 2018.

[35] M Mikami, Y Kinemuchi, K Ozaki, Y Terazawa, and T Takeuchi. Thermoelectric properties of tungsten-substituted Heusler Fe_2VAl alloy. *Journal of Applied Physics*, 111(9):093710, 2012.

[36] Yoshio Miura, Kazutaka Nagao, and Masafumi Shirai. Atomic disorder effects on half-metallicity of the full-Heusler alloys $Co_2Cr_{1-x}Fe_xAl$: A first-principles study. *Physical Review B*, 69(14):144413, 2004.

[37] Hidetoshi Miyazaki, Manabu Inukai, and Yoichi Nishino. Effect of Ta substitution on the electronic structure of Heusler-type Fe_2VAl-based alloy. *Journal of Applied Physics*, 120(12):125106, 2016.

[38] Hidetoshi Miyazaki, Suguru Tanaka, Naoki Ide, Kazuo Soda, and Yoichi Nishino. Thermoelectric properties of Heusler-type off-stoichiometric $Fe_2V_{1+x}Al_{1-x}$ alloys. *Materials Research Express*, 1(1):015901, 2013.

[39] Tomoyuki Mori, Naoki Ide, and Yoichi Nishino. Thermoelectric Properties of p-Type $Fe_2V_{1-x-y}Ti_xTa_yAl$ Alloys. *JOURNAL OF THE JAPAN INSTITUTE OF METALS*, 72(8):593–598, 2008.

[40] Dario Narducci, Ekaterina Selezneva, Gianfranco Cerofolini, Stefano Frabboni, and Giampiero Ottaviani. Impact of energy filtering and carrier localization on the thermoelectric properties of granular semiconductors. *Journal of Solid State Chemistry*, 193:19–25, 2012.

[41] N. David Mermin Neil W. Ahscroft. *Solid State Physics*. Cengage Learning, Inc, 1976.

[42] Y Nishino. Development of thermoelectric materials based on Fe_2VAl Heusler compound for energy harvesting applications. In *IOP Conference Series: Materials Science and Engineering*, volume 18, page 142001. IOP Publishing, 2011.

[43] Hidekazu Okamura, J Kawahara, Takao Nanba, S Kimura, K Soda, U Mizutani, Yoichi Nishino, M Kato, I Shimoyama, H Miura, et al. Pseudogap formation in the intermetallic compounds $(Fe_{1-x}V_x)_3Al$. *Physical review letters*, 84(16):3674, 2000.

Die approbierte gedruckte Originalversion dieser Diplomarbeit ist an der TU Wien Bibliothek verfügbar.
The approved original version of this thesis is available in print at TU Wien Bibliothek.
TU Bibliothek WIEN Your knowledge hub

[44] Yu Pan and Jing-Feng Li. Thermoelectric performance enhancement in n-type $Bi_2(TeSe)_3$ alloys owing to nanoscale inhomogeneity combined with a spark plasma-textured microstructure. *NPG Asia Materials*, 8(6):e275–e275, 2016.

[45] Yanzhong Pei, Xiaoya Shi, Aaron LaLonde, Heng Wang, Lidong Chen, and G Jeffrey Snyder. Convergence of electronic bands for high performance bulk thermoelectrics. *Nature*, 473(7345):66, 2011.

[46] John P Perdew. Density functional theory and the band gap problem. *International Journal of Quantum Chemistry*, 28(S19):497–523, 1985.

[47] John P Perdew and Mel Levy. Physical content of the exact Kohn-Sham orbital energies: band gaps and derivative discontinuities. *Physical Review Letters*, 51(20):1884, 1983.

[48] S Perumal, Stéphane Gorsse, Ujwala Ail, Rodolphe Decourt, and Arun M Umarji. Effect of Composition on Thermoelectric Properties of Polycrystalline $CrSi_2$. *Journal of electronic materials*, 42(6):1042–1046, 2013.

[49] S Picozzi, AJFA Continenza, and Arthur J Freeman. Role of structural defects on the half-metallic character of Co_2MnGe and Co_2MnSi Heusler alloys. *Physical Review B*, 69(9):094423, 2004.

[50] Krystel Renard, Arinori Mori, Yuichiro Yamada, Suguru Tanaka, Hidetoshi Miyazaki, and Yoichi Nishino. Thermoelectric properties of the Heusler-type $Fe_2VTa_xAl_{1-x}$ alloys. *Journal of Applied Physics*, 115(3):033707, 2014.

[51] M. Reissner S. Bühler Paschen, H. Michor. Festkörperphysik 1. LVA 138.017 (SS 2018).

[52] Yusuke Sandaiji, Naoki Ide, Yoichi Nishino, Takeshi Ohwada, Shota Harada, and Kazuo Soda. Off-stoichiometric effects on thermoelectric properties of fe 2 val-based compounds. *Funtai Oyobi Funmatsuyakin*, 57(4):207–212, 2010.

[53] Shivprasad S Shastri and Sudhir K Pandey. A comparative study of different exchange-correlation functionals in understanding structural, electronic and thermoelectric properties of Fe_2VAl and Fe_2TiSn compounds. *Computational Materials Science*, 143:316–324, 2018.

[54] Xun Shi and Lidong Chen. Thermoelectric materials step up. *Nature materials*, 15(7):691, 2016.

[55] K Soda, H Murayama, K Shimba, S Yagi, J Yuhara, T Takeuchi, U Mizutani, H Sumi, M Kato, H Kato, et al. High-resolution soft X-ray photoelectron study of density of states and thermoelectric properties of the Heusler-type alloys $(Fe_{2/3}V_{1/3})_{100-y}Al_y$. *Physical Review B*, 71(24):245112, 2005.

Die approbierte gedruckte Originalversion dieser Diplomarbeit ist an der TU Wien Bibliothek verfügbar.
The approved original version of this thesis is available in print at TU Wien Bibliothek.
TU WIEN Bibliothek Your knowledge hub

[56] Kazuo Soda, Shota Harada, Masahiko Kato, Shinya Yagi, Yusuke Sandaiji, and Yoichi Nishino. Origin of large thermoelectric power in off-stoichiometric fe2val-based alloys. In *IOP Conference Series: Materials Science and Engineering*, volume 18, page 142004. IOP Publishing, 2011.

[57] S Sumithra, Nathan J Takas, Dinesh K Misra, Westly M Nolting, PFP Poudeu, and Kevin L Stokes. Enhancement in thermoelectric figure of merit in nanostructured Bi_2Te_3 with semimetal nanoinclusions. *Advanced Energy Materials*, 1(6):1141–1147, 2011.

[58] Tsunehiro Takeuchi, Yuichi Terazawa, Yukihiro Furuta, Akio Yamamoto, and Masashi Mikami. Effect of heavy element substitution and off-stoichiometric composition on thermoelectric properties of Fe_2VAl-based Heusler phase. *Journal of electronic materials*, 42(7):2084–2090, 2013.

[59] Yuichi Terazawa, Masashi Mikami, Takashi Itoh, and Tsunehiro Takeuchi. Effects of heavy element substitution on electronic structure and lattice thermal conductivity of Fe_2VAl thermoelectric material. *Journal of electronic materials*, 41(6):1348–1353, 2012.

[60] M Vasundhara, V Srinivas, and VV Rao. Electronic transport in Heusler-type $Fe_2VAl_{1-x}M_x$ alloys (M= B, In, Si). *Physical Review B*, 77(22):224415, 2008.

[61] Ch Venkatesh, V Srinivas, VV Rao, SK Srivastava, and P Sudheer Babu. Effect of site disorder on the electronic properties of Fe_2VAl Heusler alloy. *Journal of Alloys and Compounds*, 577:417–425, 2013.

[62] Peter J Webster. Heusler alloys. *Contemporary Physics*, 10(6):559–577, 1969.

[63] Wikipedia contributors. Bragg's law — Wikipedia, the free encyclopedia, 2019. [Online; accessed 15-March-2020].

[64] Wikipedia contributors. Angle-resolved photoemission spectroscopy — Wikipedia, the free encyclopedia, 2020. [Online; accessed 15-March-2020].

[65] Wikipedia contributors. Bloch wave — Wikipedia, the free encyclopedia, 2020. [Online; accessed 15-March-2020].

[66] Wikipedia contributors. Brillouin zone — Wikipedia, the free encyclopedia, 2020. [Online; accessed 15-March-2020].

[67] Wikipedia contributors. Thermoelectric effect — Wikipedia, the free encyclopedia, 2020. [Online; accessed 15-March-2020].

Die approbierte gedruckte Originalversion dieser Diplomarbeit ist an der TU Wien Bibliothek verfügbar.
The approved original version of this thesis is available in print at TU Wien Bibliothek.
TU Bibliothek WIEN Your knowledge hub

[68] Alex Zevalkink, David M Smiadak, Jeff L Blackburn, Andrew J Ferguson, Michael L Chabinyc, Olivier Delaire, Jian Wang, Kirill Kovnir, Joshua Martin, Laura T Schelhas, et al. A practical field guide to thermoelectrics: Fundamentals, synthesis, and characterization. *Applied Physics Reviews*, 5(2):021303, 2018.

[69] Tianhua Zou, Xiaoying Qin, Yongsheng Zhang, Xiaoguang Li, Zhi Zeng, Di Li, Jian Zhang, Hongxing Xin, Wenjie Xie, and Anke Weidenkaff. Enhanced thermoelectric performance of β-Zn_4Sb_3-based nanocomposites through combined effects of density of states resonance and carrier energy filtering. *Scientific reports*, 5:17803, 2015.

Die approbierte gedruckte Originalversion dieser Diplomarbeit ist an der TU Wien Bibliothek verfügbar.
The approved original version of this thesis is available in print at TU Wien Bibliothek.
TU Bibliothek WIEN Your knowledge hub